Material screening and performance analysis of active magnetic heat pumps

by

Iman Niknia
M.Sc., Shiraz University, 2011
B.Sc., Shiraz University, 2008

A Dissertation Submitted in Partial Fulfillment
of the Requirements for the Degree of

DOCTOR OF PHILOSOPHY

in the Department of Mechanical Engineering

# Supervisory Committee

Material screening and performance analysis of active magnetic refrigerators and heat pumps

by

Iman Niknia
M.Sc., Shiraz University, 2011
B.Sc., Shiraz University, 2008

**Supervisory Committee**

Dr. Andrew Rowe (Department of Mechanical Engineering)
**Supervisor**

Dr. Mohsen Akbari (Department of Mechanical Engineering)
**Departmental Member**

Dr. Phalguni Mukhopadhyaya (Department of Civil Engineering)
**Outside Member**

# Abstract

**Supervisory Committee**

Dr. Andrew Rowe (Department of Mechanical Engineering)
**Supervisor**

Dr. Mohsen Akbari (Department of Mechanical Engineering)
**Departmental Member**

Dr. Phalguni Mukhopadhyaya (Department of Civil Engineering)
**Outside Member**

With the discovery of the magnetocaloric effect, utilizing magnetocaloric materials in cycles to generate cooling power began. The magnetocaloric effect is a physical phenomenon observed in some magnetic materials where the temperature of the material increases and decreases with application and removal of magnetic field. Usually the adiabatic temperature change observed in magnetocaloric materials is too small for room temperature refrigeration. A solution to this problem is to use magnetocaloric materials in an active magnetic regenerator (AMR) cycle.

In this study a detailed numerical model is developed, validated, and used to improve our understanding of AMR systems. A one dimensional, time dependent model is used to study the performance of an active magnetic regenerator. Parameters related to device configuration such as external heat leaks and demagnetization effects are included. Performance is quantified in terms of cooling power and second law efficiency for a range of displaced fluid volumes and operating frequencies. Simulation results show that a step change model for applied field can be effectively used instead of full field wave

form if the flow weighted average low and high field values are used. This is an important finding as it can greatly reduce the time required to solve the numerical problem. In addition, the effects of external losses on measured AMR performance are quantified.

The performance of eight cases of known magnetocaloric material (including first order $MnFeP_{1-x}As_x$ and second order materials Gd, GdDy, Tb) and 15 cases of hypothetical materials are considered. Using a fixed regenerator matrix geometry, magnetic field, and flow waveforms, the maximum exergetic cooling power of each material is identified. Several material screening metrics such as *RCP* and *RC* are tested and a linear correlation is found between $RCP_{Max}$ and the maximum exergetic cooling power. The sensitivity of performance to variations in the hot side and cold side temperatures from the conditions giving maximum exergetic power are determined. The impact of 2 K variation in operating temperature is found to reduce cooling power up to 20 % for a second order material, but can reduce cooling power up to 70% with a first order material.

A detailed numerical analysis along with experimental measurements are used to study the behavior of typical first order material ($MnFeP_{1-x}Si_x$ samples) in an AMR. For certain operating conditions, it is observed that multiple points of equilibrium (PE) exist for a fixed heat rejection temperature. Stable and unstable PEs are identified and behavior of these points are analysed. The impacts of heat loads, operating conditions and configuration losses on the number of PEs are discussed and it is shown that the existence of multiple PEs can affect the performance of an AMR significantly. Thermal hysteresis

along with multiple PEs are considered as the main factors that contribute to the temperature history dependent performance behavior of FOMs when used in an AMR.

# Table of contents

# List of Figures

# List of Tables

# Nomenclature

| | | |
|---|---|---|
| *A* | Area | $m^2$ |
| *B* | Applied field | T |
| *c* | Specific heat | $Jkg^{-1}K^{-1}$ |
| *C* | Volumetric specific heat | $Jm^{-3}K^{-1}$ |
| *h* | Convection coefficient | $Wm^{-2}K^{-1}$ |
| *H* | Magnetic field | $Am^{-1}$ |
| *K* | Thermal conductance | $WK^{-1}$ |
| *L* | Length | m |
| *m* | Mass | kg |
| *M* | Magnetization | $Am^2kg^{-1}$ |
| *P* | Pressure | Pa |
| *Q* | Heat transfer, net enthalpy flux | W |
| *R* | Thermal mass ratio | - |
| *S* | Entropy | $Jkg^{-1}K^{-1}$ |
| *T* | Temperature | K |
| *t* | Time coordinate | s |
| *V* | Volume | $m^3$ |
| *x* | Non-dimensional spatial coordinate | - |

**Greek**

| | | |
|---|---|---|
| $\alpha$ | Porosity | - |
| $\eta$ | Efficiency | - |
| $\mu$ | Dynamic viscosity | N s $m^{-2}$ |
| $\rho$ | Density | $kgm^{-3}$ |
| $\tau$ | Period | s |

**Subscript**

| | | |
|---|---|---|
| *0* | Ambient | - |
| *B* | Constant magnetic Field, ($\mu_0 H$), or blow | - |
| *C* | Cold | - |
| *e* | electronic | - |
| *eff* | Effective | - |
| *f* | Fluid | - |
| *H* | Hot or high-field | - |
| *l* | Lattice | - |
| *M* | Magnetic | - |
| *s* | Solid | - |
| *sat* | Saturation | - |

**Superscript**

| | | |
|---|---|---|
| $'$ | Per unit length | - |
| * | Normalized value | - |
| $\cdot$ | Per unit time | - |

# Acknowledgments

Thank you for all your guidance and support Andrew. I really admire you for your always positive and supporting attitude and your outstanding knowledge. I am most grateful for your thoughtful feedback, insightful advice and supervision in every step of my research. I learned a lot from you during the last few years. You provided me with a wonderful opportunity to work on an exciting research project in a great team environment for which I will always be thankful.

I would like to thank my valued colleagues involved in magnetic refrigeration research for all the discussions, suggestions and espresso memories: Armando Tura, Oliver Campbell, Paulo Trevizoli, Premakumara Govindappa, Theodor Christiaanse, Reed Teyber, Yifeng Liu and Jana Strain.

# Dedication

I would like to dedicate this thesis to my family.

# Chapter 1 Introduction

Approximately 40% of the world energy is consumed in residential and commercial buildings and more than 35% of the total energy consumption in buildings is for heating, ventilation and air-conditioning systems (HVAC), and refrigeration [1]. These large numbers indicate the importance of research to improve efficiency as small improvements can lead to a significant reduction in energy demand on a larger scale. A technology which can be considered an alternative to conventional devices is a magnetic heat pump.

In this section, a brief introduction to a magnetic heat pump is provided. *Heat pump* is a generic term for a device which converts work to heat transfer between cold and warm temperature reservoirs. The desired outcome may be to provide heat or refrigeration. The analogies and differences between compressor-based refrigeration and magnetic refrigeration are discussed. Different categories of magnetocaloric materials are introduced and their characteristics are described. The concept of active regeneration is introduced. Some of the challenges of modeling magnetic refrigeration systems are discussed and finally, the concept of layering a regenerator is briefly described.

## 1.1 Magnetic Refrigeration

Magnetic refrigeration (MR) is a cooling technology which has the potential to increase efficiency over current compressor based devices [2]. MR is based on the magnetocaloric effect (MCE) – a reversible phenomenon observed in some materials,

where the temperature of the material increases when an adiabatic material is exposed to a magnetic field and its temperature drops as the external field is removed. Gas refrigeration cycles usually consist of four stages (Fig. 1): compression, heat transfer, expansion, and a second heat transfer stage. In a magnetic refrigeration cycle, the compression and expansion stages are replaced by magnetizing and demagnetizing stages (Fig. 2). Compared to conventional vapor compression systems, MR has little to no environmental impacts because the refrigerant is solid with no ozone depleting effects or global warming potentials [3]. Preliminary studies have shown that MRs can have high intrinsic efficiency. It was experimentally shown that a COP of 15 can be obtained for a cooling power of 600W and an applied magnetic field of 5 T [4,5].

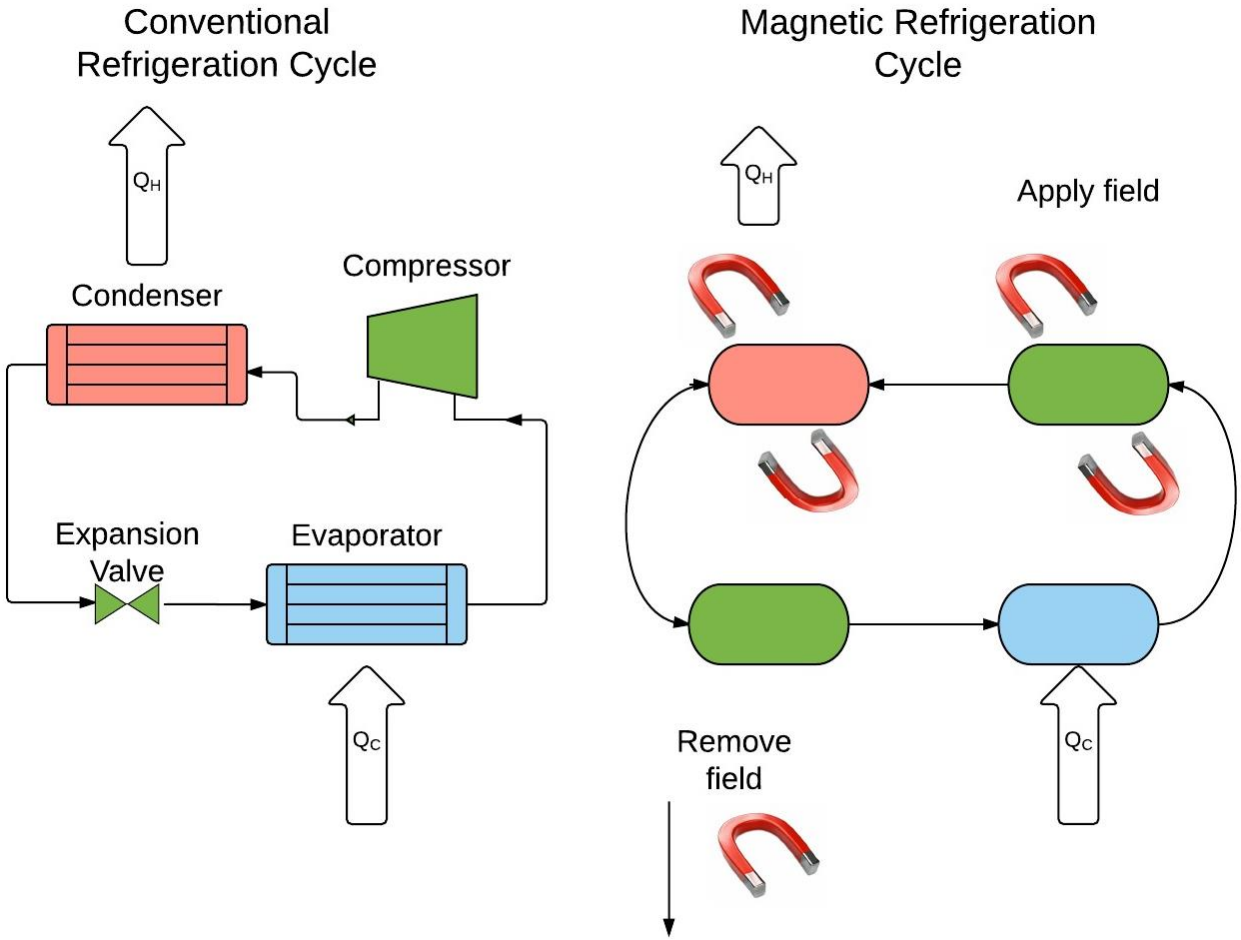


Fig. 1 Gas compression refrigeration cycle (on the left) and magnetic refrigeration cycle (on the right). $Q_c$ represents the energy absorbed from the cold reservoir and $Q_h$ represents the energy rejected at the hot reservoir. In a magnetic refrigeration cycle, the compression and expansion stages of a conventional compressor based refrigerator are replaced by magnetizing and demagnetizing stages.

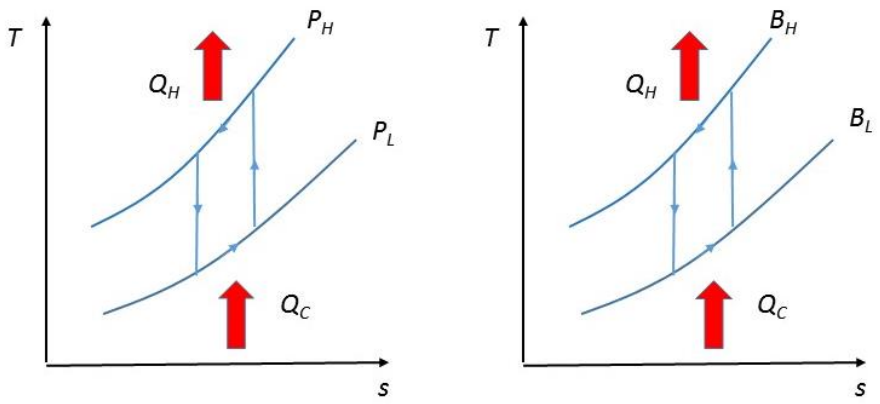


Fig. 2 T-S diagram for a Brayton compression refrigeration cycle (on the left) and a Brayton magnetic refrigeration cycle (on the right). $P_H$ and $P_L$ represent high and low pressure lines and $B_H$ and $B_L$ represent the high field and low field lines

The MCE observed in most materials is usually not sufficiently large to be directly used in a refrigeration cycle. As a result, thermal regeneration is used to increase the temperature spans that can be achieved. A regenerator is created by using a porous solid matrix to periodically exchange heat with a fluid flowing through the void space. In an AMR cycle, the magnetocaloric material (MCM) acts both as the refrigerant and the heat regenerator. Heat transfer fluid is displaced through the porous structure formed by the MCM while the applied magnetic field is varied from low intensity to high (analogues to compression and expansion in conventional refrigerators). Repeated cycling converts magnetic work to heat transfer and results in a temperature span along the length of the regenerator.

In recent years, research has focused on the design and construction of prototypes that use magnetocaloric materials in active magnetic regenerator (AMR) cycles [6]. Yu et al. in a review paper, provided a list and description of magnetic heating and cooling

prototype designs up to the year 2010 [6]. The efficiency of an active magnetic regenerative refrigerator (AMRR) strongly depends on the magnitude of the applied field, the thermodynamic design of the cycle and the intrinsic properties of the material. Hence; selecting proper material to use in an effective AMR cycle is a crucial step in developing efficient systems.

## 1.2 Magnetocaloric Materials

The magnetocaloric effect is most pronounced in materials that undergo a transformation from a disordered magnetic state to an ordered state due to changes in temperature or applied magnetic field. There are a number of different ways magnetic materials can order – *ferro*magnetic, *para*magnetic, etc. Here, the term ferromagnetism will be used to indicate the magnetically ordered state. Magnetocaloric materials can be classified into two types based on the transition behavior from ferromagnetic (ordered) to paramagnetic (disordered) phase: second order materials (SOM) and first order materials (FOM). SOMs exhibit ferromagnetic to paramagnetic phase transition at a transition temperature usually referred to as Curie temperature (i.e. when temperature approaches transition temperature, magnetization decreases continuously). SOMs tend to order gradually over a wider temperature range, and, as a result, the useful MCE effect is available over a wider temperature range. However, conventional SOMs can be expensive and not always suitable for room temperature applications. Among SOMs, gadolinium (Gd) exhibits high MCE (~3 K/T) with a Curie temperature close to room temperature. These characteristics have made it a benchmark material for room

temperature AMRRs. Gd is a rare earth element and is considered to be too expensive for broad commercial use.

Typical FOMs use readily available constituent elements, are cheaper, and their Curie point is tunable. Theoretically, the ferromagnetic to paramagnetic phase transition in FOMs is discontinuous and a latent heat is associated with their ordering; their useful magnetocaloric effect is limited to a narrower temperature range (Fig. 3). In practice, in FOMs the transition is sharp, but continuous. As a result, the useful temperature range in an AMRR device is limited.

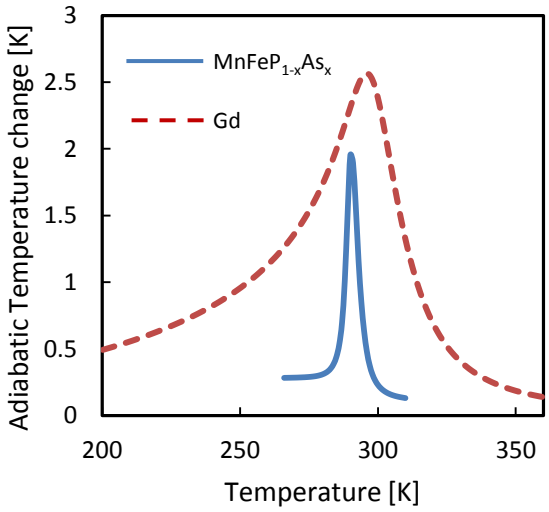


Fig. 3 Adiabatic temperature change as a function of temperature for an FOM and SOM under applied fields of 0.35 to 1.1 T. For the SOM, Gadolinium properties are shown and for FOM, one sample of $MnFeP_{1-x}As_x$ material is presented. The adiabatic temperature change curve for second order materials are wider compared to the first order materials [7].

## 1.3 Layering

For both FOMs and SOMs, the effective MCE decreases as the operating temperature deviates from the Curie temperature. Layering materials with different phase transition

temperatures in an active magnetic regenerator (AMR) is one way to overcome this problem and create a wider operating span. Rowe and Tura experimentally studied the performance of a three layer regenerator made out of second order material alloys [8] and showed that proper layering can lead to better performance and higher temperature spans. You et al. [9] numerically compared the performance of a layered regenerator consisting of Gd and $Gd_{0.73}Tb_{0.27}$ with a similar AMR of pure Gd and concluded that at a temperature span of 28 K, cooling power and COP of the multilayered AMRs exceed the one layer system by ~167% and 57% respectively. Aprea et al. [10] proposed a numerical model to study the performance of layered regenerators. They studied $Gd_xTb_{1-x}$ alloys as constituent materials for the regenerator over the temperature range 275–295 K, and $Gd_xDy_{1-x}$ alloys in the temperature range 260–280 K. They concluded that the performance of a layered regenerator can significantly exceed the performance of a single layer regenerator. The COP was reported to increase as a function of the number of layers. Tusek et al. [11] studied the performance of layered AMR with different compositions and Curie temperatures made from $LaFe_{13-x-y}Co_xSi_y$ materials. They investigated the performances of seven, four and two layered regenerators and determined that although the performance of two-layered was significantly worse than the four-layered, the performance of seven-layered regenerator was very similar to the four-layered. In other words, increasing the number of layers did not necessarily result in increased performance. Campbell et al. [12] utilized $MnFeP_{1-x}As_x$ class of material in layered structure and experimentally investigated various combinations of layers with different curie temperatures (Fig. 4). The mass of material per layer was also varied. For

the eight-layer regenerator, three different cases of 5, 10 and 15 mm/layer AMR were investigated. For each case the maximum temperature span was reported as the performance metric. It was observed that the temperature span for 15 mm/layer is close to 10 mm/layer even though there is a broader temperature range where there is useful MCE in the case of the 15 mm/layer. The performance is much lower for the 5 mm/layer case. This indicates high sensitivity of AMR performance to design parameters such as mass per layer and number of materials.

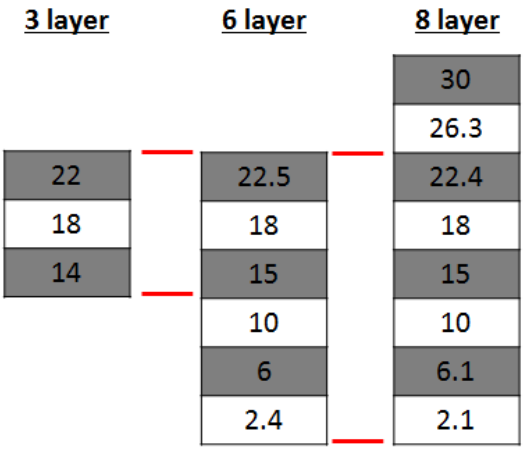


Fig. 4. Visual representation of layered AMR design conditions. The values represent Curie temperature of each layer in Celsius [12]

Monfared et al. [13] performed a numerical study on a multilayered packed bed regenerator to optimize the performance of the system. In this regard, they used properties of gadolinium with different curie temperatures and numerically adjusted the heat capacities of the material to develop a layered regenerator bed with different properties. They argued that to get a higher temperature span, a material with the highest MCE in the working temperature range should be used in a regenerator. However, to

achieve higher Carnot efficiency, the Curie temperatures of the material should be above the average layer temperature.

Although layering seems like an effective method to improve the performance of a regenerator, care should be taken in selecting material (transition temperature, particle size and other physical properties). The development of numerical tools to study and understand the behavior of layered regenerators is needed as material preparation, device development and experimental study can be expensive and time consuming. Although SOMs usually perform better in a layered system, FOMs are attracting attention due to their availability, lower price, and tunable curie temperatures. One of the reasons that FOM layered regenerators are not investigated widely is that modeling FOM regenerators is a challenging problem due to their first order transition behavior and hysteresis. Although the behavior and influence of hysteresis is not fully understood, it has been shown that hysteresis can significantly reduce the performance of FOMs in AMR systems [14,15]. Other challenges exist with FOMs such as steep changes in material properties. Smith et al. further discuss the challenges we face when looking for high performance material to utilize in AMR systems [16].

## 1.4 Summary

In this chapter a brief introduction to the magnetic refrigeration was presented. Some of the main concepts such as magnetocaloric effect were introduced. Some of the challenges in developing efficient magnetocaloric heat pumps were discussed. Two classes of MCM (FOM and SOM) were introduced and some of the shortcomings of each

class of material were explained. In the following chapter, some of the key questions and challenges in developing efficient magnetocaloric heat pumps will be described and the main objectives of the current research will be presented.

# Chapter 2 Motivation and Objectives

The application of the magnetocaloric effect in cryogenic cooling can be traced to the early works of Collins and Zimmerman [17] where they constructed a magnetic refrigerator which could operate at 1 to 0.73 K. However, this technology did not attract much attention for near room temperature application until Brown [18] introduced a near room temperature magnetic refrigerator which had a zero cooling power temperature span of around 47 K. Since then, room temperature magnetic refrigeration has been the subject of much research. With the discovery of first order transition material with giant magnetocaloric effect [19] the number of researchers involved in the field of room temperature magnetic cooling, increased significantly.

One of problems with using magnetocaloric material (MCM) in a cooling cycle is the distribution of MCE around the peak. It is observed that as the temperature of the MCM deviates from the transition temperature, the MCE value drops significantly from a maximum value. This problem becomes more critical with first order material where the MCE curve as a function of temperature is quite narrow and sharp, meaning that MCE is very sensitive to the operating temperature. Another problem with using first order transition material is thermal and magnetic hysteresis that these materials usually exhibit.

It is experimentally demonstrated that layering different alloys with close peak temperatures can be an efficient method in increasing the operating temperature range and cooling power of magnetic refrigeration systems [8]. However, finding the optimum configuration of layers and selection of the material for layers are problems that need

further investigations. In this regard, numerical models are a reasonable and relatively inexpensive approach to investigate an AMR system for optimizing system design, operating parameters and layering configurations.

The combined effects of non-linear material properties, varying magnetic field, time-dependent heat transfer and fluid flow make an AMR a complicated system to model. Nielsen et al. reviewed numerical models proposed for room temperature AMR systems [20]. Some of the studies in the literature, aimed to develop one-dimensional transient models without solving the fluid flow problem [21–23]. Other studies have focused on creating two-dimensional models of the regenerator [24–26]. Including more detail in a model is usually at the expense of speed of solution. One of the challenges for numerical analysts is to find a suitable balance of detail and range of physical interactions to consider [27].

Experimental studies of AMR cycles always include system effects beyond the regenerator; as a result, higher resolution regenerator models may be no better than simpler ones if these are not considered. A semi-analytical model was shown to replicate device performance over a broad range of conditions when demagnetization and device heat leaks were included [28,29]. Modeling has been widely used to investigate AMR performance, but validation of AMR models requires experimental data where system impacts are decoupled from regenerator impacts. In this regard, experimental AMR devices can be considered as imperfect instruments when measuring only the AMR performance is the goal.

## 2.1 Objectives and Contributions

Until recently, different research groups around the world were developing magnetic refrigerators (MR) to demonstrate the feasibility and performance of this technology in actual devices [6,30,31] with little concern about the actual cost of cooling. However, this situation is changing. As MR is being introduced as a new cooling technology with the potential to replace the compressor based systems, some of the studies are shifting toward understanding the characteristics of the prototypes [32] and the real cost of cooling [33].

To reduce the cost of cooling, the performance of an AMR refrigerator (AMRR) needs to be understood and improved. Performance of an AMRR depends on three major contributing factors:

1. Device design and configuration losses;
2. Magnetocaloric material and its characteristics; and,
3. Operating conditions.

The objective of this study is to extend our understanding of an AMRR system through numerical simulations and experimental measurements in order to improve the performance of magnetic heat pumps. This thesis addresses the factors listed above by focusing on the following questions.

- Design and configuration:
    - What are the key parameters that affect the performance of experimental devices?

  - What are the configuration losses and how can they impact the performance of a system?
  - How can one measure and include these parameters in numerical models effectively?
- Magnetocaloric material:
  - What is an effective material screening technique for selecting material for an AMR system?
  - How do the available screening techniques correlate with the performance of the material in real devices?
- Operating conditions:
  - How do operating condition impact the performance of an AMR?
  - What are the key parameters that need to be understood regarding the performance of FOMs in an AMR?
  - Why is the performance of an AMR with FOM dependent on temperature history of the regenerator?
  - How does temperature history affect stability and performance of an AMR?

The answers to these questions can improve our understanding of the coupling between experimental measurements and numerical simulations. Understanding the impacts of configuration losses and operating conditions can help with the creation of efficient numerical models which are capable of predicating the device performance with reasonable accuracy. With reliable numerical models, it is important to identify materials that actually perform well in real devices and to understand how the optimal performance of a material correlates with the properties of the material. Among the FOM class of material, there are still many questions that need to be answered before FOMs can be used to design efficient and inexpensive layered regenerators. Therefore, the last section of this research focuses on furthering our understanding of FOM material performance in

real devices. This can help us understand why performance is temperature history dependent and why increasing the number of layers in a regenerator does not necessarily result in better performance.

## 2.2 Methods

Both numerical simulation and experimental characterization is used to answer the questions described above. First, an experimental device is fully characterized using single material AMRs comprised of Gd. Parameters that affect the performance of the experimental device such as external loss factors are quantified. A numerical model is developed and the performance of the model is validated for the experimental apparatus. Through numerical simulations and experimental measurements, the key parameters that affect the performance of an AMR are analyzed.

Preferred metrics for selecting material for an AMR are identified from the literature. Using the validated numerical model, the performance of different materials in an AMRR is studied and the correlation between the optimum performances of a material with the screening metrics is further analyzed. From this work, the most effective screening technique for selecting material is determined and its correlation with optimum performance is studied.

The performance of sample FOM material are experimentally studied. Some of the differences between the performance of FOMs and SOMs (such as temperature path dependence of performance) is elaborated on. Finally, the numerical model is used to further investigate the performance of FOMs in an AMR.

## 2.3 Framework

In this section a brief overview of the thesis structure is presented.

In Chapter 3 the thermodynamics of an AMR is described. Key parameters such as adiabatic temperature change and magnetic entropy change of an MCM under applied field are further discussed and the relations between these two parameters and magnetization are studied. The concept of regeneration is presented and AMR theory is further explained. Magnetocaloric material used for experimental measurements is introduced. Gd (which is the benchmark material for AMR studies) is investigated in more detail followed by a brief introduction to Mn based alloys. The term *screening metric* is defined and some of the available metrics for material selection in literature are introduced. The performance metrics used in this thesis for comparison and performance analysis of an AMR are defined.

In Chapter 4, device configuration is introduced. Thermal loss mechanisms related to configuration are studied and the experimental technique used for measuring loss coefficients is discussed. The test apparatus used for measurements is presented. Finally the measurement procedure is explained.

In Chapter 5, the development of the numerical model is described. First, the theories and governing equations of the two phase system are presented. The correlations used to calculate transport properties for the solid and fluid phases are presented. The boundary conditions and the discretization technique are briefly discussed. Some characteristics of

the AMRR device such as field and flow wave forms are explained and finally the solution method and grid study are presented.

In Chapter 6, experimental measurements are used to validate the performance of the numerical model. After validating, a parametric study is performed on the impacts of different operating conditions such as heat rejection temperature, frequency and displaced volume on the performance of an AMR. The impacts of configuration losses on the cooling power and efficiency of an AMRR is further discussed.

In Chapter 7, numerical simulation are used to investigate the effectiveness of different material screening techniques in identifying material for optimum performance of an AMR. The performance of different materials in an AMR are studied and points of optimum performance are identified. The effectiveness of different screening metrics in identifying material with high potential are further explained.

In Chapter 8, performance of FOM with a narrow MCE curve (sharp curve toward transition point) is examined. Multiple points of equilibrium are identified for FOM material. Stability of points of equilibrium are further discussed and criteria for distinguishing an unstable point of equilibrium is presented. The impacts of this phenomenon on the performance of FOMs in AMRR are further examined and impacts of the operating conditions on the existence and location of a point of equilibrium is elaborated on.

In the final chapter (Conclusion) the main findings of this thesis are summarized, the results are discussed, and recommendations for future work are provided.

## 2.4 Summary

In this chapter the main objectives of this thesis were presented. The methods used to address the questions were introduced. In the final section, the framework of the thesis was discussed. In the next chapter, thermodynamics of an AMR will be described and some of the key parameters in AMR studies will be defined.

# Chapter 3 Active Magnetic Regenerator

In this chapter, the principles of operation of an AMR are discussed. First, a brief introduction to the magnetocaloric effect is provided and the theory of an AMR is presented. Then, several materials with first order and second order phase transition are selected and their properties are briefly discussed. Select properties and metrics used to rank magnetocaloric materials are described. And finally parameters used to quantify the performance of a material in a device are introduced.

## 3.1 Principals of Magnetic Cooling and Heating

Magnetic heating and cooling systems are based on the magnetocaloric effect (MCE) which is usually defined as the adiabatic temperature change upon applying and removing magnetic field. This phenomenon can be explained by looking more closely at the entropy change of magnetic material when exposed to change of magnetic field. Entropy of a magnetic material at a fixed temperature, pressure and field is comprised of three components of electronic $S_e$, lattice $S_l$ and magnetic $S_m$ entropies [34]. The summation of these three components gives the entropy $S$ of a material. In a general form, all the three components of entropy can be functions of temperature, pressure and magnetic field,

$$S(T,P,H) = S_e(T,P,H) + S_l(T,P,H) + S_m(T,P,H) \quad (1)$$

Usually, magnetic entropy is a strong function of magnetic field; however, electronic and lattice entropy are practically independent of the magnetic field for most cases. As a result, for entropy which is a state function, the following can be deduced [35]:

$$dS(T,P,H)=\left(\frac{\partial S}{\partial T}\right)_{P,H}dT+\left(\frac{\partial S}{\partial P}\right)_{T,H}dP+\left(\frac{\partial S}{\partial H}\right)_{T,P}dH \tag{2}$$

For constant temperature and pressure, considering that lattice and electronic entropy are usually independent of the magnetic field,

$$\Delta S(T,P,H)_{T,P,\Delta H}=\Delta S_m(T,P,H)_{T,P,\Delta H} \tag{3}$$

Once magnetic field is applied to a magnetic material, the magnetic dipoles of the material will align with the applied field, causing a drop in the magnetic entropy of the material. If the process is done adiabatically, the total entropy of the material will remain unchanged. As a result, the lattice entropy will increase causing the temperature of the material to rise. This temperature increase measured in adiabatic magnetization and demagnetization process is called the adiabatic temperature change $\Delta T(T,P,H)_{\Delta H,P}$. If this process is done at constant temperature, the change in entropy is called magnetic entropy change (Fig. 5). With the use of Maxwell equations and assuming the state of the material is a function of temperature and field only [2], adiabatic temperature change and magnetic entropy change can be correlated to magnetization as follows:

$$\Delta T_{ad}=-\int_0^H\frac{T}{c_H}\left(\frac{\partial M}{\partial T}\right)_H d\mu_0 H \tag{4}$$

$$\Delta S_M=\int_0^H\left(\frac{\partial M}{\partial T}\right)_H d\mu_0 H. \tag{5}$$

where magnetization and entropy change are per unit mass (corresponding to specific heat) and $\mu_0 H$ is local field strength in Tesla. Fig. 6 shows adiabatic temperature change and magnetic entropy change for Gd when the field is changed from 0.35 to 1.1 Tesla.

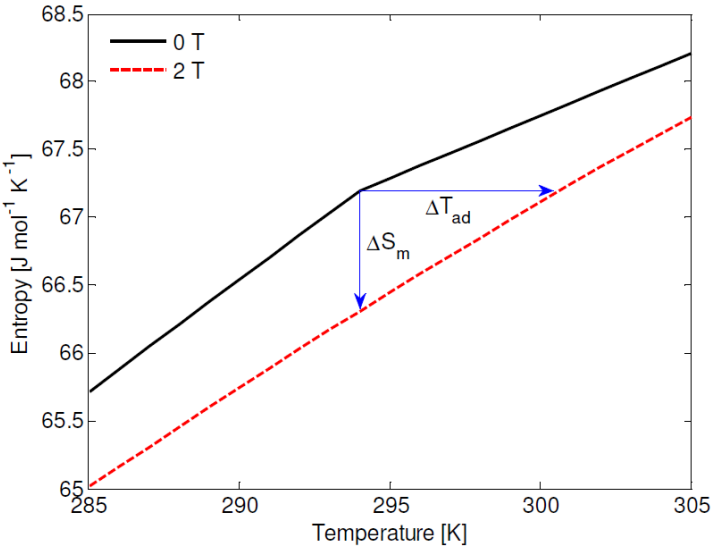


Fig. 5 Adiabatic temperature change and magnetic entropy change for Gd between 0 and 2 Tesla of applied fields [36].

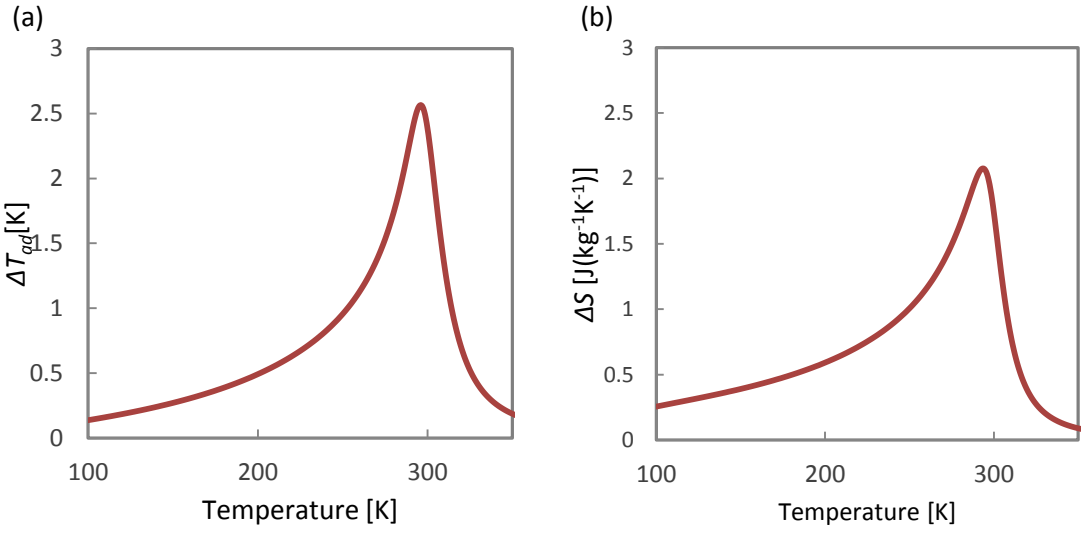


Fig. 6 a) adiabatic temperature change and b) magnetic entropy change for Gd between 0.35 and 1.1 Tesla of applied fields [37].

## 3.2 AMR Theory

Adiabatic temperature change of known materials usually does not exceed a few degrees per Tesla of field change. For example, for Gd with applied fields of 2 and 5 Tesla an MCE of 6.4 K and 11.6 K are reported [38] (In room temperature permanent magnet magnetic heat pumps, the applied field is usually less than 2 Tesla due to the cost and design complications [39]). If material with such small MCE is directly used in refrigeration cycles, the developed temperature span is usually too small for most heat pump applications. Therefore, active magnetic regenerative cycles are used to develop larger temperature spans.

In section 1.1, a general comparison between an AMR cycle and a conventional refrigeration cycle was presented. In this section, a more detailed explanation of the thermodynamic cycle inside an AMR bed is presented. Fig. 7 shows a schematic of an AMR bed where the dashed lines represent an AMR bed with length *L*. A small cross section of the bed with length $\delta x$ is selected as the control volume. The regenerator consists of two phases of fluid and solid. The fluid acts as the heat transfer agent between the refrigerant and the heat exchangers. When an AMR is operated, each section of the regenerator will go through a Brayton refrigeration cycle. Because the temperature along the regenerator is not constant and, in some cases, the local field is not the same, each section will go through its own cycle defined by the state of the material in the section.

Over a complete cycle, heat will be absorbed from the cold side and will be rejected to the hot side of the refrigerator.

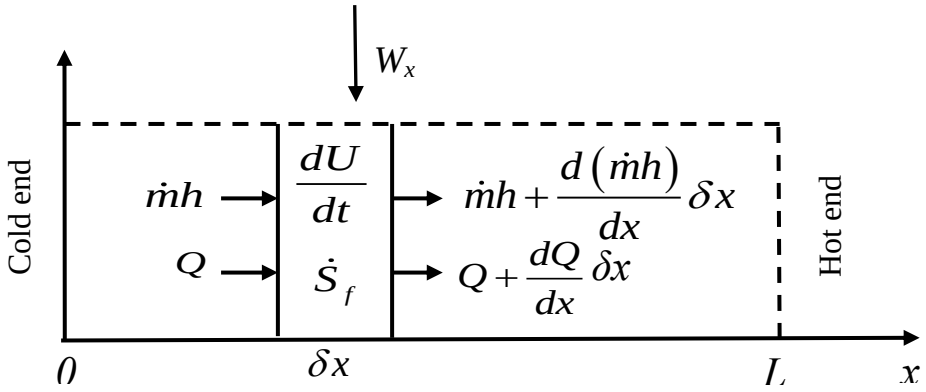


Fig. 7 A schematic representation of an AMR bed. A cross section with length of $\delta x$ is selected and the fluxes of energy are presented for the cross section [40].

As shown in Fig. 8, each section goes through four distinct stages during an AMR cycle:

a-b) While the AMR is at low field (demagnetized) fluid is pumped from the hot side toward the cold side of the regenerator. The fluid exchanges heat with the refrigerant and as the refrigerant temperature rises, the fluid temperature will drop. The solid temperature change, $\delta Tc$, occurs due to regeneration during the hot to cold blow period (Fig. 8).

b-c) Magnetic field is applied to the regenerator bed and the temperature of the refrigerant increases due to the MCE, $\Delta T(T,H)$. At each location, the refrigerant temperature will rise depending on its initial temperature and the local applied field.

c-d) Heat transfer fluid is pumped through the porous medium of the regenerator from the cold side to the hot side. The fluid absorbs heat from the solid phase, cooling down the refrigerant. $\delta T_H$ occurs due to regeneration during the cold to hot blow period.

d-a) Magnetic field is removed (isentropic process) causing the temperature of the refrigerant to decrease due to the MCE effect.

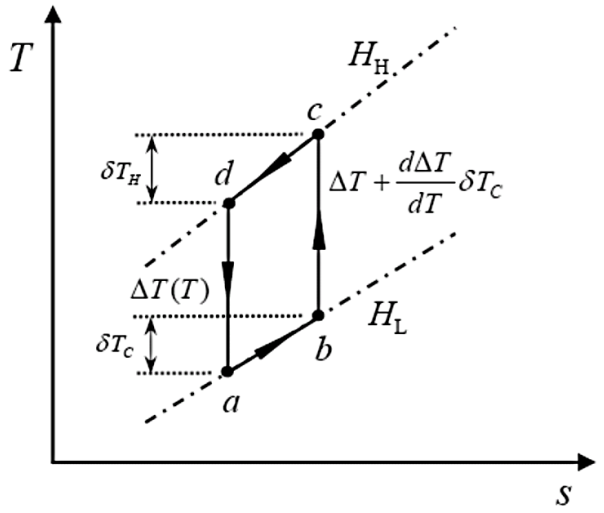


Fig. 8 Hypothetical refrigeration cycle for one section of an AMR [40]

### 3.3 Material and Metrics

The typical cycle used in prototype devices is known as the *active magnetic regenerator* (AMR). Active regeneration was first proposed to overcome the limited entropy change found in magnetocaloric materials. The use of materials with other caloric modes in similar applications is receiving increased attention [41]. These materials may also be used in an active regenerator leading to a more generic description of an active *caloric* regenerator (ACR). The efficiency of an ACR depends on the intrinsic properties of the active material; hence, selecting suitable materials is a crucial step in developing efficient systems. We use the phrase *screening metrics* to describe quantities that are derived from measurements of material properties and subsequently used to rank and compare materials in terms of suitability in an ACR cycle.

The development of experimental and numerical tools to understand the behavior of single layered and multi-layered regenerators manufactured with promising MCM has been extensively discussed in the literature [20,42]. However, material preparation, experimental characterization of the MCM properties, and the development of reliable computational tools can make numerical and experimental methods expensive and time consuming. A number of metrics to identify promising materials for use in magnetic cycles have been proposed which can potentially speed up the process of designing an AMR [43]. While a metric which ranks individual materials is useful, defining criteria for use in multi-material layered regenerators is also needed. There has been little work in validating metrics and comparing their usefulness against numerical or experimental AMR studies.

In the following sub-sections, several materials with first order and second order phase transition are selected and their properties are briefly discussed. Select properties and metrics used to rank magnetocaloric materials are described. And finally parameters used to quantify the performance of a material in a device are introduced.

### 3.3.1 Gd and its alloys

Due to their favourable properties, rare earth metals and their alloys have been widely investigated as magnetocaloric substances [2]. The magnetic transition temperature can be varied by alloying, making these material very interesting for magnetic heat pump applications at temperatures ranging from cryogenic to near ambient.

Gadolinium (Gd) is considered as the benchmark material for room temperature magnetic refrigeration systems. MCE in Gd is widely studied and the magnetocaloric effect in new materials are often compared to the MCE of Gadolinium [2]. This material exhibits a second order transition from paramagnetic to ferromagnetic with a Currie temperature of 295 K [44]. Fig. 9 (a) [19] shows the temperature dependence of heat capacity and MCE for Gd for different magnetic fields up to 10 Tesla. The peak observed in the zero-field specific heat curve identifies the second order transition temperature from ferromagnetic to paramagnetic state. The applied magnetic field is observed to have noticeable impact on the behaviour of specific heat curve of Gd. With increasing magnetic field, the specific heat curve becomes wider and the peak location shifts to higher temperatures. Fig. 9 (b) shows the MCE of Gd for different magnetic fields. MCE shows a nearly symmetric magnetocaloric effect which has a peak near the Curie temperature. Unlike specific heat, increasing magnetic field does not shift the location of peak MCE; however, it increases the magnetocaloric effect which is a typical behaviour observed in ferromagnets. The MCE of Gd is linearly dependant on the applied field at lower temperatures away from the Curie temperature; however, the MCE becomes non-linear with field, decreases at higher applied fields, near the transition [2].

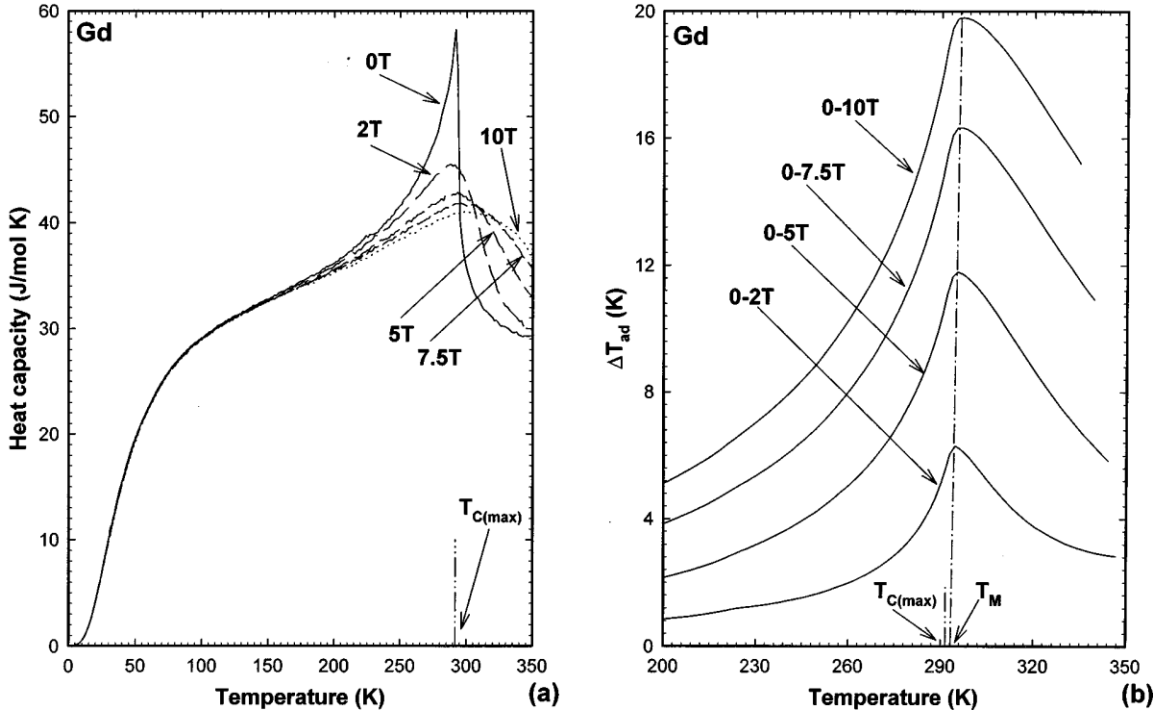


Fig. 9 Magnetic properties of Gadolinium as a function of temperature and field. a) Specific heat of Gadolinium as a function of temperature and b) Adiabatic temperature change for Gadolinium as a function of temperature for applied fields of 0, 2, 5, 7.5, and 10 T. $T_{c(max)}$ shows the temperature corresponding to the maximum specific heat in zero applied magnetic field, and $T_M$ is the temperature corresponding to maximum adiabatic temperature change.[45] [19]

It is observed that impurities can significantly alter the magnetic properties of Gd [46] and rare earth elements [47]. On the other hand, by alloying Gd with select rare earth elements such as Tb, Dy the transition temperature of Gd alloy can be shifted without significantly altering its MCE [48].

### 3.3.2 Mn based MCM

FOM's have received more attention in the last decade. Franco et al. [44] discuss different families of materials suitable for magnetic refrigeration applications. An FOM family with potential for use in AMR cycles is MnFe(P,As) alloys. In 2002, the so-called *giant magnetocaloric effect* (GMCE) was reported for this class of material [49]. The

transition temperature is tunable between 200 K to 350 K by changing the As/P ratio without losing the large MCE [50]. Although thermal hysteresis is present, it is relatively small (less than 1K). Beside thermal hysteresis, another drawback with this material is the use of As which is a toxic material. Later, this problem was addressed by replacing As with Si and, to achieve higher MCE comparable with the As family, Ge was combined with Si and a new family of FOMs were discovered $MnFe(P_{0.89-x}Si_x)Ge_{0.11}$. Unfortunately, thermal hysteresis increased significantly with this new family of FOMs [51]. Recently, $MnFeP_{1-x}Si_x$ compounds were studied further and reported to show large magnetocaloric effects [52]. This family of material do not contain any toxic components; however, they can show large hysteresis as well. It was later reported that with varying Mn:Fe and P:Si ratios, giant magnetocaloric effect and small thermal hysteresis can be achieved [53]. Although MnFe(P,As) alloys may not be ideal for AMR applications due to their toxicity and limited range of effectiveness, they are very interesting for research on AMRs comprised of layers of materials with varying transition temperature (because of large MCE, small hysteresis, availability, and tunability of the transition point) [54,55] .

### 3.3.3 Material selection metrics

From the early work of Wood and Potter [56] to more recent studies of Engelbrecht and Bahl [57], and Aprea et al. [58], the impacts of adiabatic temperature change and magnetic entropy change on the performance of MCMs have been studied. To characterize the capacity of a material for generating cooling power, Wood and Potter

define the *refrigerant capacity* (*RC*) as the reversible work to operate between $T_{\text{cold}}$ and $T_{\text{hot}}$ for isothermal heat absorption at $T_{\text{cold}}$, i.e.

$$RC \equiv -T_{cold}\Delta S\left(T_{cold}\right)\times\left(T_{hot}-T_{cold}\right). \tag{6}$$

A modified definition was suggested as a useful parameter to measure cooling capacity *q*, [38]:

$$q = -\int_{T_{cold}}^{T_{hot}} \Delta S(T,P,\Delta H)_{p,\Delta H}\, dT. \tag{7}$$

Both Eqs. (6) and (7) are a measure of the area defined in *T*-*s* space which can be interpreted as the minimum work input needed when operating between $T_{\text{cold}}$ and $T_{\text{hot}}$.

Because the magnetic entropy change is bounded by the total change in magnetization and the applied field, as discussed by Sandeman [59], a *maximum* RCP can be defined by,

$$RCP_{\text{Max}} = \int_0^{\infty} \Delta S(T,H_{\text{Max}})dT = M_{sat}H_{\text{Max}} \tag{8}$$

where $M_{sat}$ is the saturation magnetization. Although Eq. (8) is known to provide an upper limit to the available work in a system, it has not been widely used as a material screening metric.

Other metrics used to rank materials include peak entropy change $\left|\Delta S_{\text{Max}}\right|$, peak adiabatic temperature change $\Delta T_{\text{Max}}$, and combinations weighted by temperature span. Two widely used versions to identify promising MCMs are *RCP*(s) and *RCP*(T) [43,44,57,60,61] *:*

$$RCP(S) = -\Delta S_{\text{Max}} \times \delta T_{FWHM} \tag{9}$$

$$RCP(T) = \Delta T_{\text{Max}} \times \delta T_{FWHM} \tag{10}$$

where subscript *Max* refers to the maximum, or peak, value and *FWHM* refers to the full width at half maximum of either $\Delta S(T)$ or $\Delta T_{ad}(T)$. A common practice is to plot $\Delta T_{\text{Max}}$ against $\Delta S_{\text{Max}}$ for different materials [59] in order to create an Ashby map [62]. It is usually considered that materials with large $\Delta T_{\text{Max}}$ and $\Delta S_{\text{Max}}$ (upper right area of an Ashby map) would perform better in an AMR system. Based on this approach, a metric can be defined as follows:

$$RCP(TS) = \Delta T_{\text{Max}} \Delta S_{\text{Max}} \tag{11}$$

A number of other metrics have been reported where a heat metric is normalized by a work transfer [59,63]. These forms can suggest some measure of efficiency. While they are potentially good metrics for screening, they are not considered here where the focus is useful cooling power.

With the development of FOMs that exhibit high $\left|\Delta S_{\text{Max}}\right|$, but often lower $\Delta T_{\text{Max}}$ compared to SOMs, understanding the effectiveness of available metrics in identifying suitable materials for AMR applications is increasing in importance. To the knowledge of the author, there has been no rigorous study to determine how these metrics correlate with performance in an AMR cycle.

### 3.4 Summary

In this chapter the basic thermodynamics of AMRs were explained and the magnetocaloric materials used in the current study were presented. The techniques used

for selecting material for AMR applications were introduced and the metrics used for performance analysis in this research were described. In the proceeding chapters, details of experimental and numerical methods will be explained, and simulations and measurement results will be presented.

# Chapter 4 Device Configuration

The final aim of many research studies is to develop efficient magnetocaloric heat pumps. To achieve this objective, numerical models are used to investigate the impacts of various parameters on the performance of an AMR with the goal of optimizing the design. Many times, the numerical studies focus on the regenerator and neglect the impacts of device configuration – losses related to the way a specific device is constructed. Numerical models which can effectively predict the performance of real devices must consider the impacts of configuration losses. Methods to implement system effects in numerical models are needed so as to achieve good agreement between the simulated and experimental observations. In this chapter, the configuration losses inherent to an AMR system are defined and discussed. An experimental method to measure the loss coefficients of a device is presented. The experimental apparatus used in the current thesis is introduced and the procedures and protocols for experimental data collection are explained.

## 4.1 Configuration Losses

An active magnetic device consists of several parts besides the regenerators themselves: fluid flow system, magnets, heat exchangers, piping, and insulation. Many different designs exist and design choices tend to weight some losses higher than others. Part of the engineering challenge is to quantify the trade-offs for a system configuration

and to optimize the system as a whole. Here we define *configuration losses* as mechanisms *external* to the active regenerator that impact performance.

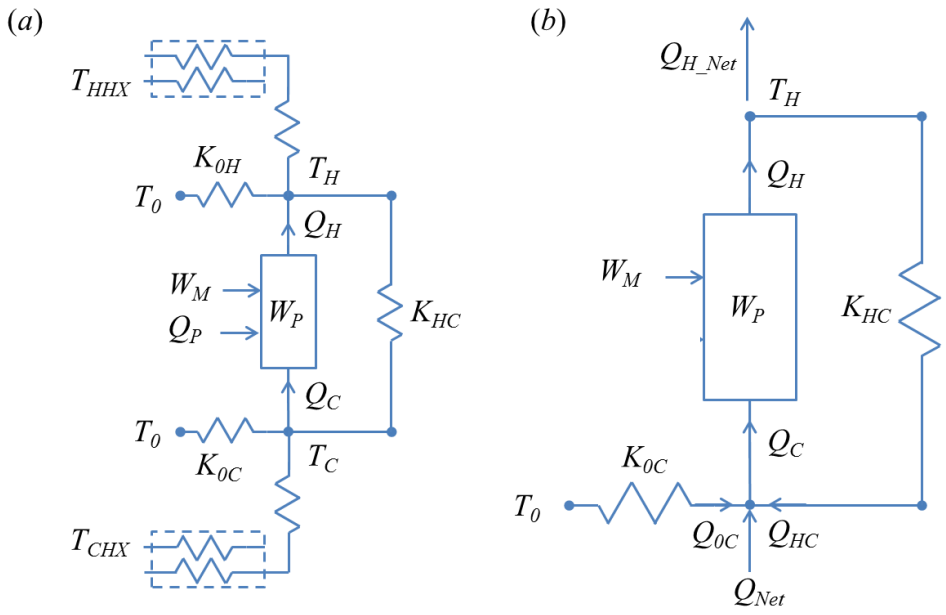


Fig. 10 (a) A schematic of heat transfer losses in an AMR system, and, (b) a simplified model which considers only two main configuration related loss mechanisms: heat leaks to the cold section from the environment and the hot side.

Fig. 10 (a) represents a model of configuration losses external to the regenerator. Depending upon the operating temperature span of the regenerator, the aspect ratio, and the design of the casing holding the regenerator, heat leaks through the surrounding structure can lead to decreases or increases in performance [64]. While not often considered, imperfect thermal isolation may actually help a device obtain a larger temperature span when operating above the environmental temperature. Other configuration losses can arise from dead volumes and heat exchanger ineffectiveness. Finally, a configuration may be selected which minimizes thermal leaks, but results in situation where demagnetization is significant. This cannot be shown in the schematic as

a resistor; instead, it acts as a reduction in the effective variation in magnetic field which is the driving force for magnetic work.

Figure 1 (b) shows a simplified model where only two thermal loss mechanisms related to configuration are considered: heat leaks between the cold side of the regenerator and the environment, and between the warm and cold sides of the system. The magnitudes of these thermal interactions are assumed to be determined by the specific thermal resistances in the device. The heat leak, $Q_{0C}$, between the cold end at $T_C$ and the ambient at $T_0$ is given by,

$$Q_{0C} = K_{0C}\left(T_0 - T_C\right) \tag{12}$$

where $K_{0C}$ is the effective thermal conductance. Likewise, the thermal interaction between the warm side of the system and the cold side is determined by the conductance $K_{HC}$ ,

$$Q_{HC} = K_{HC}\left(T_H - T_C\right). \tag{13}$$

The effect of external heat leaks is to reduce the available net cooling power of the system, $Q_{NET}$. The gross cooling power, $Q_C$, seen by all the regenerators in the device as represented in Figure 1 (b) is,

$$Q_C = Q_{NET} + Q_{0C} + Q_{HC} \ . \tag{14}$$

It is important to note that the notation used in Fig. 10 and in the equations above is for a *system* which can be comprised of an arbitrary number of regenerators, $N$. Because configuration losses are those of a complete device, we have worked with a system

representation; however, a similar schematic and set of equations could be written for a single regenerator. The convention we will use here is that upper case subscripts represent the entire system, whereas, lower case subscripts will be for a single regenerator. Thus, the net load for the device, $Q_{NET}$, would result in an effective net load per regenerator, $Q_{net}$, such that, $Q_{NET} = NQ_{net}$.

In the following sections we describe how the heat leaks and cooling powers are determined for the experimental apparatus used in this work.

## 4.2 Heat Leak Coefficients

Ideally, an AMR model would be validated using measured boundary conditions on the regenerator which would include gross cooling power, $Q_c$, parasitic heat leaks through the regenerator shell transverse to the flow direction, $Q_p$, and the gross heat rejection, $Q_h$. In the device used for this work, applied load, $Q_{NET}$, is the independent variable used to measure performance. Assuming a well-insulated shell, the transverse heat leak, $Q_p$ is assumed negligible. Validation of a regenerator model then requires knowledge of the resistances coupling the cold side to the environment and the hot side. These resistance values are calculated by measuring steady state temperature and heat rates when the device is not working as described below.

The conductance values, $K$, can be estimated experimentally by removing the regenerators and filling the void with insulating material. In this case, with a temperature difference between the hot and cold side of the device, the dominant mechanism for heat

leak between these two temperatures is assumed to be due to $K_{HC}$. A steady-state energy balance on the cold side with the device not operating is now,

$$Q_{HC} = Q_{0C} \tag{15}$$

and,

$$\left(\frac{K_{HC}}{K_{0C}}\right)^{*} = \frac{T_C - T_0}{T_H - T_C} \tag{16}$$

By performing a number of experiments where $T_H$ is varied and $T_C$ and $T_0$ are measured, the left side of Equation (16) is determined.

A second set of experiments are performed with a range of applied loads such that,

$$\begin{aligned} Q_{NET} &= Q_{HC} + Q_{0C} \\ Q_{NET} &= K_{HC}\left(T_C - T_H\right) + K_{0C}\left(T_C - T_{amb}\right) \end{aligned} \tag{17}$$

Making use of the previous experiments and Equation (16),

$$Q_{NET} = K_{0C}\left(\frac{K_{HC}}{K_{0C}}\right)^{*}\left(T_C - T_H\right) + K_{0C}\left(T_C - T_{amb}\right) \tag{18}$$

$K_{0C}$ is determined using the conductance ratio determined with the previous experiment, varying $Q_{NET}$ and measuring $T_C$ and $T_H$ via.

$$K_{0C} = \frac{Q_{NET}}{\left(\frac{K_{HC}}{K_{0C}}\right)^{*}\left(T_C - T_H\right) + \left(T_C - T_0\right)} \tag{19}$$

Finally, $K_{HC}$ can be estimated by using $K_{0C}$ calculated from Equation (19),

$$K_{HC} = K_{0C}\left(\frac{K_{HC}}{K_{0C}}\right)^{*} . \tag{20}$$

### 4.3 System Performance Metrics

The cooling power of the regenerator is the cycle-average rate of energy transfer across the cold boundary – this is defined as the *gross* cooling power for a regenerator. The regenerator gross cooling power is calculated based on the cycle averaged enthalpy flow at the cold end of the AMR neglecting pressure variations,

$$Q_c = \frac{1}{\tau_C}\oint \dot{m} c_p (T_C - T_f(t))dt \tag{21}$$

The gross cooling power of the device, $Q_C$, due to all $N$ regenerators is (note that a lower-case subscript is for a single regenerator, while an upper case subscript represents a device):

$$Q_C = NQ_c \tag{22}$$

A variety of COP definitions are possible [65] and can be useful for comparing different materials, regenerators, or systems. The COP definition we consider includes the effects of regenerator losses and thermal leaks of the device, but only focuses on the work inputs to the regenerator. By doing this, we are neglecting the mechanical inefficiencies of the device. This perspective gives what we call the *configuration* COP,

$$COP_{config} = \frac{Q_{NET}}{W_M + W_P} \tag{23}$$

where $W_M$ is the magnetic work and $W_p$ is the pumping work. Magnetic work is the amount of work input into the system through the magnetic field. In other words, this work acts as the available energy which could be changed into cooling power or could be lost due to irreversibilities. The net cooling power, $Q_{NET}$, is determined using Equation (14). The denominator is calculated using an energy balance on the AMR, $Q_H - Q_C$. Finally, the second law efficiency is calculated using Equation (24) [65]

$$\eta = COP\left(\frac{T_H}{T_C} - 1\right). \tag{24}$$

### 4.4 Experimental Apparatus

The experimental device used in this work is an apparatus known as PM II which uses permanent magnets for the field source. The device has been described in detail elsewhere; we will focus only on the characteristics most relevant for the results presented here [66,67].

The PM II device utilizes concentric nested Halbach arrays to generate a magnetic field (Fig. 11). A cylindrical regenerator fits inside the Halbach arrays and, as the magnets rotate in opposite direction, a time varying field is created in the bore where the regenerators are fixed. In a recent study, the design and development of multipolar halbach arrays for magnetic refrigeration applications are numerically investigated [68]. Increasing the number of poles, can increase the rate the refrigerant is magnetized and demagnetized which can potentially increase the refrigeration capacity. For the work described here, two-pole Halbach arrays are utilized and spherical particles of gadolinium

are the MCM. The heat transfer fluid used inside the system is a mixture of water and glycol (80%-20%) on volumetric basis. A reciprocating fluid displacer is used to pump the fluid from the hot heat exchangers, through the regenerators, cold heat exchangers and vice versa.

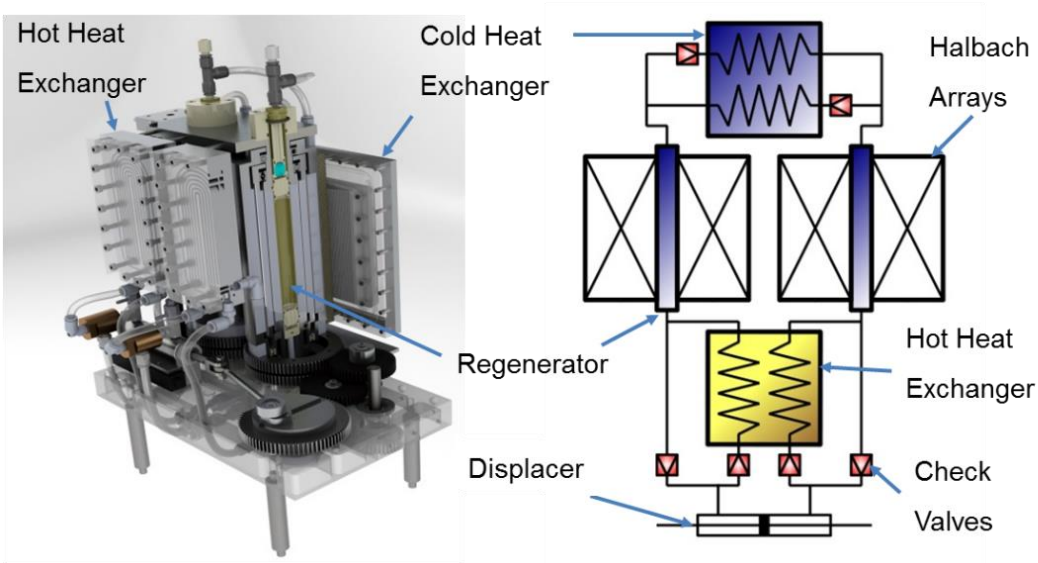


Fig. 11 PM II AMR test apparatus. This apparatus is made up of two active regenerators. A displacer is employed to pump heat transfer fluid through the system and check valves are used to control the flow direction. As the displacer moves to the left, fluid will be pumped from the hot heat exchanger, through the regenerator on the left and to the cold heat exchanger. During this period the left regenerator is in low field mode. At the same period, since the regenerator on the right is in high field mode, the fluid flows from the cold heat exchanger, through the right matrix, returning to the displacer. As the displacer now moves to the right, the fluid flows in opposite direction. In this period, the right regenerator will be in low field mode and the left one will be in high field mode.

Fluid flow is generated using a double-acting displacer combined with unidirectional valves to control the flow direction [66,69]. Assuming sinusoidal displacer motion, instantaneous mass flow rate is a function of displacer stroke, $s$, operating frequency, $\omega$, density, $\rho$, and displaced cross sectional area, $A_d$ .

$$\dot{m}(t) = \rho A_d \frac{s}{2} \omega \cos(\omega t - \frac{\pi}{2}) \tag{25}$$

The total flux density created in the empty bore is determined by the vector addition of the field generated by each magnet. The flux density in the bore of the magnet as a function of angular position is described by Equation (26).

$$B(\theta) = B_{\max} \frac{\sqrt{2}}{2} \left|1 + \cos^{0.5} \theta\right| \tag{26}$$

### 4.4.1 Regenerators

As discussed in [66] the choices of regenerator morphology are limited by manufacturing capabilities associated with the selected refrigerant. Traditionally passive regenerators have been constructed from crushed irregular particles, spherical particles, parallel plates, stacked wire mesh and stacked parallel tubes. Fig. 12 shows samples of different regenerator geometries [66]. With three dimensional printing technology and manufacturing techniques, channelled microstructures are becoming more widely available (Fig. 13). One of the key advantages of channelled microstructures is that they can be manufactured in pucks of material with different transition temperatures, and then stacked in a regenerator to construct a layered regenerator.

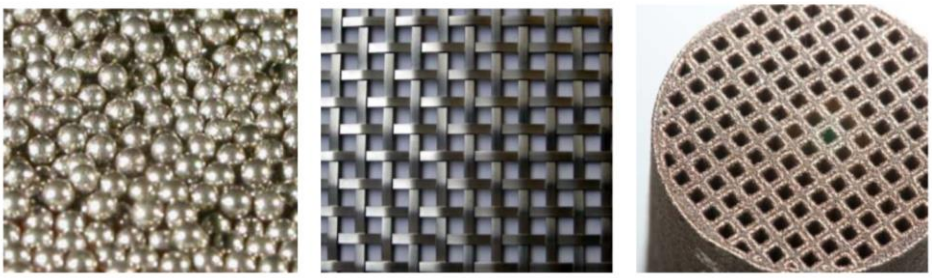

Fig. 12 Samples of different regenerator geometries [66]

Two types of regenerators are usually used in AMR applications [64]: fixed bed and rotary bed regenerators. In a fixed bed regenerator, the flow direction may be controlled by a valving system such as rotary or check valves and the field strength is varied by magnet motion. In a rotary regenerator, the time-varying magnetic field is created by movement of the regenerator with respect to the magnet. Unidirectional pumps are often used in combination with valves to generate an oscillating flow. PM II uses fixed cylindrical regenerators (Fig. 14) with the regenerator mounted inside the Halbach arrays.

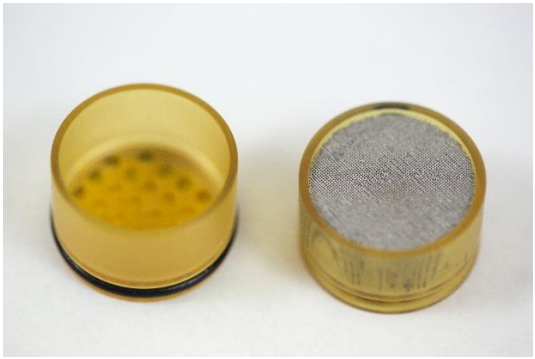

Fig. 13 Channeled microstructure puck and the puck housing designed for PM II cylindrical regenerators.

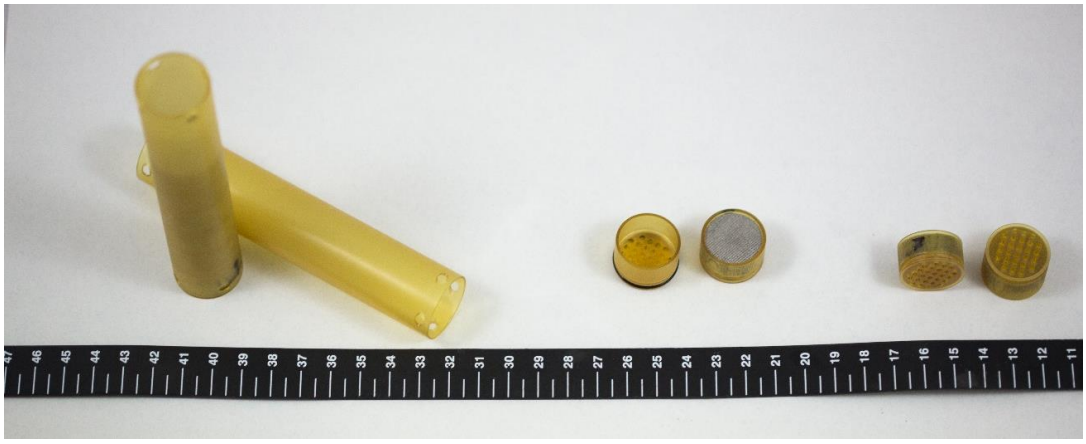

Fig. 14 Cylindrical regenerator beds used for fixing material in PM II device. On the right, sample channeled microstructure refrigerant and their housing are presented. Multiple pucks with different transition temperatures can be mounted inside a regenerator to create a multilayered AMR bed.

## 4.5 Testing Procedures

As briefly discussed in Chapter 1, one of the problems with FOMs is hysteresis. The term hysteresis refers to the history dependence of properties. Some of the emerging FOMs that exhibit large MCE, also show large magnetic and thermal hysteresis. To elaborate, when a material shows magnetic hysteresis, it means that the magnetic properties of the material are dependent on the previous state or phase of the material. This behaviour can affect the measurements of specific heat and adiabatic temperature change. This phenomenon may result in irreversibilities over the magnetic cycle which can affect the performance of an AMR. Because of hysteresis, the measurement procedure must be carefully defined when reporting performance of an FOM in an AMR.

### 4.5.1 Testing Protocols

The terms warming (heating) or cooling are used to indicate the way temperature history of a sample or the AMR is varied between each data point measurement. For a heating measurement of specific heat, the sample temperature is fixed at a temperature below the transition temperature. For the consecutive measurements, the sample temperature is slowly increased. The opposite protocol is used for cooling. Fig. 15 shows a sample measurement of specific heat following heating and cooling measurement protocols.

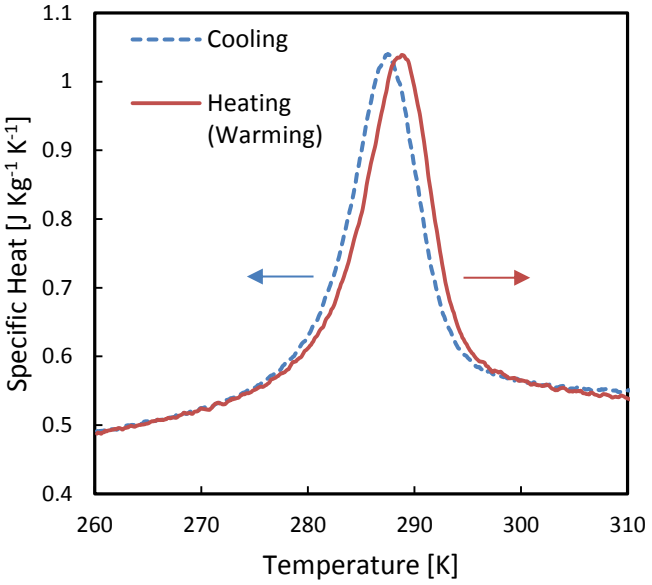


Fig. 15 Specific heat as a function of temperature for 0 T of applied field measured by utilizing heating and cooling protocols for an $MnFeP_{1-x}As_x$ sample.

To measure the performance of a material in an AMR, the heat rejection temperature is fixed to the desired value, the load on the cold side of regenerator bed is set, and then the device is started at the desired operating conditions (i.e. frequency and displaced volume). The term warming (heating) indicates that the starting heat rejection temperature is selected to be below the temperature of peak specific heat of the coldest material in the cascade. The steady-state cold side data point is collected and then the heat rejection temperature is increased and the temperature span for a new data point is measured. A cooling process refers to the procedure where the heat rejection temperature is selected to be higher than the warmest layer in the cascade. After steady-state is reached and data is recorded, the heat rejection temperature is reduced and the next measurement is made. Fig. 16 shows a sample measurement of device performance

following heating and cooling measurement protocols. It is observed that for a SOM material (Gd) the two protocols result in similar temperature spans; however, for FOM material, heating and cooling procedures result in different temperature spans for the same operating conditions.

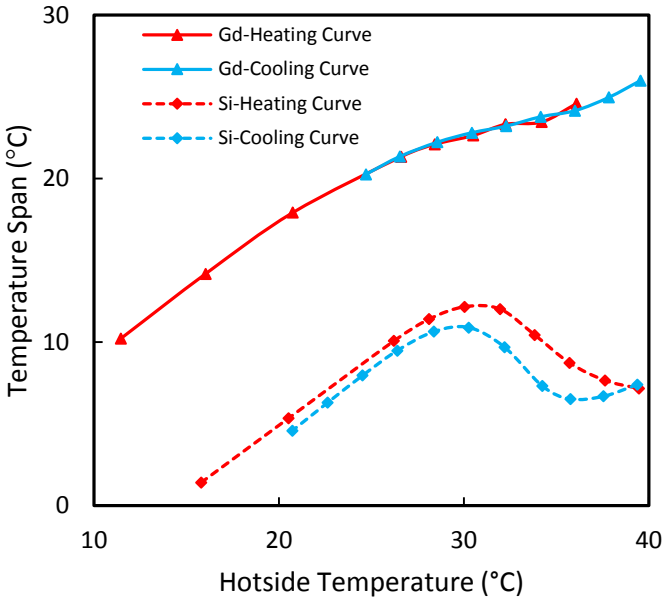


Fig. 16 A comparison of performance of an AMR using SOM (Gd) and FOM ($MnFeP_{1-x}Si_x$) sample following heating and cooling device performance measurement protocols.

The results shown in Figure 16 have not been fully explained by AMR researchers. This problem will be investigated in detail in Chapter 8.

## 4.6 Summary

In this section the device configuration is studied. Configuration losses are defined as mechanisms external to the active regenerator that impact performance and an experimental method is proposed to measure the external heat loss coefficients. The experimental test apparatus used in this study is introduced and the testing procedures

utilized for experimental measurements are outlined. In the following chapter, the details of developing the numerical model will be discussed.

# Chapter 5 Numerical Model Development

The combined effects of non-linear material properties, varying magnetic field, and time-dependent heat transfer and fluid flow make an AMR a complicated system to model. Parameters related to system design such as fluid flow unbalance which can negatively impact the performance of an AMR [10], also add to the complexity of performance modeling.

Because of complexity and the 1D nature of simple AMRs, many researchers use one dimensional models instead of two or three dimensional models. In a one dimensional model, the transverse temperature gradient in the solid matrix is neglected; however, by using proper correction factors this effect can be accounted for. This technique has been practiced by several researchers [28,70,71]. Comparing the results with experimental measurements has shown that one dimensional models with proper correction factors are capable of modeling the performance of systems closely. In this study a 1D numerical model is developed and validated against experimental measurements.

## 5.1 AMR Model

### 5.1.1 Governing equations

The active magnetic regenerator is modeled using a one-dimensional approximation to determine temperature as a function of space and time $T(x, t)$ for the solid matrix and fluid. Performance parameters such as cooling power, work input and efficiency are then

post-calculated. Using an energy balance for a control volume comprised of solid and fluid phases, the following governing equations can be derived [72].

$$\frac{m'_f L c_p}{\tau_B}\frac{\partial T_f}{\partial t^*} + \dot{m} c_p \frac{\partial T_f}{\partial x^*} = \frac{\partial}{\partial x^*}\left(\frac{\alpha A k_{f,eff}}{L}\frac{\partial T_f}{\partial x^*}\right) + h_{eff} A'_w L\left(T_s - T_f\right) + \left|\frac{\dot{m}}{\rho_f}\frac{\partial p}{\partial x^*}\right| \quad (27)$$

$$\frac{m'_s L c_B}{\tau_B}\frac{\partial T_s}{\partial t^*} = \frac{\partial}{\partial x^*}\left(\frac{(1-\alpha) A k_{s,eff}}{L}\frac{\partial T_s}{\partial x^*}\right) + h_{eff} A'_w L\left(T_f - T_s\right) + \frac{m'_s L c_B}{\tau_B}\frac{\partial T_{ad}}{\partial t^*} + Q'_{other} L \quad (28)$$

$T$ is temperature, $x^*$ is the dimensionless spatial coordinate (normalized by regenerator length, $x = x^* L$) and $t^*$ is dimensionless time coordinate (normalized by blow period, $t = t^* \tau_B$). Subscript *f* refers to fluid and subscript *s* refers to solid. $m'_f$ is the entrained mass of fluid per unit length of the regenerator $m'_s$ is the mass of MCM per unit length, $c$ is specific heat, $A'_w$ is the surface area of the solid matrix per unit length, $\tau_B$ is the blow period, $k_{eff}$ and $h_{eff}$ are the effective thermal conductivity and convective heat transfer coefficient respectively, $A$ is the cross-sectional area of the regenerator, and α is porosity. In Equation (27) the terms from left to right represent: energy storage, enthalpy flow by fluid displacement, thermal diffusion, convective transfer between the solid and the fluid, and viscous dissipation. The terms in Equation (28) are: energy storage in the solid, axial heat conduction, convective heat transfer between solid and fluid, and magnetic work effects. Equation (28) includes a generic source term, $Q'_{other}$ which can be used to represent source terms such as eddy-current heating.

The effective conductivity is a local volume-averaged property dependent on the conductivity of each phase and the porosity of the porous media given by [73]. For the

fluid, both conduction and dispersion are considered in the diffusion term such that for a one dimensional analysis, $k_{eff}$ is given by [74].

$$k_{eff} = k_{static} + k_f D^d \tag{29}$$

$k_{static}$ is the static component of effective conductivity which is the conductivity of a packed bed when there is no flow, $k_f$ is the intrinsic fluid conductivity and $D^d$ is the dispersion coefficient calculated using [73],

$$D^d = 0.75 \varepsilon PrRe \tag{30}$$

where $\varepsilon$ is the porosity and,

$$Re = \left( \frac{\dot{m}_f}{A\rho} \right) \frac{d_h}{\mu} \tag{31}$$

$d_h$ is the hydraulic diameter.

The convection coefficient is determined using the correlation suggested by Wakao et al. [75],

$$h = \frac{(2 + 1.1 Re_f^{0.6} Pr_f^{1/3}) k_f}{d_p} \tag{32}$$

where $Re_f$ is the Reynolds number based on particle diameter, $d_p$, and $Pr_f$ is the Prandtl number. An effective convection coefficient is used, $h_{eff}$, to account for temperature gradients in the matrix material. The effective value is determined by a degradation factor, *Df*, as described elsewhere [70] [76].

$$h_{eff} = Df \times h \tag{33}$$

$$Df = \left( \frac{1}{1 + \frac{Bi}{5}\phi_H} \right) \tag{34}$$

$$Bi = \frac{hd_p}{2k_s} \tag{35}$$

$$\phi_H = \left( 1 - \frac{4}{35Fo} \right) \tag{36}$$

$$Fo = \frac{\alpha \tau}{\left( \frac{d_p}{2} \right)^2} \tag{37}$$

Pressure drop is determined using the modified Ergun equation as suggested by Macdonald [77] and used in other studies on packed beds [78].

$$\frac{\Delta P}{L} = \frac{(1-\alpha)}{\alpha^3} \frac{\rho u_s^2}{d_p} \left[ \frac{180\mu(1-\alpha)}{\rho u_s d_p} + 1.8 \right] \tag{38}$$

where $u_s$ is the superficial velocity of the fluid, $L$ is the length of the regenerator, $\mu$ is dynamic viscosity.

### 5.1.2 Boundary conditions

In each cycle there are two blow periods. In the first blow the fluid flows from the hot reservoir (hot side of the regenerator) to the cold reservoir (cold side of the regenerator) and in the second blow, the fluid flows from the cold side to the hot side of the regenerator. The boundary conditions are defined by the following equations:

Hot to cold blow ( $\dot{m} \geq 0, \bar{B} = B_{Low}$ ):

$$T_f(0,t) = T_h, \frac{\partial T_f(L,t)}{\partial x} = 0 \tag{39}$$

$$\frac{\partial T_s(0,t)}{\partial x} = 0, \frac{\partial T_s(L,t)}{\partial x} = 0 \tag{40}$$

Cold to hot blow ( $\dot{m} \le 0, \bar{B} = B_{High}$ ):

$$T_f(L,t) = T_c, \frac{\partial T_f(0,t)}{\partial x} = 0 \tag{41}$$

$$\frac{\partial T_s(0,t)}{\partial x} = 0, \frac{\partial T_s(L,t)}{\partial x} = 0 \tag{42}$$

To reach steady state condition, initial transient effects need to dissipate. A periodic steady state condition is determined using a periodic boundary condition:

$$T_f(x,t) = T_f(x,2\tau) \pm \delta T \tag{43}$$

$$T_s(x,t) = T_s(x,2\tau) \pm \delta T \tag{44}$$

For the results reported here, the tolerance of the model, $\delta T$ , is set as 0.001 K.

## 5.2 Material Properties

A mixture of water-glycol (80%-20% on volume basis) is used as the heat transfer fluid. Temperature dependent properties of this fluid mixture are determined using empirical equations. The magnetization, specific heat, and entropy of SOM material are modelled by combining mean field theory (MFT) and Sommerfeld Model [79] with the Debye approximation [2]. MFT determines magnetization as a function of temperature and field, and, with appropriate Maxwell relations, the magnetic contributions to specific heat and entropy.

### 5.3 Field Waveform

In some numerical studies a step change for the magnetic field is used instead of a time varying wave form [20,29,80]. This approach significantly reduces time and complexity of the simulation, and tends to represent a best-case for the field change seen by the AMR. Trevizoli et al. looked at the effects of using a step change field instead of a rectified sinusoidal field profile [81]. In their study, the low and high field values for the discrete field approach were based on the minimum and maximum values of the continuous field wave form. This led to over predicting the performance of the system. Unfortunately, the PM II device uses a wave form which is varying throughout the cycle and is not well-represented by a step change. The ability to model the device using a step change would be beneficial as it leads to significantly faster solutions. In order to use a step change model instead of the complete wave form, the average values for low field and high fields for a step model need to be calculated based on the device field wave forms. PM II device utilizes a displacer system to pump fluid during low field and high field periods continuously (Design principles and performance details of PM II are further discussed in [66,67]). Two averaging techniques are used to estimate the effective low field and high field values based on the device waveform.

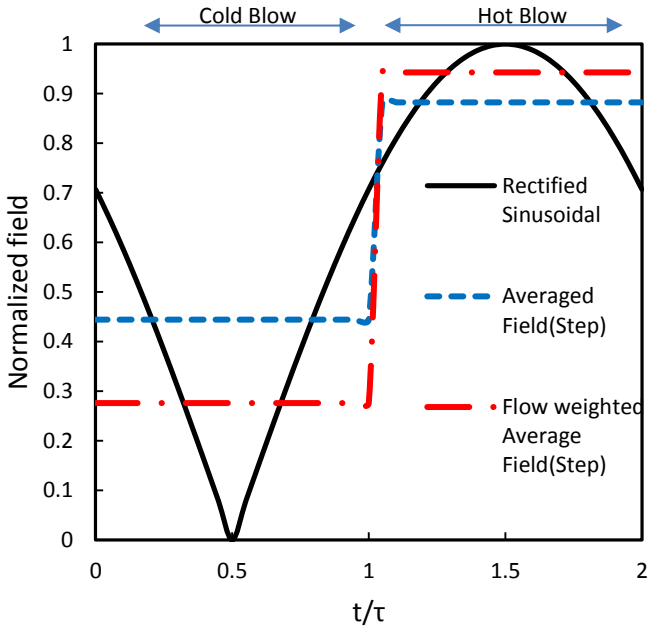


Fig. 17 Different field wave forms analyzed.

The field wave form for PM II is described by Equation (26) and is shown graphically in Fig. 17 as the rectified sinusoid. In addition, we show two different discrete field profiles representing step changes. Each is calculated using the applied fields during the blow periods. In one case, a conventional average is calculated for each blow period, $B_{avg}$, using

$$B_{avg} = \frac{1}{\tau_B}\int_0^{\tau_B} B(t)dt \tag{45}$$

The magnitude of applied field is normalized using the maximum field, $B_{\max}$,

$$B_{Normalized} = \frac{B(t)}{B_{\max}} \tag{46}$$

Although this averaging technique is simple and effective in estimating the applied field for the step model, it does not include the flow waveform effects. The conventional averaging method is most useful when the flow is uniform during each blow period. However, if the flow waveform changes significantly during the period, this method will be less accurate in replacing the complete waveform. In PM II device, the fluid flow is non-uniform during each blow period and follows a sinusoidal behavior. Different fluid waveforms can lead to different performance whereas a simple averaging technique for field is unable to discriminate between these cases.

When replacing the field waveform with a step change model, it is important to include the effects of fluid waveform and synchronization with field in the average high and low field values. As a result a second definition, $B_{favg}$, is proposed which uses the mass flow rate given by Equation (25) to determine a flow weighted average for each blow period,

$$B_{favg} = \frac{1}{m_d} \int_0^{\tau_b} \dot{m}(t) B(t) dt \tag{47}$$

The integral of the mass flow waveform gives the total displaced mass $m_d$ . As will be shown in Section 6.1.1, using the flow-weighted average field in a step-change approximation closely matches the results using the full magnetic field waveform. All simulation results that follow use the flow weighted average field with a step change approximation.

## 5.4 Demagnetization

As a material is exposed to a magnetic field, $H$, the material will be magnetized, $M$. A magnetic dipole moment is created inside the material and a demagnetization field $H_d$ can be defined resulting from this magnetic pole. The demagnetization field, depends on magnetization of the material and the shape of the sample [82],

$$H_d = N_d M \tag{48}$$

where $N_d$ is the demagnetization factor which is only a function of the geometry of the specimen. The internal field felt by the sample, $H_{in}$, is determined by the external field and the demagnetization field,

$$H_{in} = H_a - H_d \tag{49}$$

where $H_a$ is the applied field.

Demagnetization is a problem in nearly all permanent magnet based devices and arises due to both matrix and regenerator geometry. A simulated representation of relative local field when at high field in PM II is shown in Fig. 18. The average of this profile results in a 16% reduction in applied field. Burdyny et al. modeled a geometry similar to the PM II and used a constant scaling of applied field to account for demagnetization effects [29]. Using the same approach here, the scaled local field, $H_{mat,}$ is assumed to be 84% of the applied field, $H_a$. Other approaches to correcting for demagnetization are possible, but an average scaling is simple and numerically efficient. We briefly examined averaged scaling and position dependent scaling of field on local

magnetic work and solid temperature distribution. We found the differences between them to be small and so we use the average scaling approach.

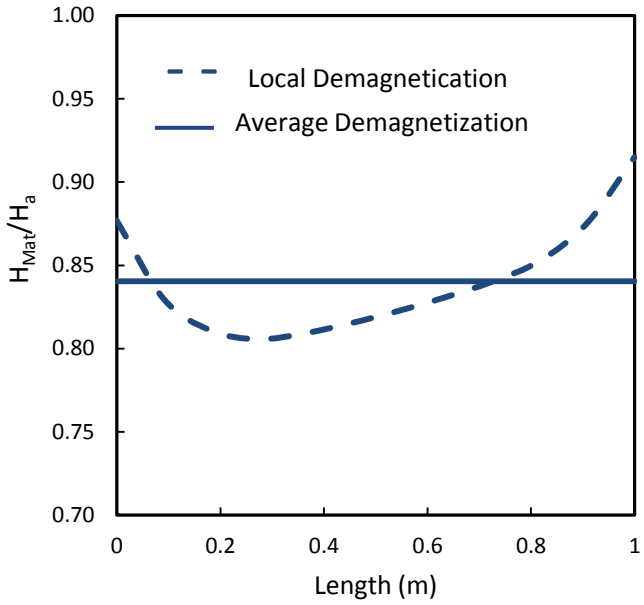


Fig. 18. Demagnetization as a function of location used for simulations. The solid line shows the average value of demagnetization and the dashed line shows location dependent value of demagnetization along the regenerator for a temperature span of 282-302 K

## 5.5 Solution Method

The governing equations are discretized both in time and space with Galerkin-Petrov method described in [83] and implemented in the Matlab PDEPE solver. The number of elements used to discretize the governing equations is an important factor that affects the performance of the model. It is essential to have sufficient density of mesh points at sensitive locations in order to capture accurate behavior. These locations can be, the points where the boundary conditions are applied (i.e. the contact points between the layers and the end points where the hot and cold fluid enters the regenerator in each blow

period) or locations where rapid variations in properties occur. Due to the sudden change of properties, a sufficient resolution of elements is needed to properly capture the temperature profile behavior.

One approach is to use a fine uniform mesh throughout the regenerator and to increase the number of elements until a solution is reached which is not mesh dependent. Although increasing the number of elements, reduces the discretizing and truncation error, it can increase the solution time significantly and also increases the round off errors [84]. Therefore, a higher accuracy using fewer elements is desirable. To keep the number of elements low and simultaneously increase the accuracy of the model, a sinusoidal mesh generation technique is used. Fig. 19 shows the distribution of elements in a uniform meshing technique compared to the sinusoidal meshing technique.

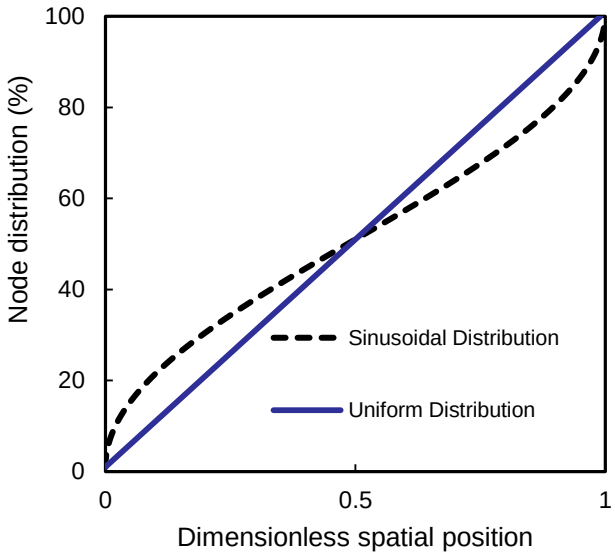


Fig. 19 Distribution of elements in a uniform meshing technique compared to sinusoidal meshing technique.

With a uniform mesh distribution, 10% of the elements are within 10% of the ends; however, using a sinusoidal method, more than 20% of the nodes are located within 10% of the ends. The difference is more significant if we compare locations within 5% of the regenerator end points. With this method, we can significantly increase the number of elements at the end points without increasing the total number of elements. This is a mesh distribution technique to increase the density of elements in locations where higher resolution is needed without increasing the total number of nodes and solution time significantly. For a single layer we have found this to be an effective meshing technique.

### 5.5.1 Grid Study

A grid sensitivity study comparing uniform and sinusoidal meshing is used to select the number of elements. We use a sinusoidal mesh distribution technique to discretize the spatial coordinates. A reference case is defined using sinusoidal meshing with 200 elements. A temperature span of 19 K, frequency of 1 Hz, a displaced volume of 10 $cm^3$, and experimental parameters described later in Table 1 are used. Cooling power and magnetic work are calculated for different element numbers and compared to the selected case. For 20 nodes and sinusoidal mesh, the values calculated for magnetic work and cooling power are 0.05% and 2.3% higher than what the reference case with 200 elements. A similar accuracy is achieved with a uniform mesh of 60 elements; however, the solution time increases by about 300%.

The above results are obtained for gadolinium which has a smooth second order transition. If we examine first order material, the number of elements may need to be

increased significantly and element distribution becomes more critical. In this case, the use of sinusoidal meshing may not be valid as the material properties are more sensitive to field and temperature. For the SOM simulations that follow 40 nodes with a sinusoidal spatial distribution are used.

## 5.6 Summary

In this section, the details of developing a numerical model for performance analysis of an AMR were discussed. The governing equations were presented and boundary conditions were outlined. Relevant equations for calculating heat transfer coefficient between solid and fluid phases were presented and field and flow waveforms used in the model were discussed. Finally the solution method was briefly explained. In the following chapter, the numerical simulation results will be validated against experimental measurements. After validating, the model is used to perform parametric studies on some of the key operating conditions and device configuration parameters.

# Chapter 6 Model Validation and Parametric Study

In this section, we use the developed model to analyze the performance of PM II under different operating conditions. First we compare simulations using step change in field to the actual applied field waveform. Then we compare the results obtained from the numerical model to experimental measurements. After validating the performance, we use the model to investigate the system performance under a wider range of operating conditions. The effects of external losses on overall system performance are reported in Section 6.2.

## 6.1 Model Validation

### 6.1.1 Field Waveform

The performance of the model using step change wave forms for field ($B_{avg}$ and $B_{favg}$) are compared to results using the rectified sinusoidal wave form. Fig. 20 shows simulated temperature spans at zero (a) and ten watts (b) of net cooling power for rejection temperatures above and below the Curie point of gadolinium. For all conditions, the use of $B_{avg}$ underestimates temperature span by approximately 30% compared to results using the full wave form. The step change approach using the flow weighted average fields, $B_{favg}$, shows excellent agreement with the results obtained using the full wave form. Based on this finding, the step change approach using the $B_{favg}$ fields is used for all other simulations.

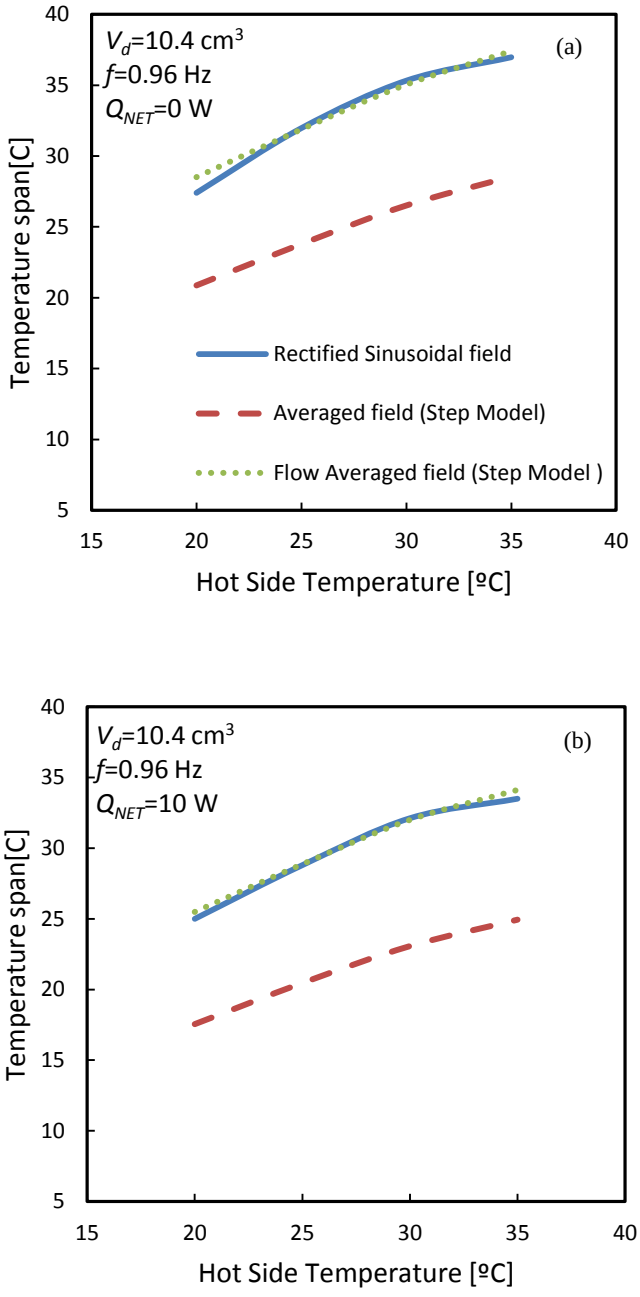


Fig. 20 Performance of the system when using rectified sinusoidal field wave form, averaged field and flow averaged field wave forms (Step Change Model).

### 6.1.2 Experimental Validation

To validate the predictive ability of the model, we compare simulated temperature spans with experimental values for zero and ten watts of net cooling power. Two different frequencies (0.5 and 1 Hz) and two different displaced volumes (10.4 and 20.8 $cm^3$) are considered. Configuration losses for the PM II device are included. The conductance values described in Section 4.1 are estimated to be $K_{HC}$ = 0.8 $WK^{-1}$ and $K_{0C}$ = 0.9 $WK^{-1}$. The experiments for determining the loss factors were performed with the regenerator matrices in the system which overestimates the value of $K_{HC}$. The impacts of this are considered by simulating an additional case with $K_{HC}$ reduced to 0.5 $WK^{-1}$.

Fig. 21 compares model results to experimental data where temperature span is plotted as a function of rejection temperature. Simulated results for the two different values of $K_{HC}$ are shown. The difference between model predications and measured data are less than 1 K in most cases which is on the order of the uncertainty of the experimental measurements. As expected, the effects of $K_{HC}$ tend to increase with temperature span. Depending on operating conditions, a $K_{HC}$ value of 0.5 or 0.8 $WK^{-1}$ may provide a better match to the data. For the remainder of this paper, $K_{HC}$ = 0.8 $WK^{-1}$ is used to study the performance of the system.

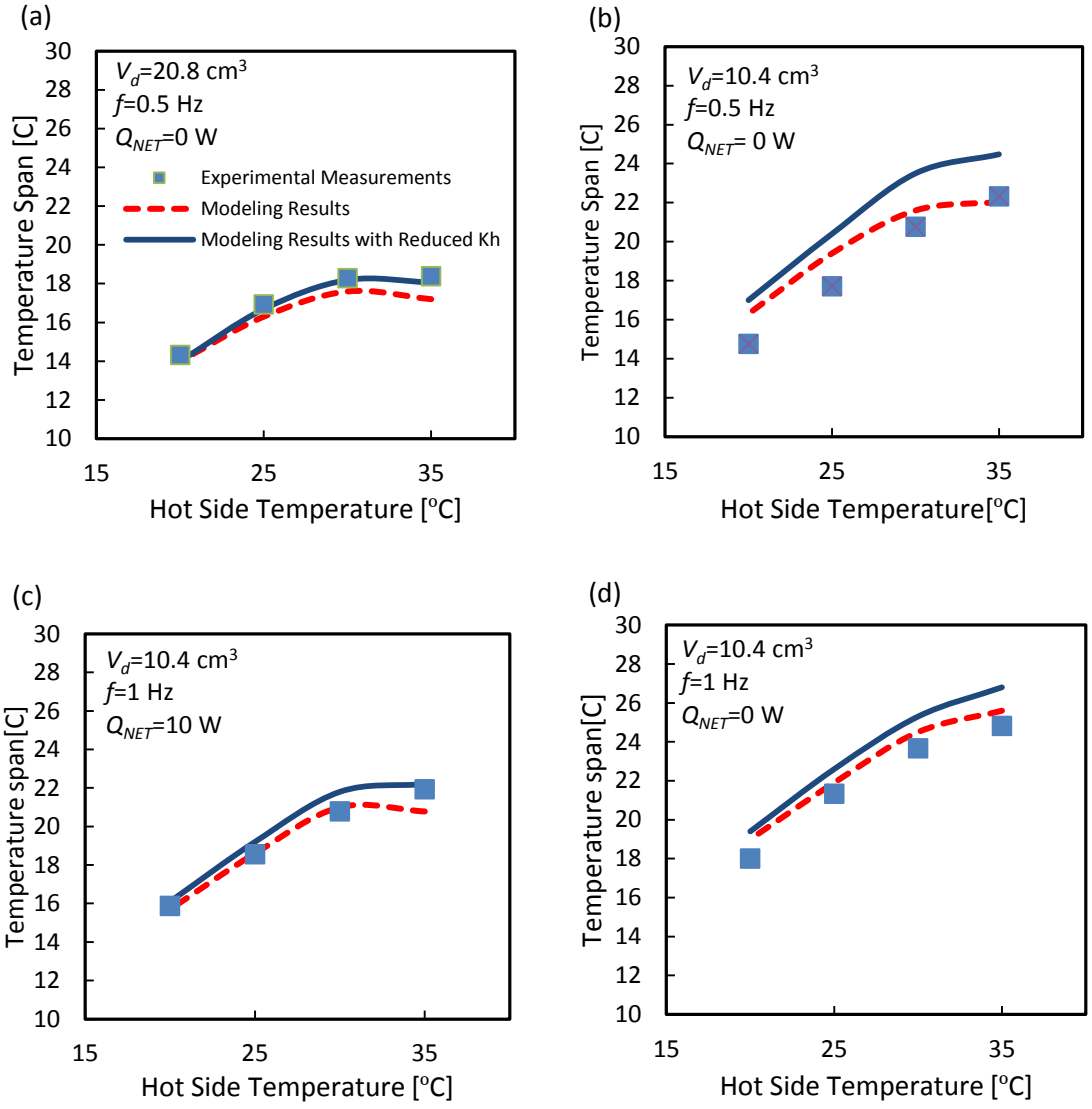


Fig. 21 Comparison between model prediction and experimental measurements (markers) for four different cases. The dashed lines show simulation results *($K_{HC}$=0.8)*. The solid lines show the modeling results when $K_{HC}$ is reduced to 0.5.

## 6.2 Parametric Study

To fully understand the impacts of configuration losses on AMR performance, we numerically explore operating conditions listed in Table 1. The ranges for parameter values correspond to possible operating points in the PM II.

Table 1 Regenerator properties and operating parameters for numerical simulations.

| **Parameter** | **Value** | **Units** |
|---|---|---|
| Matrix Material, $d_p$ | Gd spheres, 425-600 | [μm] |
| Mass of MCM (per regenerator) | 198 | [g] |
| Frequency, $f$ | 0.5, 1, 1.5, 2, 2.5, 3 | [Hz] |
| Hot side Temperature, $T_H$ | 295, 299, 303, 307 | [K] |
| Cold side Temperature, $T_C$ | 278, 280, 282, 284, 286, 288, 290 | [K] |
| Displaced volume, $V_d$ | 5.2, 10.4, 15.6, 20.8, 31.2 | [$cm^3$] |

The impacts of physical properties of the refrigerant on the performance of AMR are investigated elsewhere [85]. In this study, after comparing device performance with and without configuration losses, we determine the impact of operating conditions on COP. The efficiency is determined and conditions leading to maximum performance are identified.

### 6.2.1 Configuration losses

Configuration losses are quantified by comparing net and gross cooling powers. Results for rejection temperatures of 299 and 307 K are shown in Fig. 22 for a displaced volume of 10.4 $cm^3$. In each case, gross and net cooling power are plotted as a function of temperature span for each frequency. Ambient temperature is assumed constant at 293 K. The results show a monotonic decrease in cooling power with temperature span. At higher spans, cooling power reduces with frequency as compared to lower spans where cooling power increases with frequency. This is because cooling power is more sensitive to internal regenerator losses such as viscous dissipation and reduced thermal effectiveness at higher spans. Operating points close to room temperature exhibit smaller parasitic loads.

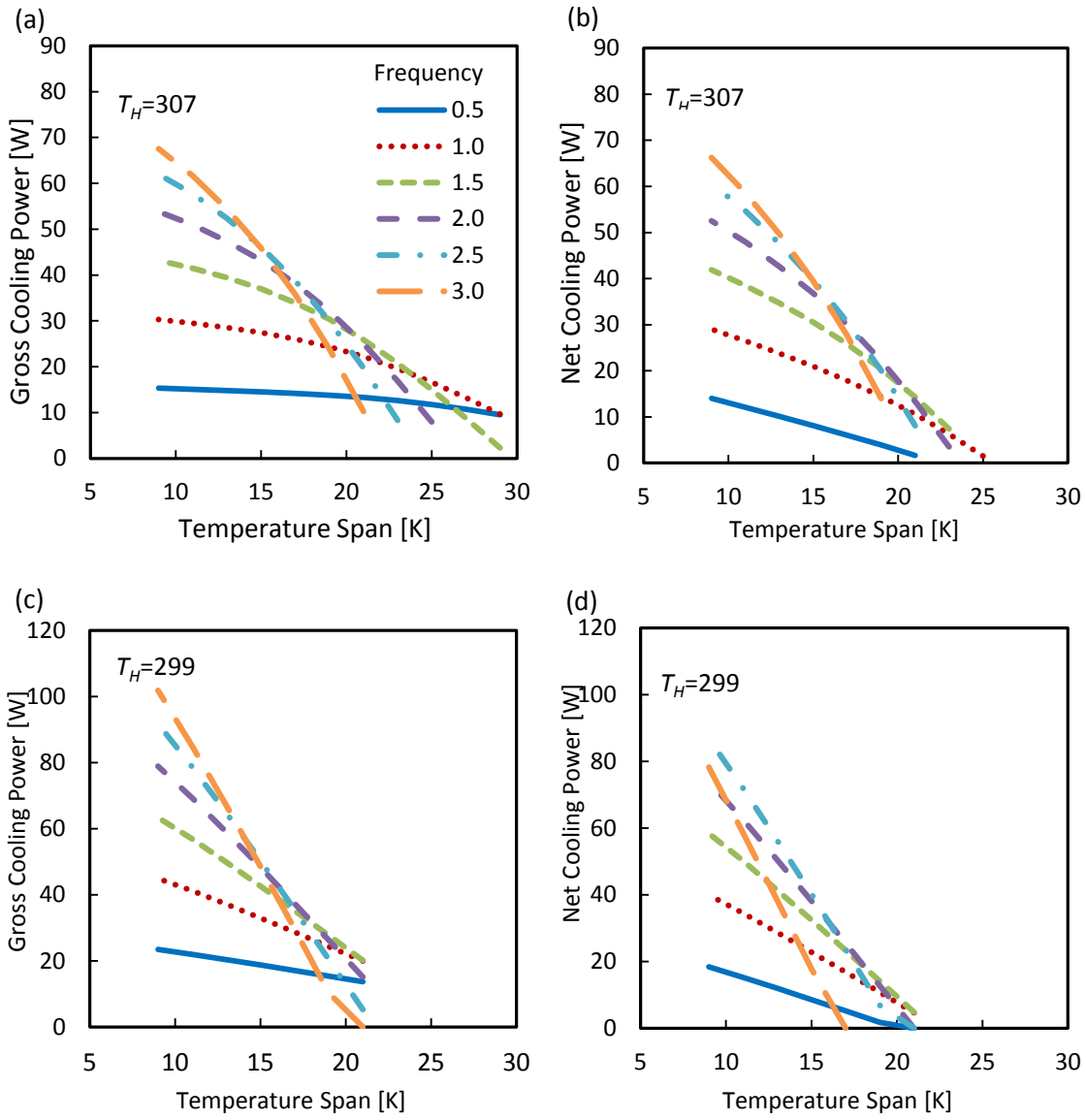


Fig. 22 Gross cooling power (a) and (c) and net cooling power (b) and (d) as a function of temperature span and frequency - (a) and (b) Hot side temperature is 307 K; (c) and (d) hot side temperature is 299 K. Displaced volume is 10.4 $cm^3$ for all cases.

The impact of configuration losses for two different displaced volumes are quantified in relation to gross cooling power in Fig. 23 where the percent difference is calculated using,

$$\text{Configuration Loss [\%]} = \frac{Q_{GROSS} - Q_{NET}}{Q_{GROSS}} \times 100 \ . \tag{50}$$

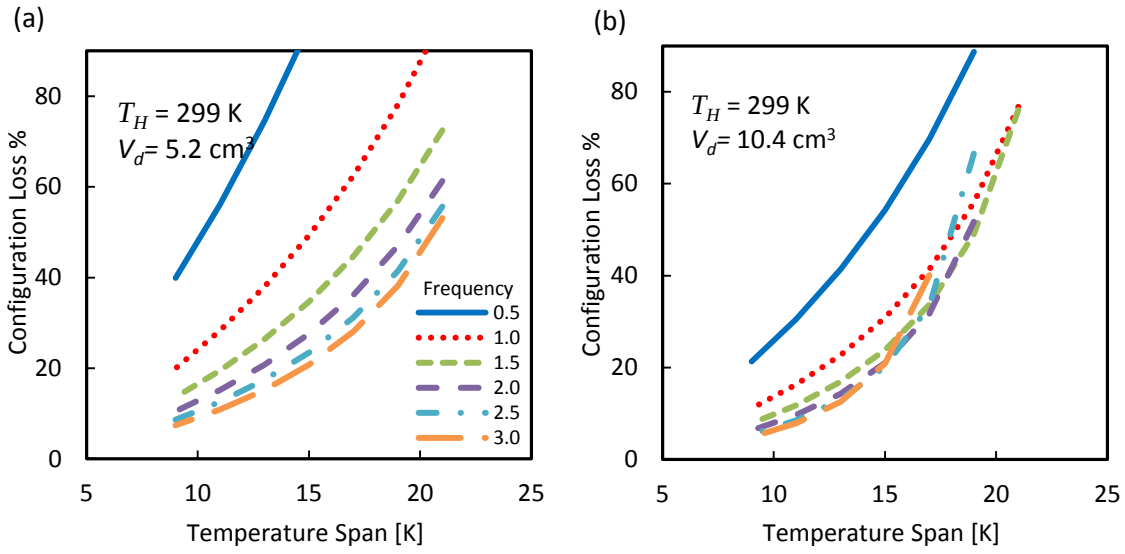


Fig. 23 Configuration losses as a function of temperature span and frequency.

Increasing the frequency will increase the rate of magnetic work input in the system; however, higher frequency also results in reduced thermal effectiveness. The combined effects of these parameters determine the cooling power of the system, and, increasing the frequency can sometimes lead to increase in gross cooling power (favorable effects of magnetic work input dominates the adverse effects of reduced thermal effectiveness) and vice versa.

### 6.2.2 Cooling power and efficiency

In a refrigeration system, we desire high cooling power at a reasonably high efficiency and temperature spans. Fig. 24 shows second law efficiency for the configuration (defined by equations (23) and (24)) as a function of net cooling power for different temperature spans. In Fig. 24, three different displaced volumes are

investigated. For each displaced volume, the efficiency of the configuration as a function of net cooling power is plotted. On each plot colors discriminate between different frequencies. Each data point represent efficiency for a specific cold side temperature. The temperature decrement between the data points connected with arrows are 2 K in decreasing order in the direction of the arrows (i.e. the cold side temperature starts at 290 K and reduces in the direction of the arrows by decrements of 2 K.). The dashed lines connect the points with the same cold side temperature where frequency increases from left to right.

As shown, decreasing temperature span will increase the net cooling power. Simultaneously the efficiency increases as the effects of the system losses on the net cooling power decrease. For $V_d = 5.2$ cm$^3$, as the frequency increases, (following the dashed lines in clockwise direction), the net cooling power increases. For higher displaced volumes, the net cooling power might increase or decrease depending on the frequency. Efficiency follows a similar trend. By increasing the frequency, efficiency increases to a peak and then decreases.

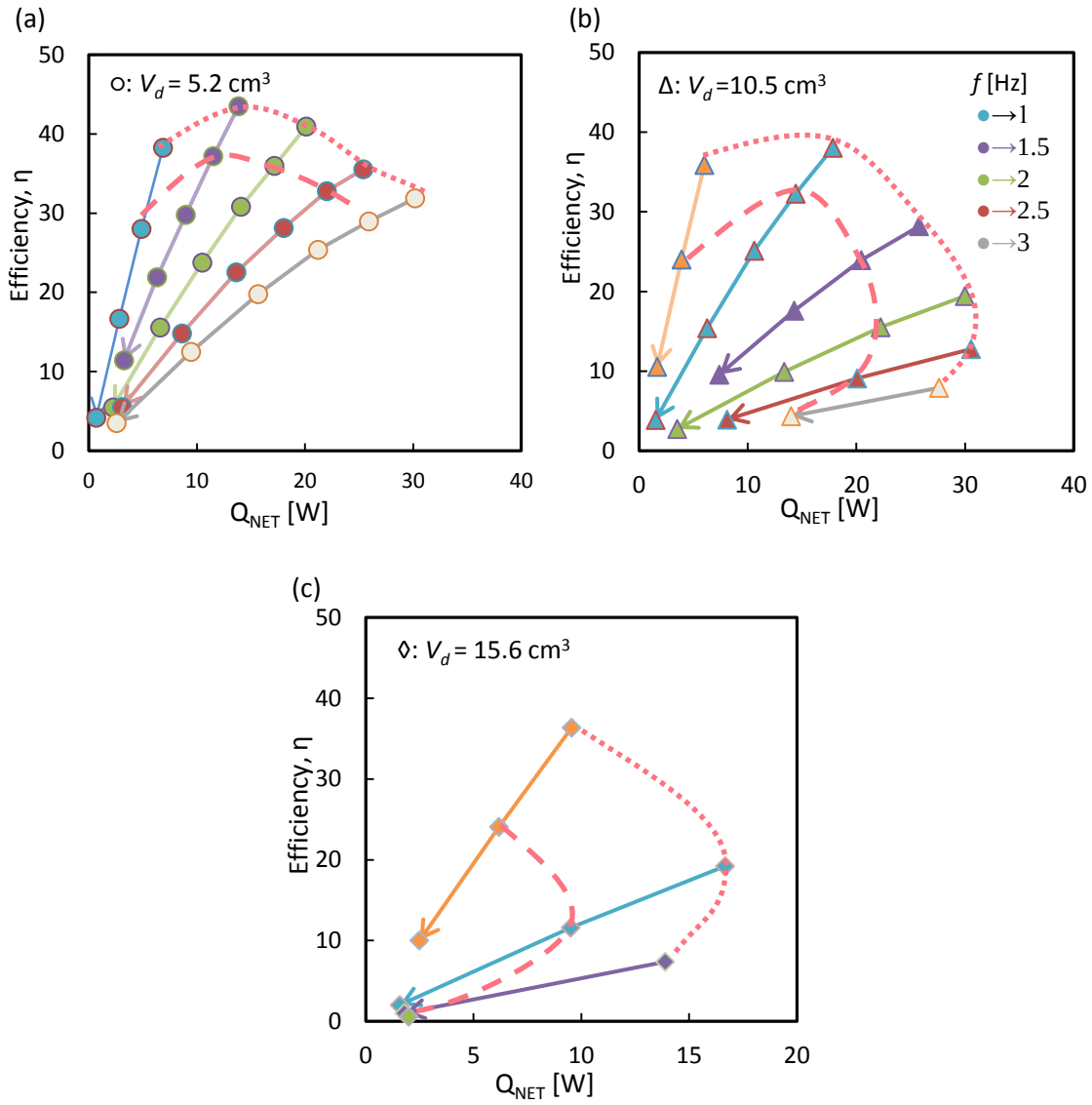


Fig. 24 Second law efficiency as a function of net cooling power for different temperature spans and $T_H$ = 307 K. a) $V_d$ =5.2 cm³, b) $V_d$ =10.4 cm³ c)$V_d$=15.6 cm³ (circle: 5.2 cm³, triangle 10.4 cm³, diamond: 15.6 cm³) the dotted line shows a contour of the same cold side temperature, $T_C$ = 290K, dashed line $T_C$ = 288 K, and as we move in the direction of the arrows, the cold side temperature reduces as: 290,288,286,284,282,280, 278 K.

In order to reduce the number of parameters, in Fig. 25 frequency and displaced volume are combined into one parameter $C_r = f \times V_d$ which can be interpreted as the capacity rate of the fluid (i.e. $C_r = \dot{m} c_p = \rho V_d f c_p$ since $\rho c_p$ is constant, varying $V_d f$

is equivalent to changing capacity rate.) Because the regenerator mass and material are fixed, varying capacity rate is also a proxy for varying utilization – the thermal mass of fluid displaced relative to the thermal mass of the regenerator. Fig. 25 shows the efficiency of the system versus net cooling power for varying capacity rates. All data presented in this figure is for $T_H$ = 300 K. Each marker style corresponds to a different displaced volume and data points are color coded for frequency. Data points can be classified in three different capacity rates. For each capacity rate there are two sets of data (two curves). One curve corresponds to a higher frequency and lower displaced volume, the second curve is for lower frequency and higher displaced volume.

At lower capacity rates, the efficiency curves are narrower with a larger peak compared to higher capacity rates. This means that at smaller capacity rates the system reaches higher efficiency with a smaller net cooling power. However, system efficiency is more sensitive to the net load compared to larger capacity rates where the performance of the system is more stable around the peak. It can also be seen that for a constant capacity rate, the system exhibits higher efficiency at higher displaced volumes. Therefore, having a higher displaced volume is more favorable than higher frequency. The difference between the frequency and displaced volume curves becomes smaller as the capacity rate increases. At higher capacity rates the temperature span is lower and, as a result, the thermal effectiveness of the regenerator has less impact on cooling power and efficiency.

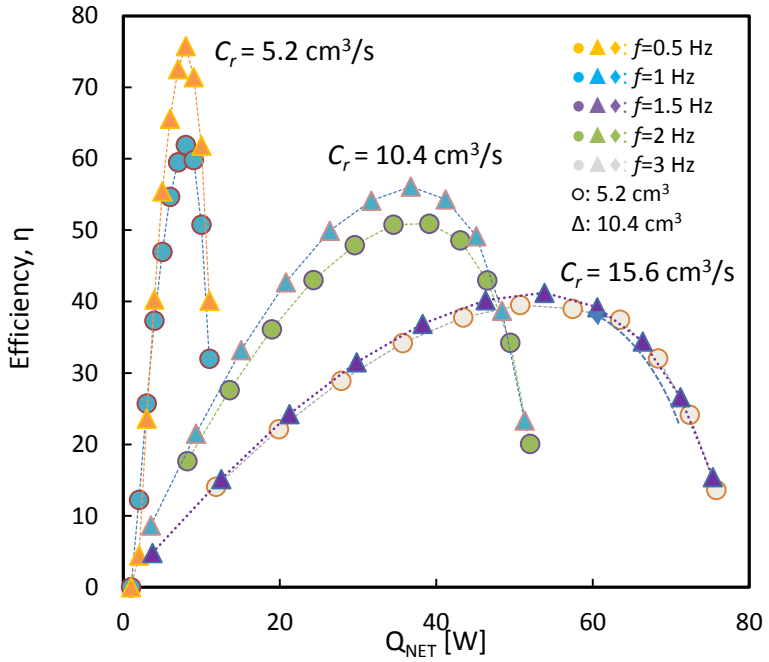


Fig. 25 Second law efficiency versus net cooling power for three different capacity rates at $T_H$=300 K.

### 6.3 Discussion

Numerical analysis and design of AMR systems relies upon reliable predictive ability. This arises from the use of appropriate numerical methods, sufficiently detailed physical models, and domains that capture the dominant physical mechanisms influencing AMR performance.

In terms of numerical methods, we show the benefits of using a sinusoidal distribution of elements over a uniform distribution for capturing sufficient accuracy while considering solution time as a criteria. Here we consider a single material AMR with properties given by a second order magnetic phase transition. In this case, the temperature and field dependent properties vary in a relatively smooth manner over the

entire AMR. Allocating more nodes near the ends of the AMR is beneficial as these locations are critical in determining heat absorption and rejection. The use of sinusoidal meshing may not be preferred with AMRs made up of large numbers of layers or where first order materials are used.

As with mesh generation, approaches that approximate system dynamics but reduce the computational domain are desirable. Because of the strong sensitivity of material properties to both temperature and field, reducing the temporal and spatial variability of field can lead to reduced solution times. The use of a mass-flow weighted field to define two discrete fields is found to give good results compared to the use of a complete field waveform. This greatly reduces iteration for material properties, such as specific heat, resulting in faster solutions. This is true even though the full cycle must still be modeled so that the mass flow waveform is captured. An appropriate averaging of flow over both blow periods may be possible to allow for a two-step cycle; however, this is an area for further research.

The impacts of configuration must be considered for the PM II system so as to separate device losses from AMR design and operating parameters. In this study, heat leaks between the hot side and cold side are assumed to arise as a parasitic load at the cold interface. Other modeling approaches explicitly include heat leaks through the walls of the regenerator housing in a distributed manner. This is an effective method; however, it may lead to longer simulation times due to the addition of a differential equation describing the housing [64,81]. Including the effects of heat leaks between the hot and cold ends of the system as well as between the environment and the cold end leads to

better model predictions. The effects of device losses should not be overlooked with any experimental device particularly when finding the maximum temperature spans. As spans increase, cooling power tends to decrease making the impacts of configuration losses more significant. Finding the maximum temperature span of a system without including configuration losses will most likely overestimate performance substantially. By including and quantifying the effects of device losses, the intrinsic efficiency of the AMR can be determined. In the case of the gadolinium regenerator characterized in this work, the efficiency can exceed 70% for low net loads. This finding suggests that through appropriate design and the use of materials with large magnetocaloric effect, potential system efficiencies can also be high.

## 6.4 Summary

In this chapter, a one dimensional, transient model was used to study the performance of an active magnetic regenerator. Sinusoidal meshing technique was used to discretize the governing equation. The impacts of configuration losses on performance was investigated and it was shown that configuration losses can lead to significant drops in performance of a typical magnetic refrigerator. Different flow and field wave forms were investigated and it was observed that step change model for applied field can be effectively used instead of full field wave form if the flow weighted average low and high field values are used. A detailed parametric study was performed on different operating conditions (i.e. frequency, displaced volume) and the results were presented. In Chapter 7, using the developed model, the efficacy of different techniques for selecting material

for AMR applications will be discussed and the correlations between the material selection techniques and optimal performance of a material in an AMR will be further examined.

# Chapter 7 Material Screening and Optimal Performance

In this chapter, the numerical model is used to study the performance of single magnetocaloric materials in an active magnetic regenerator cycle [32]. The model is used to investigate the performance of a regenerator of fixed size, matrix geometry, frequency, and magnetic field waveform using a range of materials with ordering characteristics represented by FOM and SOM transitions. The maximum performance of each material in terms of exergetic cooling power is calculated. The correlation between maximum performance and material properties such as peak adiabatic temperature change, peak isothermal entropy change, and other selected metrics is quantified. A sensitivity analysis determines the effects of varying absorption and rejection temperatures from the conditions for maximum performance.

A range of materials with different transition temperatures, entropy change, and specific heats are studied. Fluid properties, operating frequency, regenerator volume, particle size, thermal conductivity and density are fixed as listed in Table 2. Displaced volume, $V_d$, is varied with increment of 2.5 $cm^3$ to identify the optimum utilization for each material.

Table 2 Regenerator properties and operating parameters for numerical simulations.

| Parameter | Value | Units |
|---|---|---|
| Regenerator diameter | 2.2 | cm |
| Mass of MCM (per regenerator) | 143 | g |
| Density | 6.1 | g $cm^{-3}$ |
| Thermal Conductivity | 3 | $W(m.K)^{-1}$ |
| Frequency, $f$ | 1 | Hz |
| Displaced volume, $V_d$ | 5.2-27.5 ($\delta$ = 2.5) | $cm^3$ |
| Particle size | 125 | µm |
| Length of the regenerator | 12 | cm |
| Porosity | 0.49 | - |

## 7.1 Material Properties

MCM materials with properties representing SOMs and FOMs are considered. Magnetocaloric properties for seven second order materials are created using molecular field theory (MFT) modeling with parameters representing elemental Gd, Dy, Tb, and four different $Gd_xDy_{1-x}$ compositions ($0.5 \leq x \leq 0.92$). Experimental data for a single $MnFeP_{1-x}As_x$ composition (M1) with properties given in (Table 3 and Fig. 26) is used to create other hypothetical FOMs. The properties of this material are measured through VSM, DSC and direct adiabatic temperature change measurements.

Table 3 measured material properties for $MnFeP_{1-x}As_x$ (M1)

| $T_{Curie}$ [K] | FWHM [K] | $\Delta S$ [$Jkg^{-1}K^{-1}$] | $\Delta T_{ad}$ [K] | Field [T] |
|---|---|---|---|---|
| 287.25 | 2.96 | - | - | 0.0 |
| 292.1 | 2.98 | 12.74 | 3.23 | 1.0 |
| 294.45 | 2.98 | 14.50 | 4.65 | 1.5 |

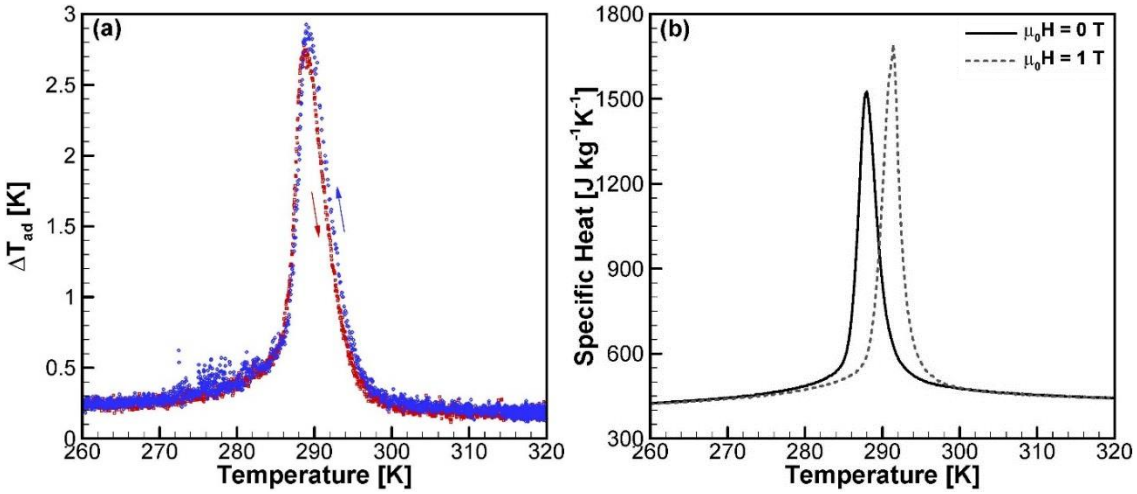


Fig. 26 Measured material properties as a function of temperature and field for $MnFeP_{1-x}As_x$ a) adiabatic temperature change for a field step change of 1.1 T, b) specific heats measured at two different fields of 0 and 1 T.

A set of fifteen first order materials are created (we call these *synthetic* materials, *S*) based on M1 ($MnFeP_{1-x}As_x$) behavior by varying the amplitude and width of the specific heat curves at low and high field. All materials are assumed to have magnetization given by M1 from 0 to 250 K so that ferromagnetic phase has the same isothermal entropy change as a function of field prior to the phase transition. Hysteresis is assumed negligible and the transition shift due to field is determined by the difference in temperature between the peak specific heats. Thermodynamically consistent data is created for synthetic materials by simulating specific heat using a Lorentzian curve and integrating to determine isofield entropy curves. Low and high field entropy are then interpolated to determine adiabatic temperature change as a function of temperature.

Eight synthetic materials, S1-S8, are synthesized by changing the specific heat curves while keeping the transition temperature constant. Seven additional cases, S9-S15, are synthesized where the zero field phase transition temperature is also changed. The

resulting FOMs are shown in Fig. 27-Fig. 29 in terms of heat capacity, entropy change, and adiabatic temperature change. The properties are for a low field and high field of 0.35 and 1.1 Tesla respectively. These values are selected based on the magnetic waveform of the PM II test apparatus [32][67].

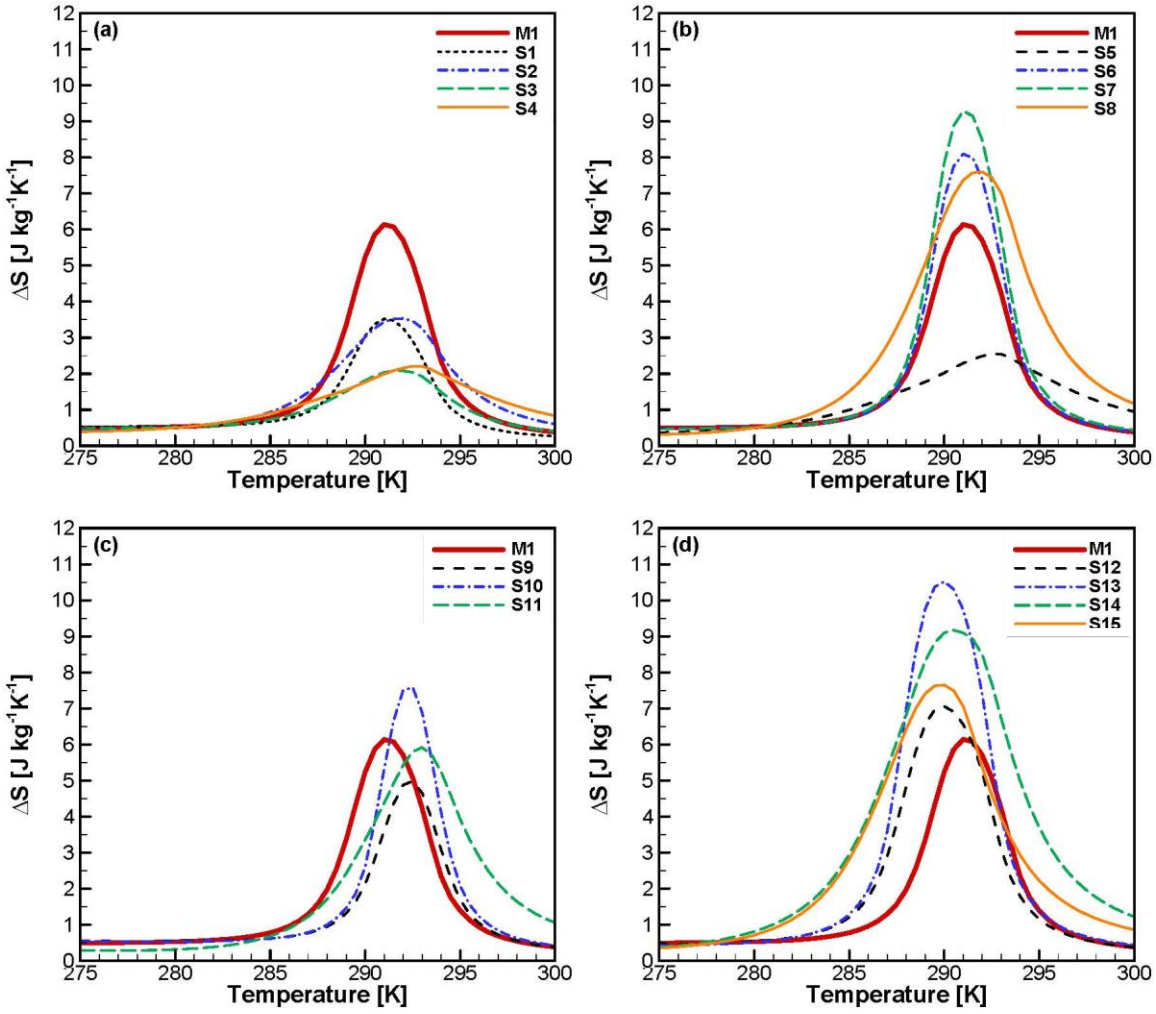


Fig. 27 Magnetic entropy change for synthetic cases (FOM). On each figure, M1 is plotted as the reference material and a number of synthetic cases are presented.

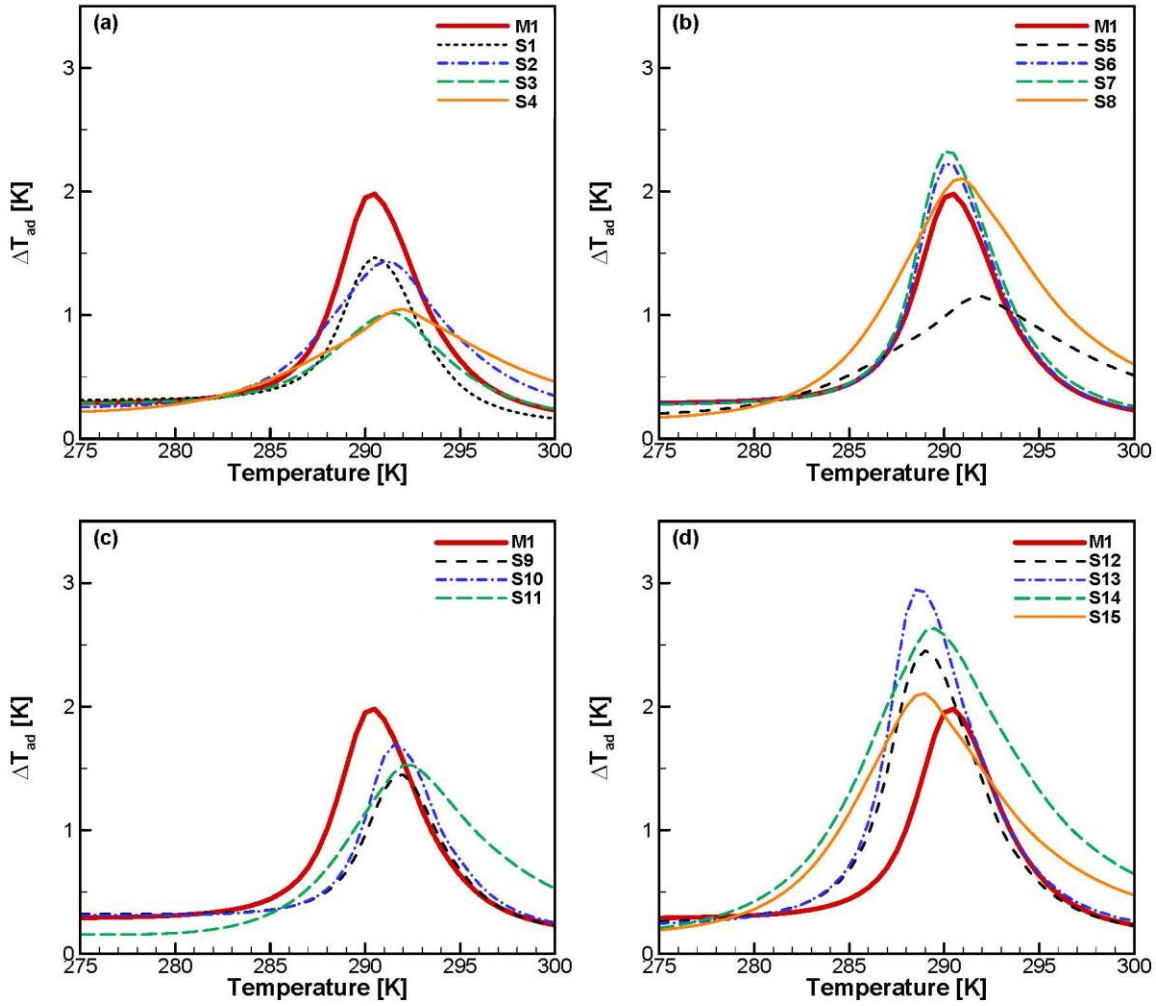


Fig. 28 Adiabatic temperature change for synthetic cases (FOM). On each figure, M1 is plotted as the reference material and a number of synthetic cases are presented.

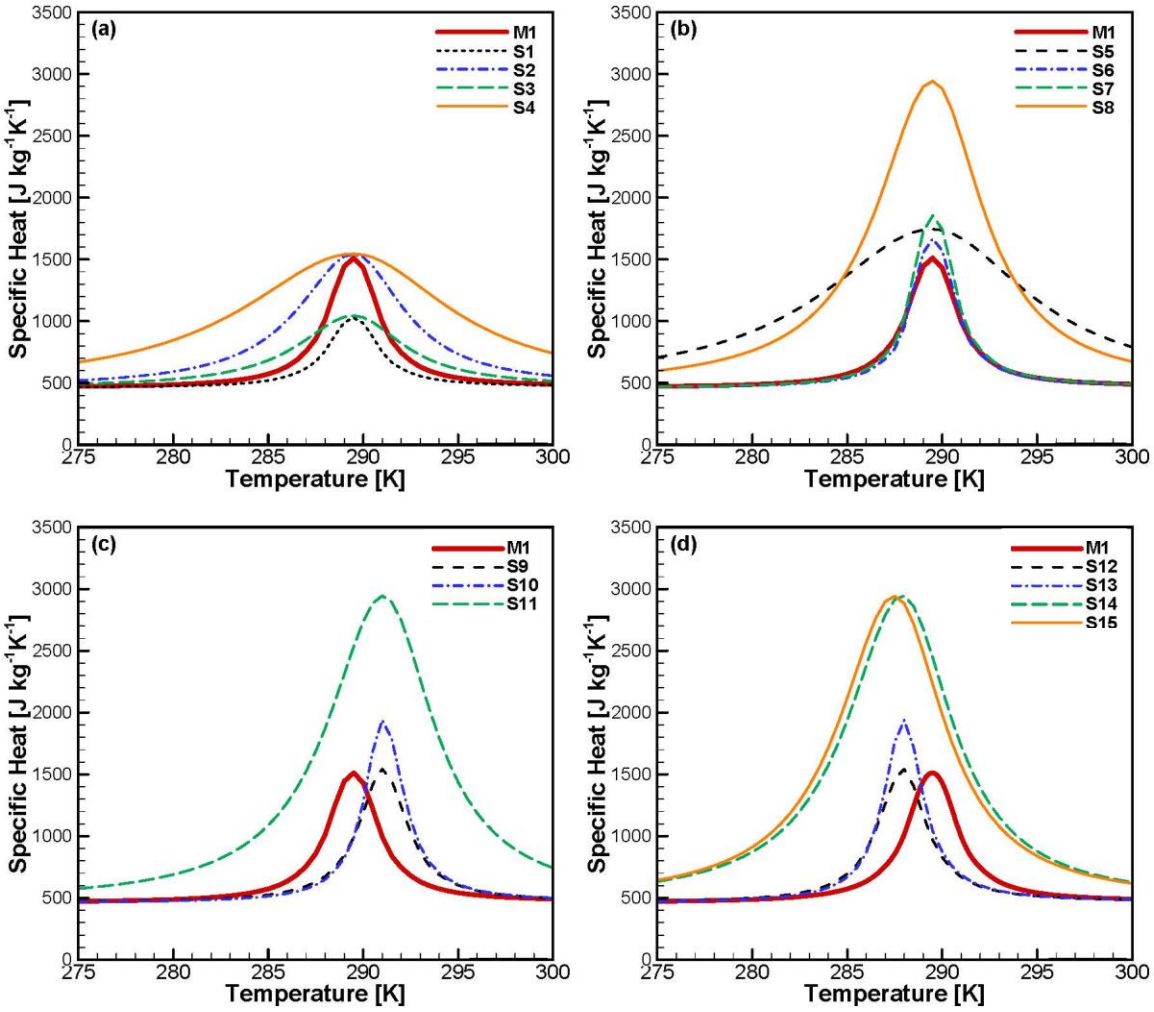


Fig. 29 Specific heat for synthetic cases at low field (0.35 T). On each figure, M1 is plotted as the reference material and a number of synthetic cases are presented.

In addition to the first order materials, seven cases of second order material are also simulated. The magnetization, specific heat, and entropy of these material are modelled by combining mean field theory (MFT) and Sommerfeld Model [79] with the Debye approximation [2]. MFT determines the magnetization and, with appropriate Maxwell relations, the magnetic contributions to specific heat and entropy. The second order

materials are compared to M1 in Fig. 5 for adiabatic temperature change and isothermal entropy change.

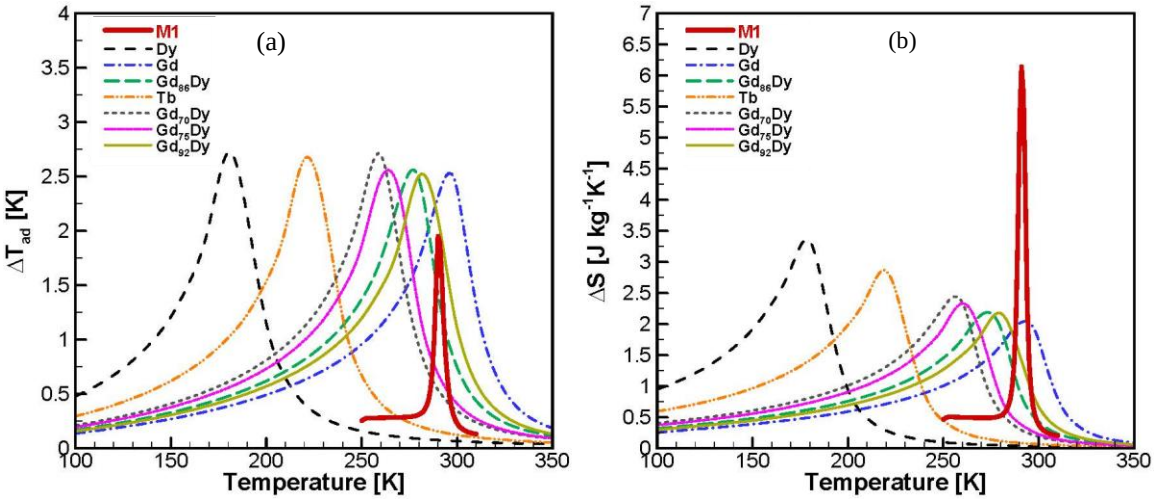


Fig. 30 a) Adiabatic temperature change and b) magnetic entropy change of second order materials and M1 of $MnFeP_{1-x}As_x$. The properties are presented for low field and high field of 0.35 and 1.1 tesla.

## 7.2 Metrics and Performance Results

The exergetic cooling power is calculated for each material sweeping operating temperatures and displaced volume so that a maximum power is found. This results in more than 6000 data points. Fig. 31 shows the correlations between material metrics and maximum power. Numerical values are also listed in Table 4.

Table 4 Material screening parameters and the maximum exergetic cooling power for each of the cases studied.

| Material | $\Delta S_{Max}$ [Jkg$^{-1}$K$^{-1}$] | $\Delta T_{Max}$ [K] | $\Delta S_{Max}.\Delta T_{Max}$ [Jkg$^{-1}$] | $\delta T_{FWHM}$ [K] | $RCP(S)$ [J kg$^{-1}$] | $RCP(T)$ [K$^2$] | $RCP_{Max}$ [J kg$^{-1}$] | $Ex_Q$ [W] |
|---|---|---|---|---|---|---|---|---|
| M1 | 6.1 | 2.0 | 12.20 | 5.7 | 29.28 | 11.15 | 73.42 | 0.87 |
| S1 | 3.5 | 1.4 | 4.90 | 5.6 | 17.5 | 8.07 | 59.30 | 0.49 |
| S2 | 3.5 | 1.4 | 4.90 | 8.9 | 26.6 | 12.74 | 67.07 | 0.72 |
| S3 | 2.1 | 1.0 | 2.10 | 9.2 | 17.22 | 9.30 | 55.77 | 0.37 |
| S4 | 2.2 | 1.1 | 2.42 | 13.2 | 25.52 | 13.86 | 60.72 | 0.51 |
| S5 | 2.5 | 1.2 | 3.00 | 13.2 | 28.5 | 15.18 | 64.25 | 0.66 |
| S6 | 8.1 | 2.2 | 17.82 | 5.2 | 35.64 | 11.68 | 81.19 | 1.15 |
| S7 | 9.3 | 2.3 | 21.39 | 5.4 | 40.92 | 12.50 | 86.84 | 1.21 |
| S8 | 7.6 | 2.1 | 15.96 | 9.5 | 54.72 | 20.01 | 100.25 | 1.63 |
| S9 | 4.9 | 1.5 | 7.35 | 5.6 | 21.07 | 8.10 | 68.48 | 0.39 |
| S10 | 7.5 | 1.7 | 12.75 | 5.4 | 28.5 | 8.95 | 81.90 | 0.68 |
| S11 | 5.9 | 1.5 | 8.85 | 9.2 | 46.02 | 14.01 | 79.78 | 0.80 |
| S12 | 7.1 | 2.5 | 17.75 | 5.9 | 39.05 | 14.57 | 80.34 | 1.13 |
| S13 | 10.5 | 2.9 | 30.45 | 5.7 | 56.7 | 16.71 | 98.13 | 1.56 |
| S14 | 9.1 | 2.6 | 23.66 | 10.1 | 80.99 | 26.32 | 122.14 | 2.22 |
| S15 | 7.6 | 2.1 | 15.96 | 9.5 | 72.2 | 19.97 | 101.66 | 1.52 |
| Dy | 3.34 | 2.76 | 9.22 | 41.40 | 170.23 | 114.46 | 260.51 | 6.26 |
| Gd | 2.07 | 2.56 | 5.30 | 43.67 | 112.93 | 147.42 | 189.27 | 3.93 |
| Gd86Dy | 2.24 | 2.61 | 5.85 | 43.64 | 121.92 | 113.99 | 201.92 | 4.30 |
| Tb | 2.86 | 2.74 | 7.84 | 42.98 | 152.89 | 117.91 | 242.86 | 5.62 |
| Gd70Dy | 2.45 | 2.71 | 6.64 | 44.24 | 135.24 | 119.81 | 220.27 | 4.87 |
| Gd75Dy | 2.36 | 2.65 | 6.25 | 43.70 | 128.59 | 115.84 | 211.09 | 4.61 |
| Gd92Dy | 2.18 | 2.59 | 5.65 | 43.58 | 118.59 | 112.97 | 196.97 | 4.18 |

The results show that *RCP*(*s*) provides a better correlation to maximum power than *RCP*(*T*). In the case of the latter, *RCP*(*T*) is unable to distinguish between the potential of materials with similar ordering – FOMs and SOMs tend to be grouped together (Fig. 31 (a) and (b)) with low sensitivity amongst materials with similar phase transition behaviour. $\Delta T_{\mathrm{Max}}$ and $\Delta S_{\mathrm{Max}}$ show poor correlation with maximum performance (Fig. 31 (c) and (d)). $\Delta S_{\mathrm{Max}}.\Delta T_{\mathrm{Max}}$ also results in FOMs and SOMs being grouped together (Fig. 31 (e)) showing a trend which is similar to $\Delta S_{\mathrm{Max}}$ . $RCP_{\mathrm{Max}}$ (Fig. 31 f) shows a strong linear correlation with maximum exergetic cooling power. This suggests that $RCP_{\mathrm{Max}}$ can be an effective metric to screen material for AMR application.

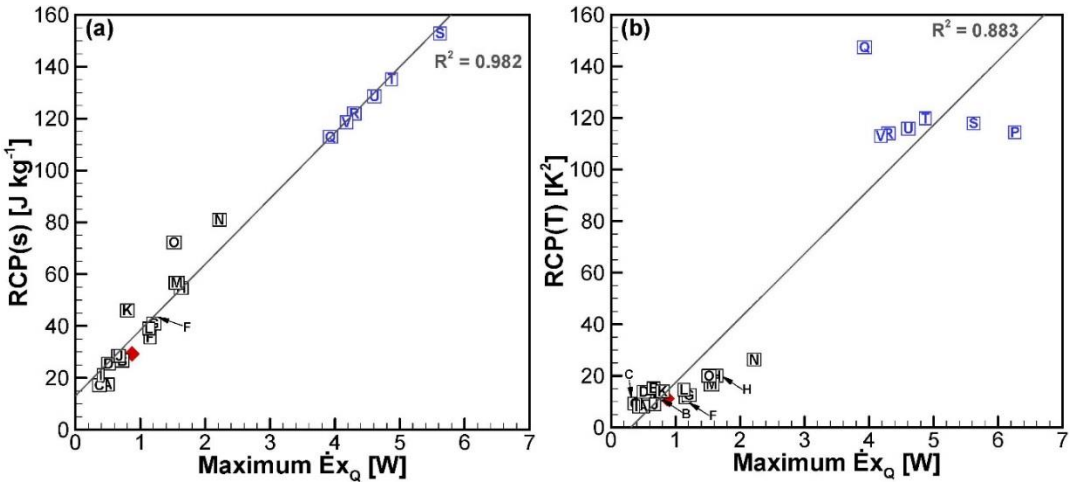

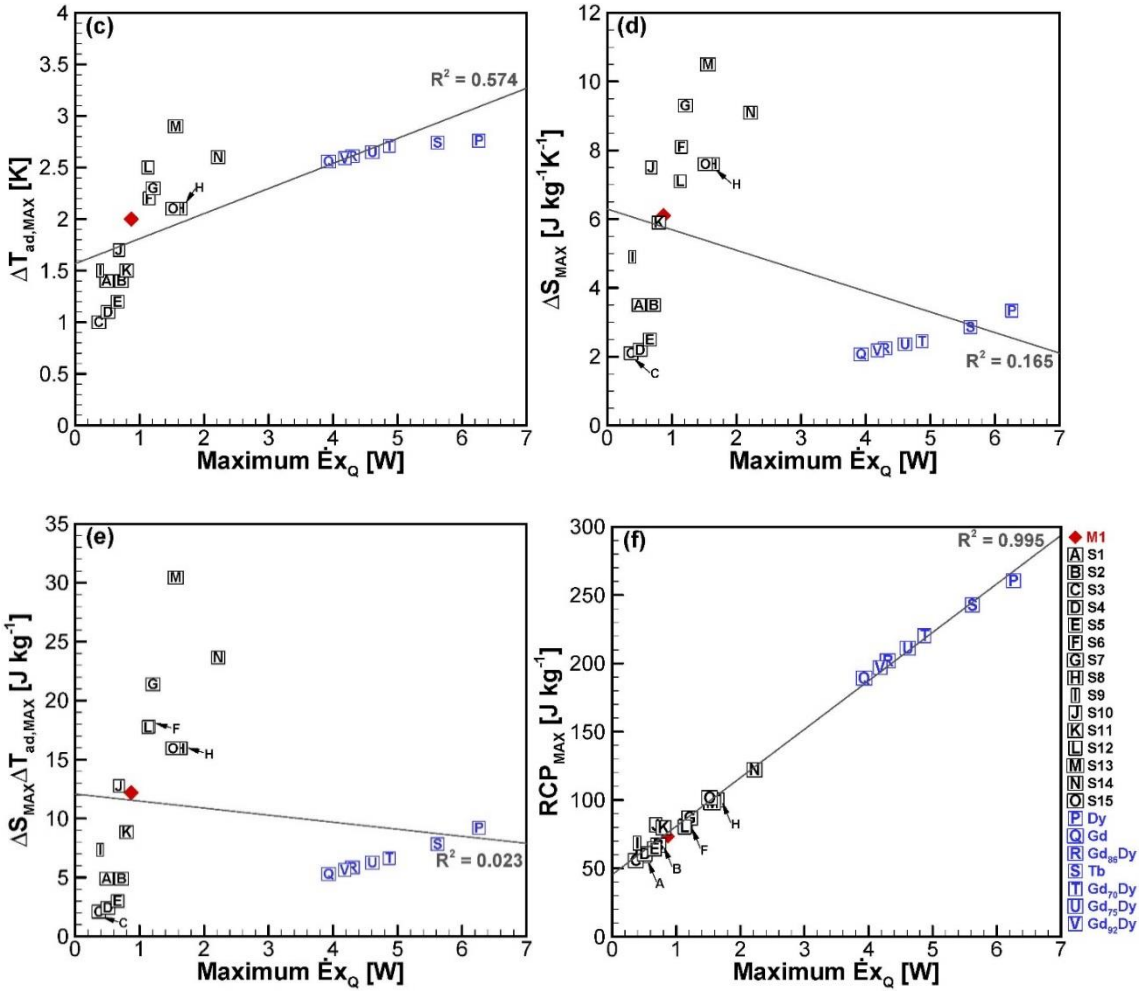


Fig. 31 Maximum exergetic cooling power of the studied material versus screening metrics, a) *RCP(S), b) RCP(T), c)* $\Delta T_{Max}$ , d) $\Delta S_{Max}$ and e) $\Delta S_{Max}.\Delta T_{Max}$ f) $RCP_{Max}$. In each figure a linear trend line is added and the R squared value which is a measure of deviation from the linear behavior is calculated and displayed. Blue markers indicate SOM cases.

## 7.3 Discussion

As shown in Fig. 31 (f), there is a strong linear correlation between maximum exergetic cooling power and $RCP_{Max}$. From a design point of view, the next step after selecting material for an AMR is identifying the operating conditions that correspond to the optimum performance. The operating conditions which exhibit the maximum

exergetic cooling power are identified in Table 5 for a subset of materials. $T$* are temperatures on the cold and hot side of the AMR when maximum exergetic power is produced. As a reference, the temperatures where the peak entropy change and adiabatic temperature change are found are listed. In general, the optimum temperature span results in both maximum adiabatic temperature change and entropy change residing somewhere inside the AMR. In actual applications, the operating conditions of the AMR might not be exactly the same as the designed operating conditions. As a result, maximum exergetic cooling power might not be achievable. Moreover, it may be difficult to manufacture material with the designed Curie temperature; thus, it is important to investigate the sensitivity of maximum performance to the operating temperatures [86]. The deviation of reservoir temperature from the optimum, $\delta T$ , is,

$$\delta T_{cold} = T_{cold} - T_{cold}^{*} \tag{51}$$

$$\delta Ex_Q\% = \frac{Ex_Q - Ex_Q^{*}}{Ex_Q^{*}} \times 100 \tag{52}$$

Here, again, the superscript * refers to the operating condition where maximum exergetic cooling power is identified. Fig. 32 shows the sensitivity of performance to deviations of the cold side temperature from the peak operating condition. The results indicate that for the FOM cases studied, performance is highly sensitive to the cold side temperature. With a two degree change in the cold side temperature, the exergetic cooling power can drop up to 60 percent for some cases. However, such sensitivity is not observed for SOM

cases. The change in performance is less than 5 percent with a change in cold side temperature of 4 degrees.

Table 5 Points of optimum operation for cases studied. $T^*_{cold}$ and $T^*_{hot}$ represents the cold side and hot side temperatures of the AMR corresponding to the maximum exergetic cooling power. $T_{\Delta S,\mathrm{Max}}$ and $T_{\Delta T,\mathrm{Max}}$ show the temperature where maximum magnetic entropy change and maximum adiabatic temperature change for the material are observed. The displaced volume corresponding to the optimum performance, in all cases were between 15-22.5 $cm^3$.

| Material | $T^*_{cold}$ [K] | $T^*_{hot}$ [K] | $T_{\Delta S,\mathrm{Max}}$ [K] | $T_{\Delta T,\mathrm{Max}}$ [K] | $\delta T_{FWHM}$ [K] | $\frac{span}{\delta_{FWHM}}$ |
|---|---|---|---|---|---|---|
| Dy | 161 | 187 | 179 | 182 | 41.40 | 0.63 |
| Gd | 273 | 302 | 294 | 296 | 43.67 | 0.66 |
| Gd86Dy | 253 | 280 | 274 | 277 | 43.64 | 0.62 |
| Tb | 202 | 227 | 220 | 223 | 42.98 | 0.58 |
| Gd70Dy | 236 | 263 | 257 | 259 | 44.24 | 0.61 |
| Gd75Dy | 241 | 268 | 262 | 265 | 43.7 | 0.62 |
| Gd92Dy | 260 | 286 | 281 | 283 | 43.58 | 0.60 |
| M1 | 285 | 290 | 291 | 290 | 5.7 | 0.88 |
| S1 | 285 | 290 | 291 | 291 | 5.6 | 0.89 |
| S2 | 285 | 292 | 292 | 291 | 8.9 | 0.79 |
| S3 | 285 | 292 | 292 | 291 | 9.2 | 0.76 |
| S4 | 285 | 290 | 293 | 292 | 13.2 | 0.38 |
| S5 | 285 | 290 | 293 | 292 | 13.2 | 0.38 |
| S6 | 285 | 292 | 291 | 290 | 5.2 | 1.35 |
| S7 | 285 | 292 | 291 | 290 | 5.4 | 1.30 |
| S8 | 287 | 293 | 292 | 291 | 9.5 | 0.63 |
| S9 | 289 | 292 | 292 | 292 | 5.6 | 0.54 |
| S10 | 287 | 292 | 292 | 292 | 5.4 | 0.93 |
| S11 | 289 | 292 | 293 | 292 | 9.2 | 0.33 |
| S12 | 281 | 290 | 290 | 289 | 5.9 | 1.53 |
| S13 | 283 | 290 | 290 | 289 | 5.7 | 1.23 |
| S14 | 283 | 288 | 291 | 289 | 10.1 | 0.50 |
| S15 | 285 | 290 | 290 | 289 | 9.5 | 0.53 |

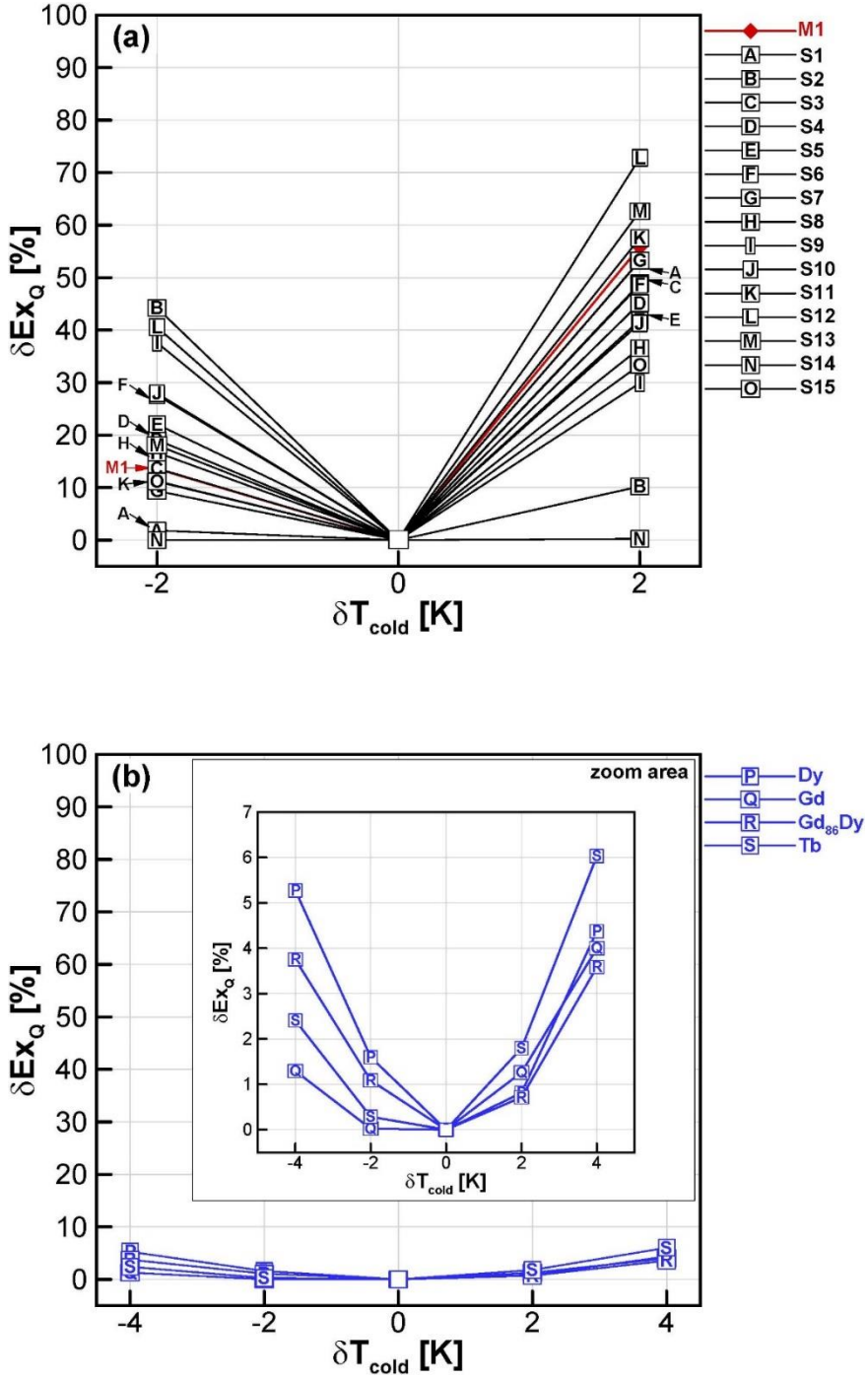


Fig. 32 Percent drop in exergetic cooling power as a function of $\delta T_{Cold}$ for a) FOM cases and b) SOM cases.

Fig. 33 shows the sensitivity of performance to deviations of the hot side temperature from the optimum $T^*$. FOM cases show high sensitivity to the hot side temperature and as

the hot side temperature changes by 2 degrees, the performance drops up to 80% for some of the cases. The SOM cases also indicate some sensitivity to the hot side temperature, however, their performance drops by less than 20% for a 2 degree change in the hot side temperature.

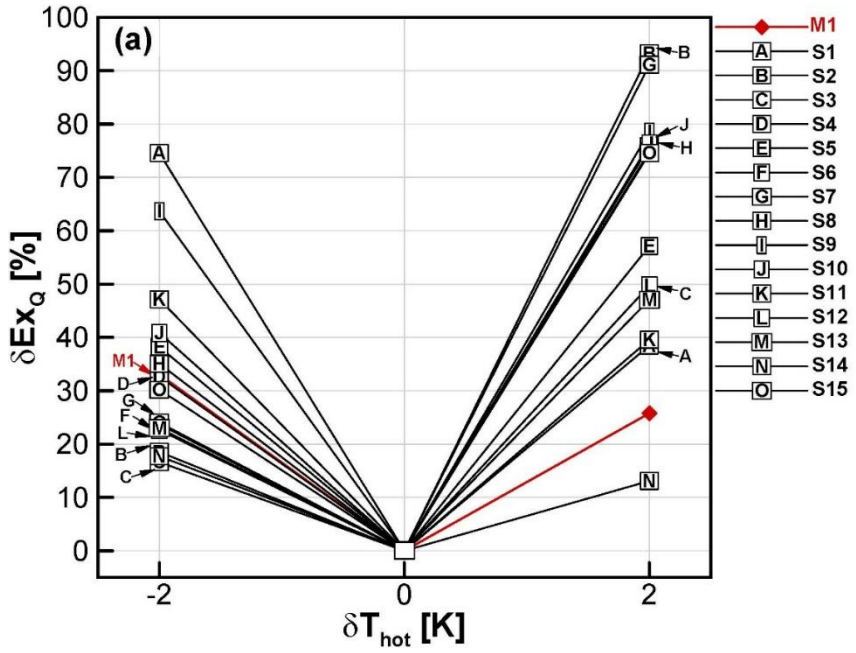

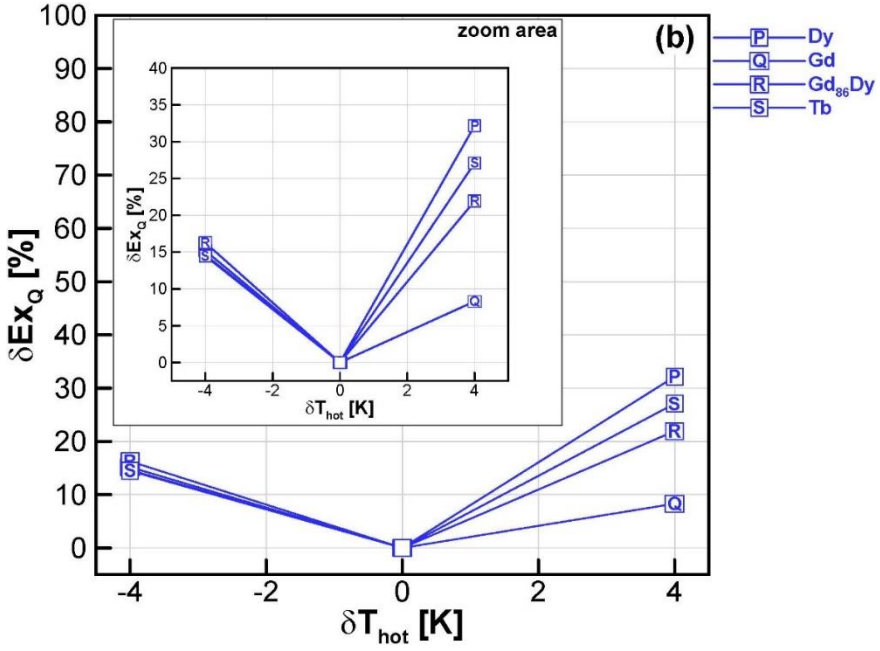


Fig. 33 Percent drop in exergetic cooling power as a function of $\delta T_{hot}$ for a) FOM cases and b) SOM cases.

Comparing Fig. 32 and Fig. 33 for SOMs, it can be concluded that the sensitivity of maximum exergetic power to deviations in hot side temperature are more significant than similar deviations in the cold side temperature. A 4 K deviation in $T_{hot}$ results in a decrease in power of up to 30% whereas a similar deviation on the cold side results in only a 5% reduction.

For FOM cases, the behaviour is different. The sensitivity of performance to both hot side and cold side temperatures are higher than SOM cases. However, some materials show higher sensitivity to the changes in cold side temperature (such as M1) and others show higher sensitivity to the changes in cold side temperatures (such as S2). With performance drops which can be up to 80% for a 2 K deviation from optimum operating

conditions, the need to minimize the difference between the operating temperatures and the design temperatures with FOMs is evident.

## 7.4 Summary

Selecting proper material for an AMR application, is a crucial step in designing efficient magnetic heat pumps. Using numerical and experimental measurements is one way of identifying appropriate material for MR applications. However, these methods can be expensive and time consuming. In this chapter the developed numerical model is used to assess the predictive ability of a set of material metrics. For this purpose, eight cases of known material and 15 cases of synthetic material are numerically analyzed and the predictive capability of the material metrics were compared against the simulation results for the maximum exergetic cooling power of each material. It was shown that among the studied metrics, $RCP_{\mathrm{Max}}$ shows a linear correlation with the maximum exergetic cooling power of the material. Such behaviour was not observed for other screening metrics. The sensitivity of the maximum exergetic cooling power to the absorption and rejection temperatures were also investigated. These results can be considered as helpful guidelines in selecting proper material and operating conditions for devices. In the next chapter, some of the key characteristics of the performance of an FOM in an AMR will be discussed. Cooling power curves will be closely studied and the stability of points of equilibrium will be analyzed.

# Chapter 8 Performance and Stability of Equilibrium

The current rate of growth in discovery of FOMs, and the challenges inherent with these materials call, for a better understanding of how FOMs perform in an AMR. One of the challenges with FOMs is hysteresis. General effects of hysteresis on refrigeration performance for a model GMCE have been reported [87,88]. In addition to the hysteresis, the narrow temperature window for adiabatic temperature change and magnetic entropy change is another challenge. In this chapter the performance of FOMs in an AMR is studied in detail and the impacts of properties and multiple points of equilibrium is discussed.

## 8.1 Material Properties

Amongst the families of FOMs reported in recent years, the Fe2P-based system has shown potential for room temperature magnetic heat pump applications. In Section 3.3.2 two classes of material from this family ($MnFeP_{1-x}As_x$ and $MnFeP_{1-x}Si_x$) were briefly introduced. In this chapter, samples from the $MnFeP_{1-x}Si_x$ family are experimentally and numerically studied.

Fig. 34 presents adiabatic temperature change and specific heat of a $MnFeP_{1-x}Si_x$ sample. The properties are experimentally measured using cyclic $T_{ad}$ and DSC with heating and cooling protocols.

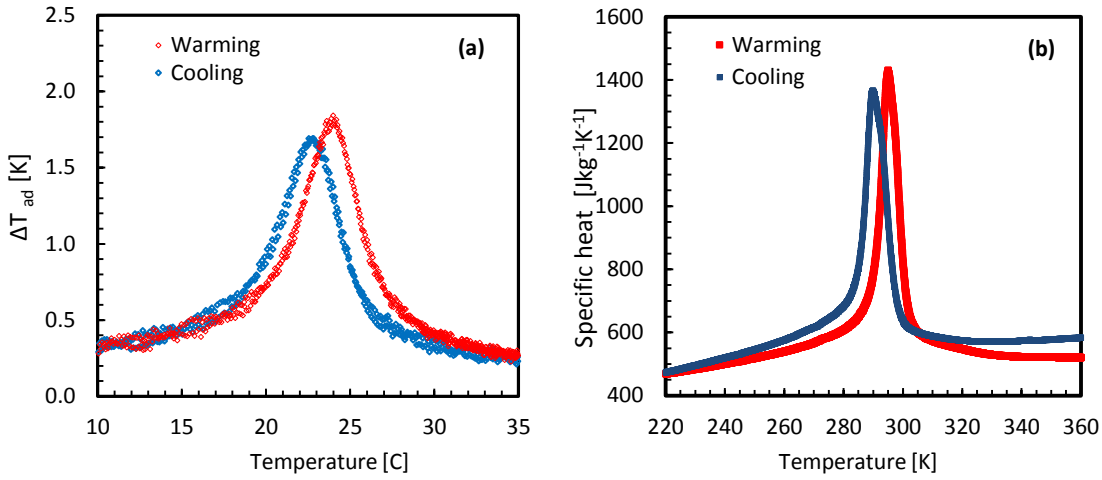


Fig. 34 Material properties measured for a sample $MnFeP_{1-x}Si_x$. a) Adiabatic temperature change for a magnetic field change of 0-1.1 T, b) Specific heat for heating (warming) and cooling measurements at 0 T.

For numerical simulations, material properties are modeled using the same approach described in Chapter 7 whereby specific heat is approximated with a Lorentzian curve, and the transition shift due to field is determined by the difference in temperature between the peak specific heats. Integration of specific heat provides total entropy curves which are interpolated for $\Delta T$ and $\Delta s_m$. Fig. 35 shows modeled properties for $MnFeP_{1-x}Si_x$ with a thermal hysteresis of 1.7 K and a zero-field warming transition of 288 K. These properties are evaluated using magnetic field values of 0.35 and 1.1 T, respectively, representing the flow-averaged fields in the PM II device [32].

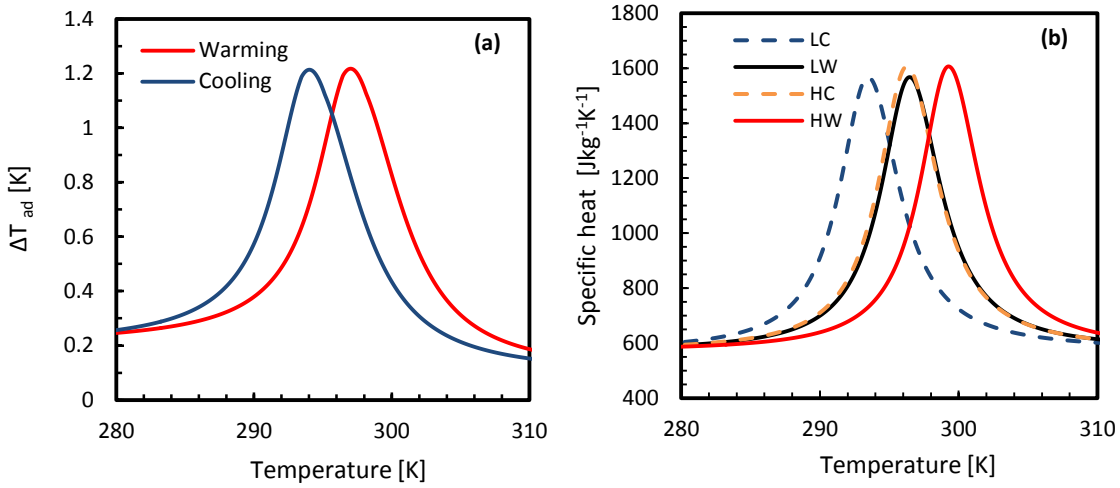


Fig. 35 Simulated a) adiabatic temperature change, b) specific heat of the $MnFeP_{1-x}Si_x$ samples for low field of 0.35 and high field of 1.13 T [32,66]. In the figures, *L* and *H* represent low field and high field states. *C* and *W* represent cooling and warming protocols. (i.e. *LC* represents measurements conducted at low field following the cooling protocol)

## 8.2 Methods

The numerical model described in [32,37] is employed to determine temperature as a function of space and time $T(x, t)$ for the solid matrix and fluid. To accurately model temperature sensitive material properties such as magnetocaloric effect and specific heat, care should be taken when selecting the numerical resolution of a simulation. In this study, a uniform mesh is selected and a detailed grid study is performed to ensure the independence of simulation results from the number of elements. Absolute and relative tolerance of the solver is set to 1e-6. The convergence criterion of the model is set to 1e-5, specifying that the maximum change between the temperature profiles at any time one cycle apart should not exceed 1e-5 K.

Two performance parameters are considered: cooling power and temperature span. In the experiments, the net cooling power is set based on the thermal load applied by a

heater in the cold heat exchanger [31,66]. In the numerical simulations, gross cooling power is the rate of energy transfer across the cold boundary determined from the cycle averaged enthalpy flow at the cold side. The net cooling power is determined by subtracting parasitic heat leaks from the gross cooling power. The temperature span is the temperature difference between the hot side and cold side of the regenerator; experimentally, this is the cycle-averaged fluid temperature. Both cooling capacity and temperature span are dependent on the operating conditions (flow rate, frequency ($f$) and rejection temperature ($T_h$)) and thermal losses) [39].

Table 6 presents the properties and operating conditions of the regenerator used for simulations. These operating conditions are used to study the performance of FOM samples ($MnFeP_{1-x}Si_x$) and compare results to a benchmark material (Gd). It should be noted that for FOM cases, because of the abrupt changes in the magnetocaloric properties, smaller increments for the hot side and cold side temperatures are selected ($\delta$ = 1 K) for consecutive data points. As will be shown, with FOM materials, data points that are greater than 2 K apart may be too coarse to capture some details. Details of the numerical model including the heat transfer fluid are described in Chapter 5 and [32].

Table 6 Regenerator properties and operating parameters used for simulation of $MnFeP_{1-x}Si_x$ and Gd samples.

| Parameter | Value | Units |
|---|---|---|
| Regenerator diameter | 1.59 | cm |
| Regenerator length | 5.6 | cm |
| Particle size (spherical) | 360 | μm |
| Mass of MCM | 50.0 | g |
| Porosity | 0.39 | - |
| Frequency, $f$ | 0.9 | Hz |
| Displaced volume, $V_d$ | 5.0 | $cm^3$ |
| Hot side temperature (FOM) | 288-314 ($\delta = 1$) | K |
| Cold side temperature (FOM) | 267-313 ($\delta = 1$) | K |
| Hot side temperature (Gd) | 288-306 ($\delta = 2$) | K |
| Cold side temperature (Gd) | 267-305 ($\delta = 1$) | K |

## 8.3 Cooling Power

Numerical predictions of cooling power as a function of the cold side temperature, $T_C$, are presented in Fig. 36. The data in (a) show results for Gd, while (b) and (c) show data for $MnFeP_{1-x}Si_x$ where each line represents a different fixed rejection temperature, $T_h$. The properties of $MnFeP_{1-x}Si_x$ based on a cooling measurement (Fig. 35) are used for simulations. Fig. 36 (a) and (b) show gross cooling power which is when external losses, $Q_p$, are neglected. Fig. 36 (c) shows net cooling power for the $MnFeP_{1-x}Si_x$ where parasitic heat leaks are included.

Over the range of rejection temperatures considered, the gross cooling power for Gd (Fig. 36 (a)) increases monotonically with the cold side temperature; hence, for a fixed hot side temperature and operating conditions, reducing temperature span results in higher cooling power. However, this behaviour is not observed for $MnFeP_{1-x}Si_x$ cases (Fig. 36 (b)). For example, for a fixed hot side temperature of 300 K, as the cold side

temperature increases the cooling power increases up to a peak (at $T_c$ = 290 K) before decreasing to a minimum (at $T_c$ = 295 K) and then increasing again. Similar behaviour is seen in Fig. 35 (c) when heat leaks are considered and net cooling power is plotted.

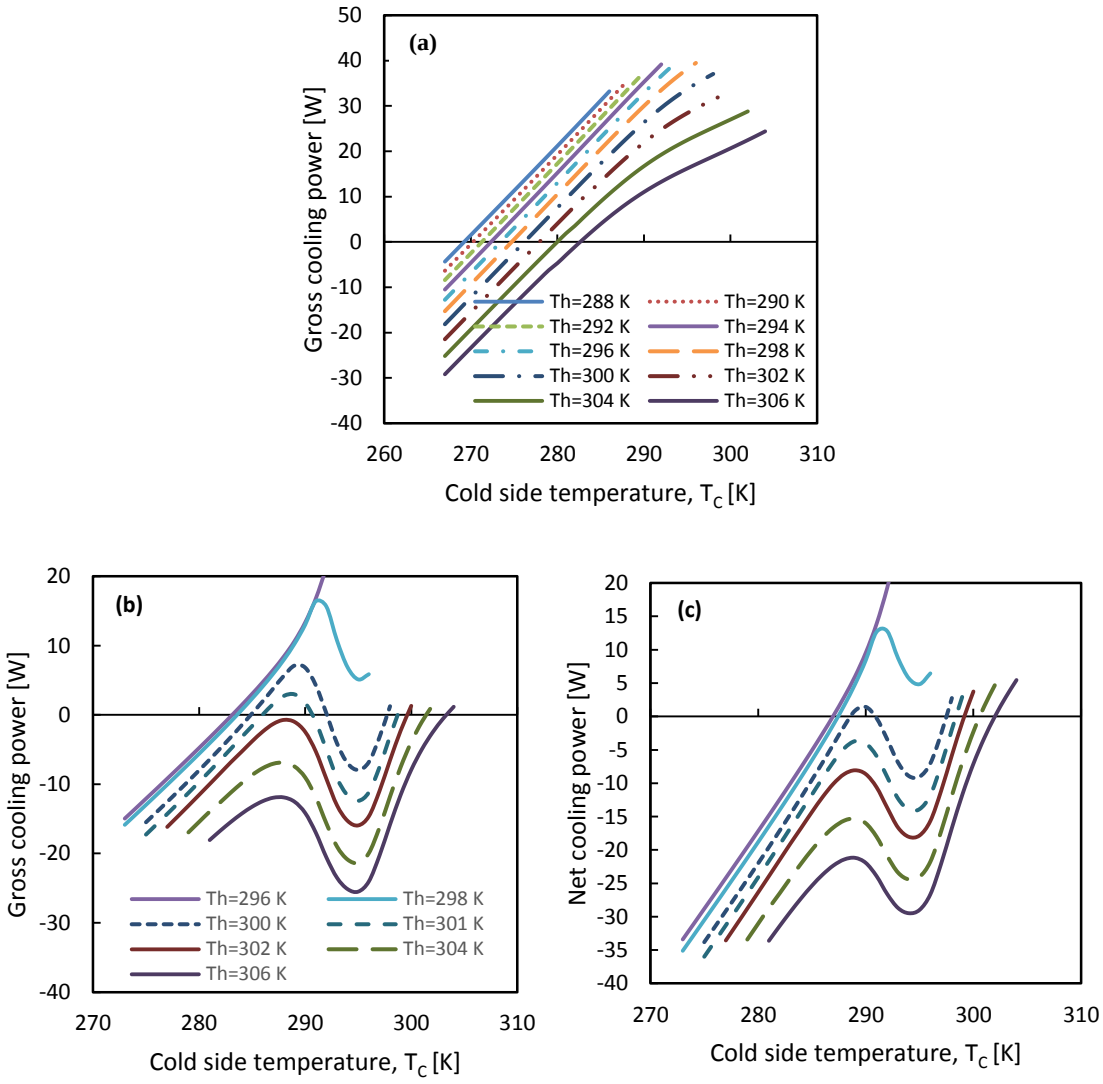


Fig. 36 Cooling power as a function of cold side temperature for a) Gd and b) $MnFeP_{1-x}Si_x$ sample without configuration losses (heat leaks.) c) $MnFeP_{1-x}Si_x$ material with configuration losses included in the model.

For Gd, the cooling power curves are single-valued functions; for a fixed $T_h$ there is only one cold-side temperature corresponding to any given cooling power. This suggests

that for specified operating conditions (fixed applied load), only one point of equilibrium (PE) can be obtained. Point of equilibrium (PE) for a fixed heat rejection temperature refers to the cold side temperature where the system is in thermal equilibrium. For example, for a fixed hot side temperature of $T_h$ = 300 K and applied load of 5 W, the resulting cold side temperature is ~278 K. This cold side temperature is called the point of equilibrium for the given operating conditions.

The cooling power curves are not always single-valued functions for $MnFeP_{1-x}Si_x$. For example, for a fixed hot side temperature of $T_h$ = 300 K and a gross cooling power of 0 W, the cooling power is a multivalued function; there are multiple points of equilibrium (MPE) (three PEs at $T_c$ = 286, 292, 298 K.) Similar results are seen when considering *Qc* = 5 W and 10 W which have MPEs.

One of the more interesting points of equilibrium is the point that corresponds to zero cooling power. This PE gives the maximum temperature span a system can develop. In this study a point of equilibrium corresponding to zero cooling is called a *zero-load point of equilibrium*.

Impacts of configuration losses are shown in Fig. 36 (c). Heat leaks between the hot reservoir and cold reservoir, and the effects of imperfect thermal isolation between the cold end and environment are considered. These losses are inherent to the performance of most AMR devices. Comparing Fig. 36 (b) and (c), the range of rejection temperatures where zero load MPE are observed decreases significantly with configuration losses

included. In the case with losses, only at $T_h$ = 300 K zero load MPEs are observed. For all the remaining $T_h$, values a single zero load point of equilibrium is found.

## 8.4 Stable and Unstable Equilibrium

The question we now consider is which points of equilibrium are stable. As will be shown, the stability depends on the slope of the cooling power curve with respect to temperature at the PE. To understand under what conditions a PE is stable, we need to consider how an AMR performs dynamically in terms of temperature span versus cooling power. A lumped model of the cold side of the AMR (cold heat exchanger) relates the temporal response of the cold side to changes in load, $Q_a$, leaks, $Q_p$, and gross cooling power, $Q_{AMR}$. The sum of these heat transfers is defined as the *thermal balance*, $\Delta Q$.

$$\rho c V \frac{dT_c}{dt} = \underbrace{Q_a + Q_p - Q_{AMR}}_{\equiv \Delta Q} \tag{53}$$

So, a PE occurs when,

$$\Delta Q = 0$$

And a *zero-load PE* is specifically when $\Delta Q = 0$ and $Q_a = 0$.

In our AMR experiments, the system starts with a fixed heat rejection temperature (hot side temperature). If the operating condition results in a negative thermal balance ($\Delta Q < 0$), the cold side temperature will decrease as the system operates. As long as the thermal balance is negative, the temperature span will continue to develop. When the gross cooling power balances the applied load and parasitic heat leaks $\Delta Q = 0$ and a PE is found. The opposite situation may arise during an experiment whereby the thermal

balance is positive ($\Delta Q > 0$) meaning that the system is not able to reduce the cold side temperature. In this case, leaks from the ambient and the applied load will increase the cold side temperature. As the system operates, the cold side temperature increases until the thermal balance approaches zero. At this point the cold side temperature does not change; hence, a PE is found.

When the system is operating at a PE, small perturbations can initiate a thermal imbalance on the system. In the case of a temporary increase in the thermal balance ($\Delta Q > 0$), the cold side temperature will begin to increase. If the gross cooling power of the AMR increases monotonically with the cold reservoir temperature (as with Gd), the thermal balance can become negative which will then reduce the temperature of the cold side of the AMR and move it back to the stable position ($\Delta Q = 0$). Similarly, a temporary decrease in the cold side temperature reduces the gross cooling power, causing the thermal balance to be positive, causing the cold side temperature of the AMR to increase back to the stable position. This behaviour is associated with a stable point of equilibrium and is a result of the positive slope of gross cooling power with respect to cold temperature.

We now discuss the multiple points of equilibrium which arise with the FOM. Unlike Gd, the gross cooling power of the $MnFeP_{1-x}Si_x$ material is not monotonically increasing; there are states where cooling power decreases as the cold side temperature increases. To explain stability, we will focus on a zero-load PE situation as shown in Fig. 37. Based on the previous discussion, the stability of a PE depends on the slope of the cooling power curve with respect to temperature at the PE.

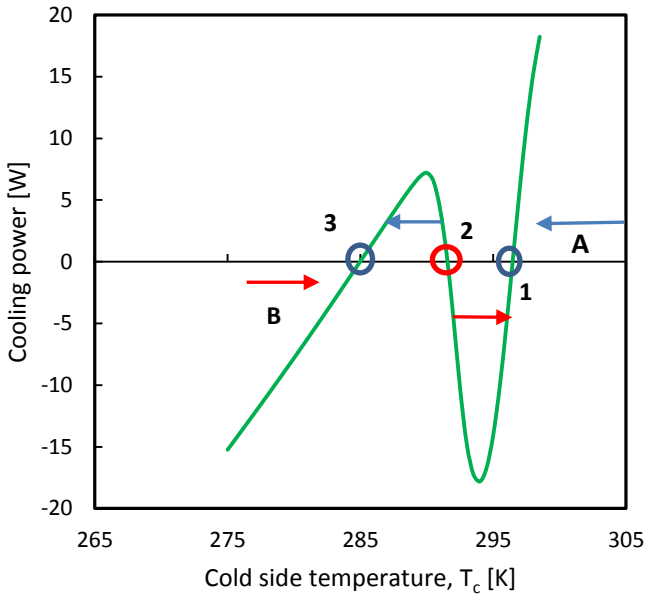


Fig. 37 Cooling power curve as a function of cold side temperature. The red circle indicates an unstable zero load PE and the blue circles show stable zero load PEs. The arrows show the direction cooling power pushes the cold side if small perturbation is introduced. The blue arrows indicate positive cooling power which tends to increase the temperature span and the red arrows indicate negative cooling power which results in decrease of temperature span.

Three zero-load PEs are identified in Fig. 37. Of these points, only 1 and 3 are stable with respect to a small perturbation in $T_c$. In the case of point 2, the thermal balance is zero; however, a perturbation in $T_c$ will cause the system to migrate to either point 1 or point 3. Hence, point 2 is an unstable PE.

After understanding and identifying the stable and unstable PEs, the main question would be which point of equilibrium is the one that we measure experimentally? The answer depends on the previous thermal state of the system. If the load is zero watts and the initial cold side temperature of the device is in area A of Fig. 37, then PE 1 is the equilibrium temperature. If the initial temperature of the cold side is in region B, then PE 3 will be the point where the cold side temperature stabilizes. Thus, if the device is in

cooling mode (the thermal balance is negative) and the cold side temperature is near the hot side temperature, a smaller temperature span will be achieved as compared to when a positive thermal balance exists (heating mode) and the cold side temperature is below PE 2 such that a larger temperature span is achieved.

The existence of MPEs can lead to problems when designing regenerators for an AMR system. During operation, an AMR might produce a smaller temperature span than expected. In multilayered regenerators one of the materials may be limited in span due to an unfavorable thermal equilibrium and thereby limit the performance of the entire cascade. Some consideration can be taken to avoid this. As shown in Fig 36 (c), these problems occur when the heat rejection temperature exceeds a certain temperature. In the cases of $T_h$ = 298, the cooling power curve is unstable in some conditions; however, the unstable region is when there is a net positive cooling power. Therefore, if the regenerator (each layer) is designed to operate at a sufficiently low rejection temperature, MPEs may be avoided. However, further research should be done experimentally and numerically on the methods of avoiding PEs in cascade design before conclusive recommendations can be provided on this matter.

## 8.5 Experimental Observation

A series of experiments are performed on single material AMRs composed of $MnFeP_{1-x}Si_x$ and $MnFeP_{1-x}As_x$ material. The AMRs are tested in PMI [69] and PM II [66] devices and the performance is measured using heating and cooling procedures. For each regenerator, the maximum temperature span as a function of heat rejection temperature is

measured. Fig. 38 presents the experimental temperature spans as a function of the rejection temperature for different thermal loads for (a) $MnFeP_{1-x}Si_x$ and, (b) $MnFeP_{1-x}As_x$ compounds. The experimental results show that at low $T_h$ values, the cooling and heating curves have a similar temperature span. As $T_h$ increases a maximum span is obtained for a given applied load and, after this peak point, the cooling and heating curves show significantly different spans.

Von Moos et al. [89] performed similar experiments where they studied MnFe(P,As) in an AMR. They reported that the curve of temperature span as a function of hot side temperature for the heating procedure shifts to the right of the cooling curve by 1.1 K. This behaviour was attributed to thermal hysteresis of the material which was also ~1.1 K.

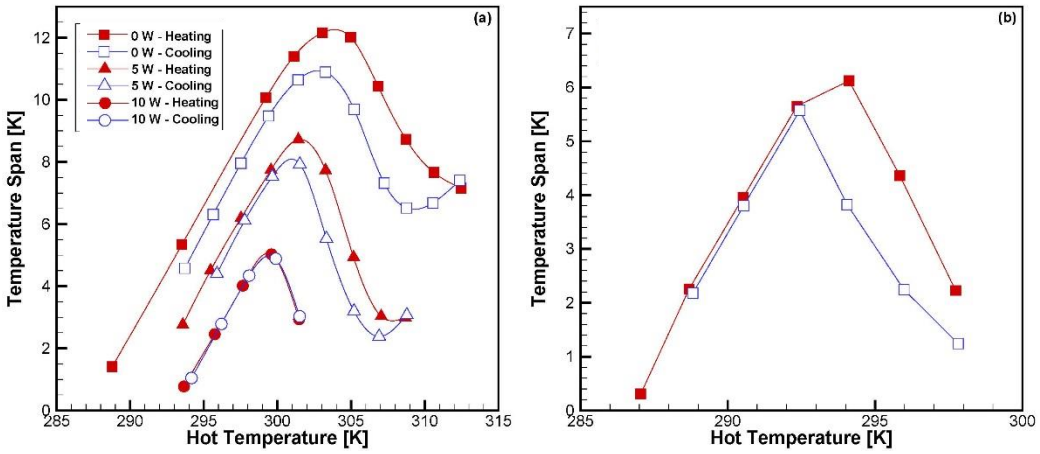


Fig. 38 Sample heating and cooling measurements obtained for (a) $MnFeP_{1-x}Si_x$ ; (b) $MnFeP_{1-x}As_x$. Figure 38 (a) is plotted for the operating conditions presented in Table 6. Figure 38 (b) is obtained with a frequency of 0.7 Hz, applied load of 5W, displaced volume of 6.96 $cm^3$, and material mass of 143g.

Based on the MPE phenomenon predicted for FOMs, the experimental results shown in Fig. 38 can be interpreted in a different light. From Fig. 38 (a), MPEs exist close to the

peak operating temperature and, as the load increases, they tend to disappear (10 W). The results in Fig. 35 (c) show that the MPEs tend to approach each other as the losses and loads increase. Another important characteristic of the PEs seen in Fig. 35 is that a larger temperature span corresponds to heating mode while a smaller temperature span is associated with cooling mode. Similar behavior is observed in Fig. 38 where heating curves correspond to a larger temperature span than the cooling curves. Such similarities in behavior suggest that MPE phenomena are impacting FOM behaviour seen in AMR cycles; however, MPE results alone do not fully explain the measured data. In the following section, MPE will be considered with thermal hysteresis.

## 8.6 Numerical Results

The performance of a $MnFeP_{1-x}Si_x$ AMR is simulated while considering both the impacts of thermal hysteresis and MPEs. When simulating a heating experiment, material properties ($c_{p,}$ $\Delta T$ and $\Delta s$) corresponding to a heating measurement procedure are used. Likewise, for a cooling experiment, the corresponding material properties are used. When constructing a heating curve for temperature span as a function of rejection temperature, only the PEs associated with the largest equilibrium temperature spans are included. When constructing a cooling curve, only the PEs with the smallest span are included. Fig. 39 shows the performance of the $MnFeP_{1-x}Si_x$ sample represented by properties shown in Fig. 34 for applied loads of zero and 5 W. Configuration losses are included in the simulations to compare with the experimental results. The operating parameters used in this simulation are presented in Table 6.

Comparing numerical model with experimental measurements (presented in Fig. 38) it is seen that numerical model is able to follow the trend of performance well. However, there are some differences between experimental measurements and the numerical simulations. In the experimental results, the heating and cooling curves overlap at rejection temperatures less than the peak location, while in the numerical results a shift is observed, similar to the experimental observations reported by [89]. These differences can be explained based on the experimental heating and cooling procedures. In [89] when making heating and cooling measurements, for every point the system is heated or cooled down before starting every single experimental point; thereby, resetting the material state. However, the heating and cooling experiments used here follow a continuous experimental protocol, whereby a small decrease (cooling protocol) or increase (heating protocol) is made to $T_h$ after steady-state is reached for the previous rejection temperature.

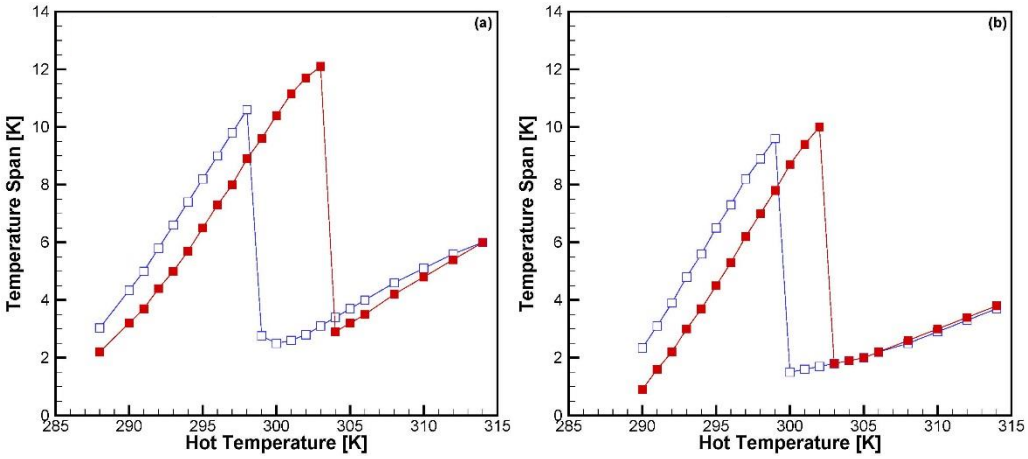


Fig. 39 Temperature span as a function of hot side temperature for MnFe(P, Si) material tested with considering the configuration losses. a) for 0 W of applied load and b) for 5W of applied load. The red markers represent the heating curve and the blue markers represent the cooling curves

## 8.7 Summary

First order transition material (FOM) usually exhibit magnetocaloric effects in a narrow temperature range which limits their applicability in an AMR. Magnetocaloric effect in FOMs are dependent on field and temperature history of the material. In this chapter a detailed numerical model along with experimental measurements were used to study the behavior of $MnFeP_{1-x}Si_x$ samples in an AMR. For certain operating conditions, it was observed that multiple points of equilibrium (PE) exist for a fixed heat rejection temperature. Stable and unstable PEs were identified and behavior of these points were discussed. The impacts of heat loads, operating conditions and configuration losses on the number of PEs were discussed and it was shown that the existence of MPEs can affect the performance of an AMR significantly. Thermal hysteresis along with MPEs were considered as the main factors that contribute to the temperature history dependent performance behavior of FOMs when used in an AMR.

# Chapter 9 Conclusions

The work reported in this thesis presents a numerical and experimental investigation of the performance of AMR systems using first order and second order transition materials. The main goal is to further our understanding of behaviour of magnetocaloric material in AMR system and investigate the impacts of different design and operating parameters on the performance of AMR systems.

## 9.1 Numerical Model and Performance Analysis

A transient one dimensional numerical model is developed to study the performance of AMR systems where external losses due to imperfect thermal isolation are considered. The model is validated against experimental results using gadolinium spheres in a permanent magnet apparatus. A sinusoidal mesh generation technique is utilized and shown to provide good accuracy with fewer nodes than a uniform mesh. In the cases considered, this technique reduced the number of elements needed for an effective simulation up to three times compared to a uniform mesh. It is shown that a step change model for applied field results in accurate predictions where the low and high field values are determined using flow weighted average fields for each blow period.

A simple resistance network model is used to simulate external losses. Through experiments, loss coefficient factors are estimated to determine conductances linking the cold side of the AMR to the environment and the hot side. As temperature span increases, the gross cooling power of the AMRs tends to decrease while the external leaks grow.

These effects lead to lower net cooling power and efficiencies. The thermal effectiveness of the AMR is linked to capacity rate of the fluid, and increases in capacity rate reduce the maximum efficiency that can be achieved. At lower capacity rates, the efficiency is more sensitive to changes in cooling power. Calculating the maximum temperature span of a typical system without considering the configuration losses might be misleading. These findings were reported in *Applied Thermal Engineering* journal [32].

## 9.2 Material Selection

Performance of more than 23 cases of first order and second order material are investigated using the developed numerical model. MFT was used to model magnetocaloric properties for SOM cases. For synthetic FOM cases, specific heat is modeled using a Lorentzian curve and integrated to determine isofield entropy curves. Two approaches used for creating material properties ensure thermodynamic consistency in the key magnetocaloric data. For each material, a wide range of operating conditions is studied and the point of maximum exergetic cooling power is identified. The correlation of the maximum exergetic cooling power with conventional material screening metrics is analyzed. The results show that $RCP_{\mathrm{Max}}$ has a linear correlation with the maximum exergetic cooling power of each material. Such linearity was not observed for other screening metrics such as *RCP(T).* The sensitivity of $Ex_q$ to the operating temperature indicate that for FOM cases, a 2 degree deviation from the design cold side or hot side temperatures can result in a drop of performance up to 70%. However, for SOM cases, performance is not very sensitive to the cold side temperature. Nevertheless, SOM cases

also show a moderate sensitivity (up to 20% drop) to the design hot side temperature. These findings were reported in *Journal of Applied Physics* [37].

### 9.3 Performance Stability and Points of Equilibrium

The performance of model FOM ($MnFeP_{1-x}Si_x$ material) in an AMR is investigated. A detailed numerical analysis with fine resolution is utilized to further study the behavior of cooling power curves. Heating and cooling curves of temperature span are simulated to compare with available experimental measurements for FOM material with thermal hysteresis. It is numerically observed that for FOM cases studied, for certain operating conditions, multiple points of equilibrium can be identified. As a result, two or more temperature spans can be obtained for the same hot side temperature which is consistent with our experimental findings. Among these points of equilibrium (PEs) some are stable points and some are unstable depending on the sign of the slope of the cooling power curve in the vicinity of the PE. A larger temperature span corresponds to the case where AMR is being heated and a smaller temperature span corresponds to the case where the AMR is being cooled down. It is also observed that with applying external load and for systems with larger configuration losses, MPEs approach each other and finally overlap. Again, similar behavior has been observed experimentally when FOM material with thermal hysteresis are used in an AMR. [89]. It is concluded that two phenomena are contributing to the shift in performance: thermal hysteresis and multiple points of equilibrium.

## 9.4 Recommendations and Future Works

The current research raised some new aspects to be studied in future research:

- Include magnetic hysteresis in the developed model and investigate the impacts of hysteresis on the performance of FOM in an AMR numerically. This can be done through equilibrium or non-equilibrium thermodynamic analysis. It is recommended that samples of FOM material with low and high hysteresis effects to be identified and experimentally analyzed. The numerical model should be modified to include the entropy generation due to hysteresis. The numerical model needs to be calibrated and validated with several test measurements
- Investigate the efficacy of different material screening techniques for multilayered regenerator. In the current study, a material screening technique was proposed which correlates linearly with optimum performance of one material in an AMR. This screening technique is based on integrating the adiabatic entropy change in the entire range where material exhibits measureable entropy change. It is interesting to further investigate this screening technique in order to understand how entropy curves of multilayered regenerators correlate with the optimum performance of the regenerator.
- In the current study, multiple points of equilibrium were identified for FOM material with sharp change in the magnetic properties as a function of temperature. Further investigation should be performed on the correlation between the slope of magnetic properties and the existence of MPEs. It is rather interesting to look for a

dimensionless parameter that can be used to screen material and identify samples that are prone to having multiple points of equilibrium.

- MPEs need to be investigated through specifically designed experimental measurements in order to analyze the stability of MPEs experimentally. It is also important to investigate experimental methods that can be pursued to avoid the unfavorable points of equilibrium.
- The obtained insight into material screening techniques and multiple points of equilibrium should be used in order to design effective multilayered AMR systems.

# References

[1] N.N. Abu Bakar, M.Y. Hassan, H. Abdullah, H.A. Rahman, M.P. Abdullah, F. Hussin, et al., Energy efficiency index as an indicator for measuring building energy performance: A review, Renew. Sustain. Energy Rev. 44 (2015) 1–11. doi:10.1016/j.rser.2014.12.018.

[2] A.M. Tishin, Y.I. Spichkin, The Magnetocaloric Effect and its Applications, IOP Publishing Ltd 2003, Bristol and Philadelphia, 2003. doi:10.1017/CBO9781107415324.004.

[3] K.A. Gschneidner, V.K. Pecharsky, Rare earths and magnetic refrigeration, J. Rare Earths. 24 (2006) 641–647. doi:10.1016/S1002-0721(07)60001-5.

[4] C. Zimm, A. Jastrab, A. Sternberg, V.K. Pecharsky, K.A. Gschneidner Jr, M. Osborne, et al., Description and performance of a near-room temperature magnetic refrigerator, Adv. Cryog. Eng. 43 (1998) 1759–1766. doi:10.1007/978-1-4757-9047-4_222.

[5] K.A. Gschneidner, V.K. Pecharsky, Magnetic refrigeration materials (invited), J. Appl. Phys. 85 (1999) 5365. doi:10.1063/1.369979.

[6] B. Yu, M. Liu, P.W. Egolf, A. Kitanovski, A review of magnetic refrigerator and heat pump prototypes built before the year 2010, Int. J. Refrig. 33 (2010) 1029–1060. doi:10.1016/j.ijrefrig.2010.04.002.

[7] D.O. Campbell, Investigation of calculated adiabatic temperature change of MnFeP1-xAsx alloys, University of Victoria, 2015.

[8] A. Rowe, A. Tura, Experimental investigation of a three-material layered active magnetic regenerator, Int. J. Refrig. 29 (2006) 1286–1293.

doi:10.1016/j.ijrefrig.2006.07.012.

[9] Y. You, S. Yu, Y. Tian, X. Luo, S. Huang, A numerical study on the unsteady heat transfer in active regenerator with multi-layer refrigerants of rotary magnetic refrigerator near room temperature, Int. J. Refrig. 65 (2016) 238–249. doi:10.1016/j.ijrefrig.2016.02.002.

[10] C. Aprea, A. Greco, A. Maiorino, A numerical analysis of an active magnetic regenerative refrigerant system with a multi-layer regenerator, Energy Convers. Manag. 52 (2011) 97–107. doi:10.1016/j.enconman.2010.06.048.

[11] J. Tušek, A. Kitanovski, U. Tomc, C. Favero, A. Poredoš, Experimental comparison of multi-layered La–Fe–Co–Si and single-layered Gd active magnetic regenerators for use in a room-temperature magnetic refrigerator, Int. J. Refrig. 37 (2013) 1–10. doi:10.1016/j.ijrefrig.2013.09.003.

[12] O. Campbell, A. Rowe, P. Govindappa, Experimental studies of layered AMRs using MnFeP(1-X) As (X), in: IIF-IIR Int. Conf. Magn. Refrig. Victoria, BC, 7-10 Sept. 2014, 2014: pp. 6–7.

[13] B. Monfared, B. Palm, Optimization of layered regenerator of a magnetic refrigeration device, Int. J. Refrig. 57 (2015) 103–111. doi:10.1016/j.ijrefrig.2015.04.019.

[14] K. Skokov, V. V. Khovaylo, K.H. Muller, J.D. Moore, J. Liu, O. Gutfleisch, Magnetocaloric materials with first-order phase transition: thermal and magnetic hysteresis in LaFe11.8Si1.2 and Ni2.21Mn0.77Ga1.02, J. Appl. Phys. 111 (2012) 2012.

[15] V. Basso, C.P. Sasso, G. Bertotti, M. LoBue, Effect of material hysteresis in magnetic refrigeration cycles, Int. J. Refrig. 29 (2006) 1358–1365. doi:10.1016/j.ijrefrig.2006.08.001.

[16] A. Smith, C. Bahl, R. Bjork, K. Engelbrecht, K.K. Nielsen, N. Pryds, Material challenges for high performance magnetocaloric refrigeration devices, Adv. Energy Mater. 2 (2012) 1288–1318.

[17] S.C. Collins, F.J.. Zimmerman, Cyclic Adiabatic Demagnetization, Phys. Rev. 90 (1953) 991–992.

[18] G. V. Brown, Magnetic heat pumping near room temperature, J. Appl. Phys. 47 (1976) 3673–3680. doi:10.1063/1.323176.

[19] V.K. Pecharsky, K.A. Gschneidner Jr, Magnetocaloric effect and magnetic refrigeration, J. Magn. Magn. Mater. 200 (1999) 44–56.

[20] K.K. Nielsen, J. Tusek, K. Engelbrecht, S. Schopfer, a. Kitanovski, C.R.H. Bahl, et al., Review on numerical modeling of active magnetic regenerators for room temperature applications, Int. J. Refrig. 34 (2011) 603–616. doi:10.1016/j.ijrefrig.2010.12.026.

[21] B.M. Siddikov, B.A. Wade, D.H. Schultz, Numerical simulation of the active magnetic regenerator, Comput. Math. with Appl. 49 (2005) 1525–1538. doi:10.1016/j.camwa.2004.07.026.

[22] J. Roudaut, A. Kedous-Lebouc, J.-P. Yonnet, C. Muller, Numerical analysis of an active magnetic regenerator, Int. J. Refrig. 34 (2011) 1797–1804. doi:10.1016/j.ijrefrig.2011.07.012.

[23] T. Lei, K. Engelbrecht, K.K. Nielsen, C.T. Veje, Study of geometries of active magnetic regenerators for room temperature magnetocaloric refrigeration, Appl. Therm. Eng. (2015). doi:10.1016/j.applthermaleng.2015.11.113.

[24] C. Aprea, G. Cardillo, A. Greco, A. Maiorino, C. Masselli, A comparison between experimental and 2D numerical results of a packed-bed active magnetic regenerator, Appl. Therm. Eng. 90 (2015) 376–383. doi:10.1016/j.applthermaleng.2015.07.020.

[25] T.F. Petersen, N. Pryds, A. Smith, J. Hattel, H. Schmidt, H.-J. Høgaard Knudsen, Two-dimensional mathematical model of a reciprocating room-temperature Active Magnetic Regenerator, Int. J. Refrig. 31 (2008) 432–443. doi:10.1016/j.ijrefrig.2007.07.009.

[26] S. Lionte, C. Vasile, M. Siroux, Numerical analysis of a reciprocating active magnetic regenerator, Appl. Therm. Eng. 75 (2015) 871–879. doi:10.1016/j.applthermaleng.2014.10.076.

[27] A. Rowe, Thermodynamics of active magnetic regenerators: Part I, Cryogenics. 52 (2012) 111–118. doi:10.1016/j.cryogenics.2011.09.005.

[28] T. Burdyny, D.S. Arnold, A. Rowe, AMR thermodynamics: Semi-analytic modeling, Cryogenics. 62 (2014) 177–184. doi:10.1016/j.cryogenics.2014.03.013.

[29] T. Burdyny, A. Ruebsaat-Trott, A. Rowe, Performance modeling of AMR refrigerators, Int. J. Refrig. 37 (2014) 51–62. doi:10.1016/j.ijrefrig.2013.08.007.

[30] K. Engelbrecht, C.R.H. Bahl, K.K. Nielsen, Experimental results for a magnetic refrigerator using three different types of magnetocaloric material regenerators, Int. J. Refrig. 34 (2011) 1132–1140. doi:10.1016/j.ijrefrig.2010.11.014.

[31] A. Tura, A. Rowe, Permanent magnet magnetic refrigerator design and experimental characterization, Int. J. Refrig. 34 (2011) 628–639. doi:10.1016/j.ijrefrig.2010.12.009.

[32] I. Niknia, O. Campbell, T. V. Christianse, P. Govindappa, R. Teyber, P.V. V. Trevizoli, et al., Impacts of configuration losses on active magnetic regenerator device performance., Appl. Therm. Eng. 106 (2016) 601–612. doi:10.1016/j.applthermaleng.2016.06.039.

[33] A. Rowe, Configuration and performance analysis of magnetic refrigerators, Int. J. Refrig. 34 (2011) 168–177. doi:10.1016/j.ijrefrig.2010.08.014.

[34] V. Pecharsky, K. Gschneidner, A. Pecharsky, A. Tishin, Thermodynamics of the magnetocaloric effect, Phys. Rev. B. 64 (2001) 144406. doi:10.1103/PhysRevB.64.144406.

[35] V.K. Pecharsky, K.A. Gschneidner, Some common misconceptions concerning magnetic refrigerant materials, J. Appl. Phys. 90 (2001) 4614–4622. doi:10.1063/1.1405836.

[36] T. Burdyny, Simplified Modeling of Active Magnetic Regenerators by Simplified Modeling of Active Magnetic Regenerators, University of Victoria, 2012.

[37] I. Niknia, P. V Trevizoli, T. V Christiaanse, P. Govindappa, R. Teyber, A. Rowe, Material screening metrics and optimal performance of an active magnetic regenerator, J. Appl. Phys. in proofs (2017). doi:10.1063/1.4975833.

[38] K.A. Gschneidner, V.K. Pecharsky, Magnetocaloric materials, Annu. Rev. Mater. Sci. 30 (2000) 387–429.

[39] A. Kitanovski, J. Tušek, U. Tomc, U. Plaznik, M. Ožbolt, A. Poredoš, Magnetocaloric Energy Conversion, Springer International Publishing, Switzerland, 2015. doi:10.1007/978-3-319-08741-2.

[40] A. Rowe, Active magnetic regenerators : Performance in the vicinity of ..., University of Victoria, 2002.

[41] P. Lloveras, E. Stern-Taulats, M. Barrio, J.L. Tamarit, S. Crossley, W. Li, et al., Giant barocaloric effect at low pressure in ferrielectric ammonium sulphate, Nat Commun. 6 (2015) 1–20. doi:10.1038/ncomms9801.

[42] B.F. Yu, Q. Gao, B. Zhang, X.Z. Meng, Z. Chen, Review on research of room temperature magnetic refrigeration, Int. J. Refrig. 26 (2003) 622–636. doi:10.1016/S0140-7007(03)00048-3.

[43] M.H. Phan, S.C. Yu, Review of the magnetocaloric effect in manganite materials, J. Magn. Magn. Mater. 308 (2007) 325–340. doi:10.1016/j.jmmm.2006.07.025.

[44] V. Franco, J.S. Blázquez, B. Ingale, A. Conde, The Magnetocaloric Effect and Magnetic Refrigeration Near Room Temperature: Materials and Models, Annu. Rev. Mater. Res. 42 (2012) 305–342. doi:10.1146/annurev-matsci-062910-100356.

[45] A.M. Tishin, K.A. Gschneidner Jr., V.K. Pecharsky, Magnetocaloric effect and heat capacity in the phase-transition region, Phys. Rev. B. 59 (1999) 503–511. http://www.scopus.com/inward/record.url?eid=2-s2.0-4243570041&partnerID=40.

[46] S. Dan'kov, A.M. Tishin, V.K. Pecharsky, K.A. Gschneidner, Magnetic phase transitions and the magnetothermal properties of gadolinium, Phys. Rev. B. 57 (1998) 3478–3490. doi:10.1103/PhysRevB.57.3478.

[47] V.K. Pecharsky, K.A. Gschneidner, D. Fort, Zero-field and magnetic-field low-temperature heat capacity of solid-state electrotransport-purified erbium, Phys. Rev. B. 47 (1993) 5063–5071. doi:10.1103/PhysRevB.47.5063.

[48] W. Dai, B.G. Shen, D.X. Li, Z.X. Gao, New magnetic refrigeration materials for temperature range from 165 K to 235 K, J. Alloys Compd. 311 (2000) 22–25. doi:10.1016/S0925-8388(00)00852-5.

[49] O. Tegus, E. Brück, K.H.J. Buschow, F.R. de Boer, Transition-metal-based magnetic refrigerants for room-temperature applications., Nature. 415 (2002) 150–152. doi:10.1038/415150a.

[50] I.F. Gribanov, A. V. Golovchan, D. V. Varyukhin, V.I. Val'Kov, V.I. Kamenev, A.P. Sivachenko, et al., Magnetic and magnetocaloric properties of the alloys Mn(2-x)Fe(x)P0.5As0.5, Low Temp. Phys. 35 (2009) 786–791. doi:10.1063/1.3253401.

[51] D.T. Cam Thanh, E. Brück, O. Tegus, J.C.P. Klaasse, T.J. Gortenmulder, K.H.J. Buschow, Magnetocaloric effect in MnFe(P,Si,Ge) compounds, J. Appl. Phys. 99

(2006). doi:10.1063/1.2170589.

[52] D.T. Cam Thanh, E. Brück, N.T. Trung, J.C.P. Klaasse, K.H.J. Buschow, Z.Q. Ou, et al., Structure, magnetism, and magnetocaloric properties of MnFeP[1−x]Si[x] compounds, J. Appl. Phys. 103 (2008) 07B318. doi:10.1063/1.2836958.

[53] N.H. DŨNG, Moment formation and giant magnetocaloric effects in hexagonal Mn-Fe-P-Si compounds, Technical University of Delft, 2012.

[54] E. Brück, O. Tegus, X.W. Li, F.R. de Boer, K.H.J. Buschow, Magnetic refrigeration—towards room-temperature applications, Phys. B Condens. Matter. 327 (2003) 431–437. doi:10.1016/S0921-4526(02)01769-6.

[55] E. Brück, M. Ilyn, A.M. Tishin, O. Tegus, Magnetocaloric effects in MnFeP[1−x]As[x]-based compounds, J. Magn. Magn. Mater. 290–291 (2005) 8–13. doi:10.1016/j.jmmm.2004.11.152.

[56] M.E. Wood, W.H. Potter, General analysis of magnetic refrigeration and its optimization using a new concept: maximization of refrigerant capacity, Cryogenics. 25 (1985) 667–683. doi:10.1016/0011-2275(85)90187-0.

[57] K. Engelbrecht, C.R.H. Bahl, Evaluating the effect of magnetocaloric properties on magnetic refrigeration performance, J. Appl. Phys. 108 (2010) 1–7. doi:10.1063/1.3525647.

[58] C. Aprea, A. Greco, A. Maiorino, C. Masselli, A comparison between rare earth and transition metals working as magnetic materials in an AMR refrigerator in the room temperature range, Appl. Therm. Eng. 91 (2015) 767–777. doi:10.1016/j.applthermaleng.2015.08.083.

[59] K.G. Sandeman, Magnetocaloric materials: The search for new systems, Scr. Mater. 67 (2012) 566–571. doi:10.1016/j.scriptamat.2012.02.045.

[60] K.A. GschneidnerJr, V.K. Pecharsky, A.O. Tsokol, Recent developments in magnetocaloric materials, Reports Prog. Phys. 68 (2005) 1479–1539. doi:10.1088/0034-4885/68/6/R04.

[61] F. Guillou, H. Yibole, G. Porcari, L. Zhang, N.H. Van Dijk, E. Br??ck, et al., Magnetocaloric effect, cyclability and coefficient of refrigerant performance in the MnFe(P, Si, B) system, J. Appl. Phys. 116 (2014) 63903. doi:10.1063/1.4892406.

[62] M.F. Ashby, Materials Selection in Mechanical Design, Third, Butterworth-Heinemann, 2005. doi:10.1016/B978-1-85617-663-7.00011-4.

[63] X. Moya, S. Kar-Narayan, N.D. Mathur, Caloric materials near ferroic phase transitions., Nat. Mater. 13 (2014) 439–50. doi:10.1038/nmat3951.

[64] P.V. Trevizoli, Development of thermal regenerators for magnetic cooling applications, PhD Thesis, Federal University of Santa Catarina, 2015. http://www.polo.ufsc.br/portal/en/publicacoes.

[65] D.S. Arnold, A. Tura, A. Rowe, Experimental analysis of a two-material active magnetic regenerator, Int. J. Refrig. 34 (2011) 178–191. doi:10.1016/j.ijrefrig.2010.08.015.

[66] D. Arnold, Design Principles and Performance Metrics for Magnetic Refrigerators Operating Near Room Temperature by, University of Victoria, 2014.

[67] D.S. Arnold, A. Tura, A. Ruebsaat-Trott, A. Rowe, Design improvements of a permanent magnet active magnetic refrigerator, Int. J. Refrig. 37 (2014) 99–105. doi:10.1016/j.ijrefrig.2013.09.024.

[68] Y. You, Y. Guo, S. Xiao, S. Yu, H. Ji, X. Luo, Numerical simulation and performance improvement of a multi-polar concentric Halbach cylindrical magnet for magnetic refrigeration, J. Magn. Magn. Mater. 405 (2016) 231–237. doi:10.1016/j.jmmm.2015.12.077.

[69] A. Tura, Design and Analysis of a Nested Halbach Permanent Magnet Magnetic Refrigerator by, (2013) 122.

[70] K. Engelbrecht, A Numerical Model of an Active Magnetic Regenerator Refrigerator with Experimental Validation by, University of Wisconsin-Madison, 2008.

[71] J. Dikeos, Development and Validation of an Active Magnetic Regenerator Refrigeration Cycle Simulation by Development and Validation of an Active Magnetic Regenerator Refrigeration Cycle Simulation, University of Victoria, 2006.

[72] J. Dikeos, A. Rowe, Validation of an active magnetic regenerator test apparatus model, Int. J. Refrig. 36 (2013) 99–105. doi:10.1016/j.ijrefrig.2012.12.003.

[73] M. Kaviany, Principles of Heat Transfer in Porous Media, New York, NY, 1995. doi:10.1017/CBO9781107415324.004.

[74] K.L. Engelbrecht, G.F. Nellis, S.A. Klein, A.M. Boeder, Modeling active magnetic regenerative refrigeration systems, in: 1st Int. Conf. Magn. Refrig. Room Temp., 2006: pp. 265–274.

[75] N. Wakao, S. Kaguei, Heat and Mass Transfer in Packed Beds., Gordon and Breach Science Publishers, New York, NY, 1982.

[76] K.L. Engelbrecht, G.F. Nellis, S. a. Klein, The Effect of Internal Temperature Gradients on Regenerator Matrix Performance, J. Heat Transfer. 128 (2006) 1060–1069. doi:10.1115/1.2345428.

[77] I. Macdonald, Flow through porous media-The Ergun equation revisited, Ind. Eng. Chem. Fundam. 18 (1979) 199–208.

[78] P. Li, M. Gong, G. Yao, J. Wu, A practical model for analysis of active magnetic regenerative refrigerators for room temperature applications, Int. J. Refrig. 29

(2006) 1259–1266. doi:10.1016/j.ijrefrig.2006.07.021.

[79] C. Kittel, Introduction to Solid State Physics, John Wiley & Sons Inc., New York, 1953.

[80] L. Rosario, M.M. Rahman, Analysis of a magnetic refrigerator, Appl. Therm. Eng. 31 (2011) 1082–1090. doi:10.1016/j.applthermaleng.2010.12.002.

[81] P. V Trevizoli, J.R.B. Jr, A. Tura, D. Arnold, A. Rowe, Modeling of Thermo-magnetic Phenomena in Active Magnetocaloric Regenerators, J. Therm. Sci. Eng. Appl. 6 (2014).

[82] D. Jiles, Introduction to magnetism and magnetic materials, Chapman and Hall, London, 1991. doi:10.1017/CBO9781107415324.004.

[83] R.D. Skeel, M. Berzins, A Method for the Spatial Discretization of Parabolic Equations in One Space Variable, SIAM J. Sci. Stat. Comput. 11 (1990) 1–32. doi:10.1137/0911001.

[84] H.S. Atamturktur, B. Moaveni, C. Papadimitriou, T. Schoenherr, eds., Model Validation and Uncertainty Quantification,Vol3, in: Proc. 32nd IMAC, A Conf. Expo. Struct. Dyn. 2014, Springer, 2014: p. 419. doi:10.1007/978-3-319-04552-8.

[85] D.J. Silva, B.D. Bordalo, J. Puga, A.M. Pereira, J. Ventura, J.C.R.E. Oliveira, et al., Optimization of the physical properties of magnetocaloric materials for solid state magnetic refrigeration, Appl. Therm. Eng. 99 (2016) 514–517. doi:10.1016/j.applthermaleng.2016.01.026.

[86] T. Lei, K.K. Nielsen, K. Engelbrecht, C.R.H. Bahl, H. Neves Bez, C.T. Veje, et al., Sensitivity study of multi-layer active magnetic regenerators using first order magnetocaloric material La(Fe,Mn,Si)13Hy, J. Appl. Phys. 118 (2015) 14903. doi:10.1063/1.4923356.

[87] W. Brey, G. Nellis, S. Klein, Thermodynamic modeling of magnetic hysteresis in AMRR cycles, Int. J. Refrig. 47 (2014) 85–97. doi:10.1016/j.ijrefrig.2014.07.013.

[88] T.D. Brown, I. Karaman, P.J. Shamberger, Impact of cycle-hysteresis interactions on the performance of giant magnetocaloric effect refrigerants, Mater. Res. Express. 3 (2016) 74001. doi:10.1088/2053-1591/3/7/074001.

[89] L. Von Moos, K.K. Nielsen, K. Engelbrecht, C.R.H. Bahl, Experimental investigation of the effect of thermal hysteresis in first order material MnFe(P,As) applied in an AMR device, Int. J. Refrig. 37 (2014) 303–306. doi:10.1016/j.ijrefrig.2013.05.005.